

# REON

## SACRAMENTO PLANT



REPORT NO. RN-S-0243  
TO  
AEC-NASA SPACE NUCLEAR PROPULSION OFFICE  
  
CENTERBODY DIFFUSER STUDY

NERVA PROGRAM

CONTRACT SNP-1

OCTOBER 1965

FACILITY FORM 602

**N66 26757**  
ACCESSION NUMBER

124  
(PAGES)

CR 75-521  
(NASA CR OR TMX OR AD NUMBER)

\_\_\_\_\_  
(THRU)

52  
(CODE)

\_\_\_\_\_  
(CATEGORY)

GPO PRICE \$ \_\_\_\_\_

CFSTI PRICE(S) \$ \_\_\_\_\_

Hard copy (HC) 4.00

Microfiche (MF) 1.00

ff 653 July 65



AEROJET GENERAL CORPORATION



---

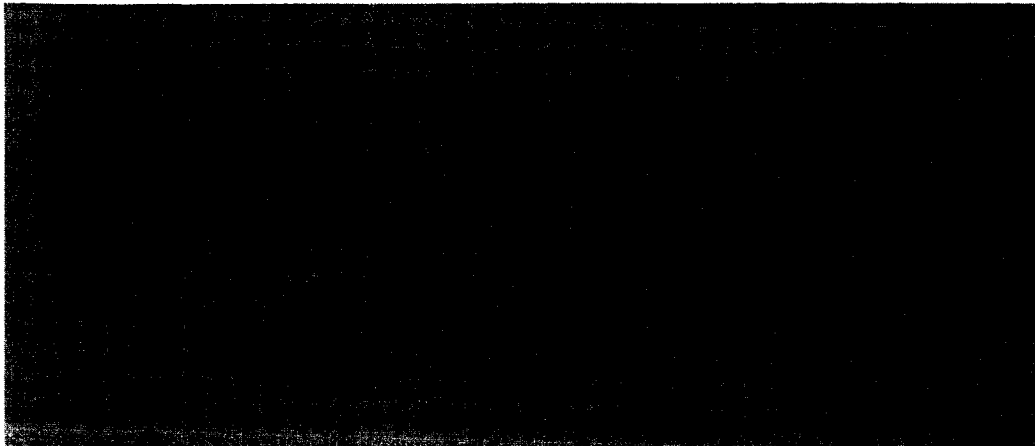
REPORT NO. RN-S-0243

CENTERBODY DIFFUSER STUDY

NERVA PROGRAM

OCTOBER 1965

CONTRACT SNP-1



**AEROJET-GENERAL CORPORATION**  
A SUBSIDIARY OF THE GENERAL TIRE & RUBBER COMPANY

# ABSTRACT

This report presents the analytical and experimental evaluation of the scale model centerbody diffuser test program of Contract Year 1965. Nine centerbody diffusers were tested and evaluated to determine the feasibility of cooling centerbody diffusers for nuclear rocket application in Engine/Stage Test Stand 2 and 3. As a result of the data obtained through this analytical and experimental evaluation, the design implications for a centerbody diffuser for testing NERVA II in E/STS-2/3 have been drawn.


*for*   
W. D. Stinnett  
Program Manager  
REON

TABLE OF CONTENTS

	<u>Page</u>
I. SUMMARY	I-1
II. CONCLUSIONS AND RECOMMENDATIONS	II-1
III. INTRODUCTION	III-1
IV. TEST FACILITY AND GENERAL APPARATUS	IV-1
V. RESULTS AND DISCUSSION	V-1
REFERENCES	V-49
APPENDIX A	
Method for Correcting Indicated Heat Transfer Convection Coefficients for Longitudinal Conduction Effects in Thin-Walled Sections	A-1
Nomenclature	A-9
APPENDIX B	
Stagnation Point Heat Transfer for a Spherical Body	B-1
APPENDIX C	
Laminar Heat Transfer Rates to Centerbody Nose as a function of Distribution Angle $\theta$	C-1
APPENDIX D	
Turbulent Heat Transfer Rates to Centerbody Nose as a function of Distribution Angle $\theta$	D-1
APPENDIX E	
Laminar Heat Transfer Rates to Cone Frustum	E-1
APPENDIX F	
Heat Transfer to the Struts	F-1

## CENTERBODY DIFFUSER

LIST OF ILLUSTRATIONS

<u>Figure</u>		<u>Page</u>
IV-1	Centerbody Diffuser Layout 1/15 Scale Model	IV-2
IV-1a	Comparison of a Centerbody Diffuser to an Equivalent Second-Throat Diffuser	IV-3
IV-1b	Centerbody Diffuser Parameters	IV-4
IV-2	NERVA II Centerbody Diffuser 1/15 Scale Model	IV-5
IV-3	Stored Energy Heater, Azusa Proving Grounds	IV-6
IV-4	Centerbody Weldment, Downstream View	IV-8
IV-5	Small Radius Nosecones with Specifications	IV-9
IV-6	Small Radius Nosecones, a closeup photograph	IV-10
IV-7	Intermediate Radius Nosecones with Specifications	IV-11
IV-8	Intermediate Radius Nosecones, a closeup photograph	IV-12
IV-9	Large Radius Nosecones with Specifications	IV-13
IV-10	Large Radius Nosecones, a closeup Photograph	IV-14
IV-11	Thermocouples attached to Nose and Cone prior to Final Weld	IV-16
IV-12	Special Welding Fixture for Nose to Cone Weld Joint	IV-17
IV-13	Thermocouple Wires on the Interior of Nosecone	IV-18
IV-14	Centerbody Weldment - Side View	IV-19
IV-15	Centerbody Weldment - Upstream View	IV-20
IV-16	NERVA II Centerbody Diffuser Note Thermocouple Wires in Vane	IV-21
IV-17	NERVA II Centerbody Diffuser, Upstream View	IV-22
IV-18	Instrumentation Locations 1/15 Scale-Model Centerbody Diffuser	IV-25
IV-19	Thermocouple Locations Small Radius Nosepieces	IV-26
IV-20	Thermocouple Locations Intermediate Radius Nosepieces	IV-27
IV-21	Thermocouple Locations Large Radius Nosepieces	IV-28

LIST OF ILLUSTRATIONS, CONTINUED

<u>Figure</u>		<u>Page</u>
V-1	Experimental Heat Transfer Coefficient (h) as a function of Developed Contour Length (s), Run No. 13	V-5
V-2	Experimental Heat Transfer Coefficient (h) as a function of Developed Contour Length (s), Run No. 15	V-6
V-3	Experimental Heat Transfer Coefficient (h) as a function of Developed Contour Length (s), Run No. 17	V-7
V-4	Experimental Heat Transfer Coefficient (h) as a function of Developed Contour Length (s), Run No. 23	V-8
V-5	Experimental Heat Transfer Coefficient (h) as a function of Developed Contour Length (s), Run No. 24	V-9
V-6	Experimental Heat Transfer Coefficient (h) as a function of Developed Contour Length (s), Run No. 22	V-10
V-7	Experimental Heat Transfer Coefficient (h) as a function of Developed Contour Length (s), Run No. 21	V-11
V-8	Experimental Heat Transfer Coefficient (h) as a function of Developed Contour Length (s), Run No. 20	V-12
V-9	Experimental Heat Transfer Coefficient (h) as a function of Developed Contour Length (s), Run No. 19	V-13
V-10	Experimental Centerbody Stagnation Point Heat Transfer Coefficients as a function of Nosecone Radius	V-14
V-11	Laminar Heat Transfer Coefficient (h) as a Spherical Centerbody Versus Nose Radius and Location	V-24
V-12	Laminar Heating Rates ( $q_1$ ) on a Spherical Centerbody versus Nose Radius and Locations	V-25
V-13	Turbulent Heating Rates ( $q_t$ ) on a Spherical Centerbody versus Nose Radius and Location	V-28
V-14	Turbulent Heat Transfer Coefficient (h) on Spherical Centerbody, versus Nose Radius and Location	V-29
V-15	Composite Heat Transfer Coefficients versus Contour Distance from Stagnation Point (Nose Radius R = 1.58")	V-31
V-16	Composite Heat Transfer Coefficients versus Contour Distance from Stagnation Point (nose Radius R = 0.87")	V-32

LIST OF ILLUSTRATIONS, CONTINUED

<u>Figure</u>		<u>Page</u>
V-17	Composite Heat Transfer Coefficients versus Contour Distance From Stagnation Point (Nose Radius $R = 0.395''$ )	V-33
V-18	Dynamic Viscosity $\mu$ of $N_2$ as a Function of Absolute Temperature	V-38
V-19	Cell and Nozzle Exit Pressures versus Nozzle Chamber Pressure	V-44
V-20	Static Wall Pressures versus Longitudinal Position	V-45
V-21	Static Wall Pressures versus Nozzle Chamber Pressure	V-46
V-22	Stagnation Pressure of Front Strut versus Nozzle Chamber Pressure	V-47
	Appendix A	
A-1	Geometry used for Spherical Nose Segment	A-3
A-2	Geometry used for Conical Section	A-4
A-3	Typical Geometry used in Analysis	A-5
	Appendix C	
C-1	Pressure Distribution over a Spherical Body in a Supersonic Gas Stream	C-3
C-2	Velocities versus Angle $\theta$	C-7

## NOMENCLATURE AND SYMBOLOGY

NES	Nuclear Exhaust System
NERVA	Nuclear Engine for Rocket Vehicle Application
diffuser	device to recover static pressure
ejector	pumping device to decrease the static pressure of a second fluid by increase of its momentum
environmental cell	an airtight enclosure surrounding the NERVA engine. The diffuser attaches to the environmental cell resulting in an airtight assembly except for the exit of the diffuser. Lowered back pressures, $P_v$ (altitude simulation) exist throughout the environmental cell when the primary (NERVA) nozzle is fired into the diffuser.
forward stagnation point	stagnation point coinciding with geometrical summit of centerbody tip.
Newtonian pressure	pressure resulting from Newton's friction law (shearing stress proportional to viscosity and velocity gradient)
mounting strut	connecting member between centerbody and duct
scale-model	equivalent to small scale, or subscale in contrast to full scale.
sonic point	location on centerbody contour, where gas flow becomes supersonic
starting pressure	that chamber pressure at which the nozzle starts to flow full (minimum cell pressure)
tangential velocity	tangential component of velocity vector at the edge of the boundary layer along centerbody contour.

# NOMENCLATURE AND SYMBOLOGY

<u>Upper Case</u>	<u>Description</u>
A	area
$A_{gn}$	area of the increment $\Delta x_n$ subject to convective heat flux
A,B,D	parameters in heat flux equation (Lester Lees' relation for points along conical surface)
C	dimensionless constant (for heat transfer parameter f)
D	diameter
F	thermal radiation view factor
$GN_2$	gaseous nitrogen
H	enthalpy
$\Delta H$	enthalpy difference
J	heat conversion factor
K	geometry constant
L	length, (along centerline for duct)
M	Mach Number
$M_n$	mass of increment $\Delta X_n$
$N_u$	Nusselt Number
P	pressure, or total pressure
$P_r$	Prandtl Number
Q	heat quantity
R	gas constant
R	radius (in general)
$R_o$ } $R_b$ }	radius of spherical nose
$R_M$	mean radius of spherical nose segment equal to $(R - b/2)$

<u>Upper Case</u>	<u>Description</u>
$R_e$	Reynolds Number
$\Delta S$	stand-off distance of shock wave from body
$St$	Stanton Number
$T$	temperature or total temperature
$T_n$	temperature of increment n with length $\Delta x_n$
$\Delta T$	temperature difference
$\Delta T_n$	temperature rise of an increment at end of time interval $\Delta \beta$
$\bar{T}_n$	average temperature of an increment at beginning of time interval $\Delta \beta$

#### Lower Case

$b$	wall thickness
$c_p$	specific heat
$f$	dimensionless heat parameter
$g$	gravitational constant
$h$	convective heat transfer coefficient
$h_n$	local convection heat transfer coefficient for an increment
$h'_n$	local indicated convection heat transfer coefficient (uncorrected for longitudinal conduction and curvature characteristics of thin wall)

$$h'_n = \frac{\rho c b}{(T_R - T_n)} \frac{dT_n}{d\beta}$$

$k$	thermal conductivity
$n$	number of points along shock wave
$p$	pressure, or static pressure
$q$	heat flow rates per unit area
$r_{M_n}$	radial distance from axis to the center of an increment n

<u>Lower Case</u>	<u>Description</u>
$r_n$	radial distance equal to $r_{M_n} + \frac{1}{2} b \cos \alpha$
$s$	distance from forward stagnation point to a point on conical surface
$s'$	distance from virtual cone tip to a point on conical surface
$t$	temperature, or static temperature
$u$	velocity
$\frac{\partial u}{\partial x}$	velocity gradient along centerbody surface (see also $\beta$ )
$x$	arc length along spherical part of center body surface from forward stagnation point
$\Delta x_n$	length of an increment $n$ with an average temperature equal to $T_n$
(1)	indicates region 1 (ahead of bow shock)
(2)	indicates region 2 (behind bow shock)

#### Greek

$\alpha$	cone half - angle (front-end of centerbody)
$\beta$	cone half - angle (tail-end of centerbody)
$\beta$	time
$\beta$	velocity gradient along centerbody surface
$\gamma$	specific heat ratio
$\epsilon$	area ratio exit to throat
$\rho$	density
$\mu$	viscosity
$X_1$	abscissa (computation of pressure distribution)
$\theta$	angle corresponding to contour distance $X$ from forward stagnation point

<u>Subscripts</u>	<u>Description</u>
1,2,3,4,...	station locations
1	region ahead of bow shock
2	region behind bow shock
a	ambient, or atmospheric
c	chamber conditions
c	conduction
c	centerbody
d	duct
e	edge of boundary layer
e	nozzle exit plan
e or se	outside the boundary layer (edge of boundary layer) and stagnation conditions
i	initial
max	maximum
n	denotes any increment n where n is an integer, i.e., n = 1, 2, 3, 4, --
o	forward stagnation point
pr	denotes practical results, or experimental results
st or s	stagnation conditions
str	strut
v	environmental cell
th	theoretical, or throat
x	variation with arc length X along contour of CB
AN	annular cross-section, or flow area
CB	center body
D	duct
L	laminar flow conditions
R	thermal radiation contribution

<u>Subscripts</u>	<u>Description</u>
R	recovery conditions
S	shock wave
T	turbulent flow conditions
W	centerbody wall conditions, or wall surface
$\infty$	free stream conditions

#### Superscripts

*	critical conditions (points where local speed equals speed of sound)
-	average value

## I. SUMMARY

This report presents the analytical and experimental evaluation of the scale-model centerbody diffuser test program of Contract Year 1965. To determine the feasibility of water-cooled centerbody diffusers for nuclear rocket application in Engine/Stage Test Stand No. 2 and 3, nine different centerbody configurations were fabricated. The subscale models included three nose cone sizes, and for each nose cone size three different cone frustrums were designed. The cones varied by the magnitude of their half-angle.

Testing was conducted at the Aerojet-General Corporation, Azusa, Proving Grounds utilizing the pressure blow-down system in series with a large, stored-energy heater to supply the gaseous nitrogen to the 1/15 size NERVA II nozzle.

Temperature measurements were taken on the various nose cones using chromel-alumel thermocouples. The Aerojet Digital Data Acquisition System (ADDAS) was used in conjunction with a high-speed electronic sampling switch. The ADDAS converts sampled test readings onto magnetic tape in digital form, which is then processed through an IBM 7094 computer. Raw and processed data were printed out one to two hours after completion of a particular test by the computer.

The test procedure yielded experimental heat transfer coefficients which are shown on Figures V-1 through V-9. Each Figure gives the convective heat transfer coefficient "h" versus the developed distance "s" along the centerbody contour, and the range of chamber pressure and temperature variation for the run represented by the graph.

The analytical work comprised detailed computations of expected heating rates of the forward stagnation point, the spherical segment for laminar and turbulent flow, the transition point sphere-to-cone and the conical segment for laminar conditions only. Heating rates at the mounting struts were computed for laminar flow with the assumption of a maximum Mach number of 2. Figures V-10 through V-18 illustrate the results of the computations in graphical form, the last three giving composite heating rates. Additional sections deal with adjustments and conversion formulas to bring the predictions in line the actual test conditions.

Scale-up procedures to full size NERVA II diffuser are explained and discussed. Some reservations are made as to their applicability. One of the reservations deals with the problem of gas dissociation at high temperatures to be encountered during full scale operation.

The aerodynamic performance is discussed by comparing starting pressure behavior in connection with normal shock theory.

Conclusions and recommendations are discussed in detail. They comprise the aerodynamic the thermodynamic phases of the program and include all important analytical and experimental findings. The major conclusion can be phrased as follows:

As compared to conventional ejector-diffusers, a relatively short diffuser of the centerbody type is workable and can be built in appropriate sizes to ground test large nuclear engines.

## II. CONCLUSIONS AND RECOMMENDATIONS

The conclusions listed below result from the theoretical and experimental studies (both aerodynamic and thermodynamic) regarding the feasibility of a centerbody diffuser.

### 1. Aerodynamics

Test measurements of chamber pressure and temperature, nozzle exit pressure, cell pressure and selected pressures along inside duct wall were taken to evaluate aerodynamic performance of the various subscale models.

- a. For the range tested, nose cone angles and radii seemed to have no noticeable influence on the ejector starting pressure.
- b. With the use of a correlation factor of 1.15, the starting pressure ratio can be predicted by means of the conventional normal shock theory.
- c. Without the attenuating factor of turbine exhaust, pressure instabilities were observed prior to start.

### 2. Thermodynamics and Heat Transfer

a. This study has proven that a full-scale, water-cooled centerbody diffuser can be built and that scale-up procedures present no major problems which cannot be solved.

b. A theoretical investigation of heating rates involving the spherical tip, the cone frustrum, the transition point cone-to-sphere, and the mounting struts of the centerbody for laminar and turbulent flow, revealed that the absolute maximum heating rate is located at the sonic point, i.e., a spot on the spherical segment under turbulent flow conditions about  $41^\circ$  from the forward stagnation point.

c. Except for a short area close to the forward stagnation point, maximum heating rates are those resulting from turbulent flow.

d. For any location, heating rates are inversely proportional to the size of the nose radius.

e. Depending upon nose size, maximum turbulent heating rates are from 20% to 80% higher than the laminar maxima at the forward stagnation point; the smaller the nose, the smaller is this difference.

f. For a Mach number of 2, the laminar heating rates at the stagnation point of the struts are only a fraction of those of the centerbody tip. This fraction is 40% for equal radii and becomes 80% when the strut curvature radius is one quarter that of the centerbody tip radius. For larger Mach numbers, small curvature radii, or turbulent flow, the heating rates at the struts could become larger than the centerbody maxima.

g. The reduced data from the experimental tests indicate heating rates which, on the average, are smaller than those predicted.

h. Heat transfer rates to the duct walls should be analyzed. From hot spots along the duct, the impact of oblique shocks and their reflections could be detected and their influence evaluated.

i. Full-scale model calculations should include such additional heating as may result from gas dissociation at temperature above 3000°R. The additional heat contribution from this source, which for 4000°R hydrogen was estimated to be approximately 10% of all other sources, should be analyzed in greater detail prior to full-scale design.

### III. INTRODUCTION

Captive testing of a nuclear engine or stage is necessarily a much more complex operation than is captive testing of a chemical engine or stage. There are four main reasons for this:

1. Chemical engines can be fired, the diffuser or exhaust deflector repaired and or modified and the engine refired until satisfactory performance is achieved, provided no catastrophic failure occurs. But, once a nuclear engine is brought up to power, its fission products and level of induced radioactivity make subsequent servicing difficult or impractical.
2. Captive testing of nuclear engines involves exhausting downward large quantities of unburned hydrogen gas heated to well above its auto-ignition temperature.
3. Radiation scattered during ground tests by air and test stand materials must be suppressed if overtesting of components sensitive to radiation and overheating engine or stage materials and the propellant is to be avoided.
4. Direct radiation from the nuclear engine while it is operating, and radioactive contamination resulting from the estimated 10% of the fission products formed that diffuse out into the engine exhaust present hazards to personnel.

As engines grow in size, and nozzle area ratios increase, the diameter of the diffuser system must be similarly increased. One governing parameter in diffuser operation is the length-to-diameter ratio. As the diameter is increased, the length must also be increased to maintain a reasonable efficiency. Prohibitive test stand heights are soon required.

One method whereby test stand heights can be maintained at a reasonable value is by the use of a centerbody in the diffuser to accomplish the shocking process in a shorter overall length. This preliminary investigation has generated information as to heat transfer to the centerbody, centerbody geometry, aerodynamic performance and in general has shown the feasibility of using centerbodies in nuclear exhaust systems.

By uprating the NERVA in power level by a factor of 5 and increasing the nozzle area ratio to 40:1, the NES currently planned for ETS-1 will not be satisfactory. This preliminary study has laid the ground work for sizing future test stands, and determining diffuser-ejector configurations required for testing future flight versions of the NERVA engine.

#### IV. TEST FACILITY AND GENERAL APPARATUS

##### A. TEST FACILITY

Scale-model testing (1/15 size) of various centerbody diffusers was conducted to determine the feasibility of a full-scale centerbody diffuser system that could be used to test the NERVA II engine. As shown in Figure IV-1, IV-1a, and IV-1b, a centerbody diffuser is comprised of three major components; the engine compartment (environmental cell), the diffuser duct and the centerbody. A typical scale-model centerbody diffuser ready for testing is shown in Figure IV-2.

The working fluid was fed into the nozzle at controlled pressure and temperature. During the course of a test run, pressures and temperatures throughout the diffuser were recorded on IBM tape. These records were then reduced to obtain pressure and temperature histories of the test run.

The fluid used during this program was nitrogen. The nitrogen was heated to about 1350°R in a stored energy heater (see Figure IV-3). The stored energy heater contains long coils of thick-wall stainless steel tubing, which are heated to about 1800°R by natural gas burners. Prior to a test run, nitrogen was pumped into storage bottles under a pressure of about 2400 psia. When the compressed nitrogen was released, it flowed through the hot tubes of the stored energy heater wherein heat was exchanged to the gas. The hot nitrogen was mixed with unheated nitrogen so that a temperature of about 1350°R was maintained during the run. Prior to a test, some hot gas was used to preheat the feed line and was bled off just upstream of the burst diaphragm. After the feed line was up to temperature, the hot gas bleed valve was closed and the hot nitrogen was brought up to run pressure which burst the aluminum diaphragm.

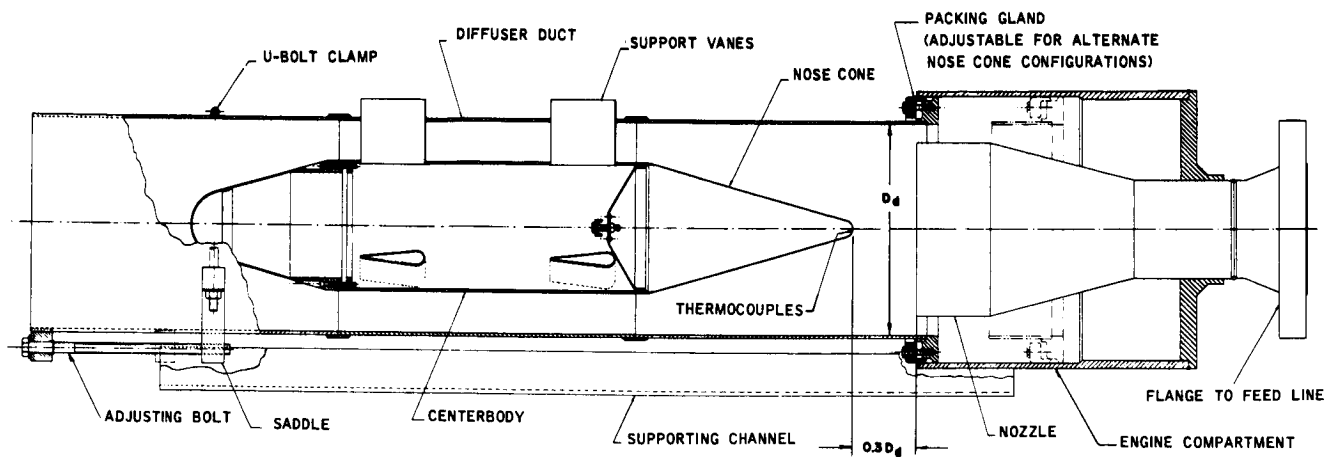
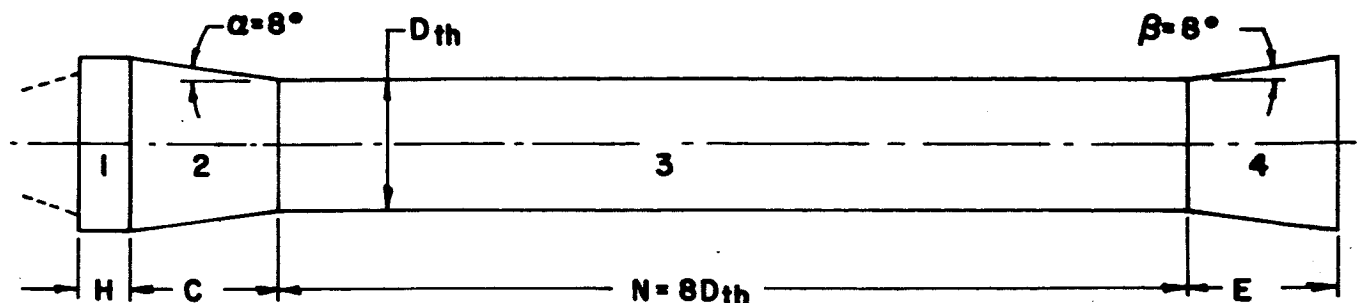
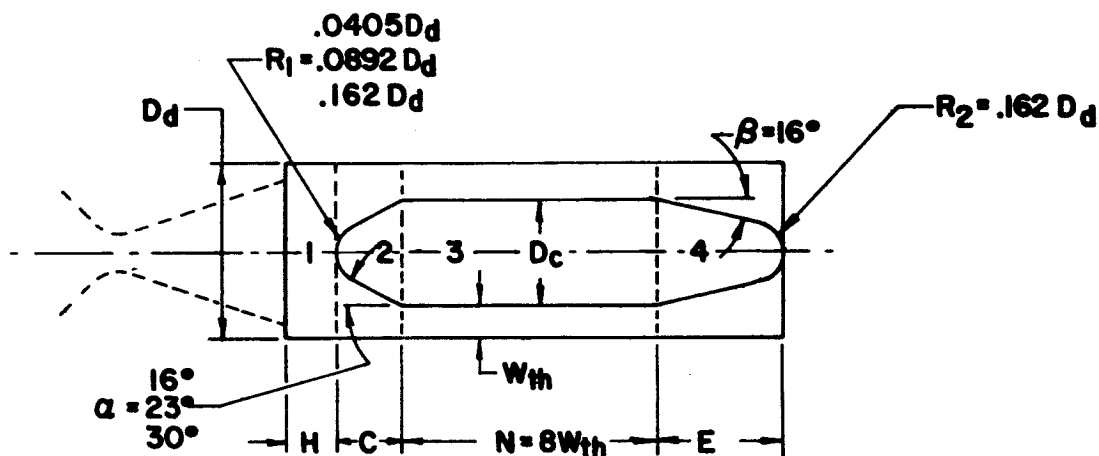


Figure IV-1  
Centerbody Diffuser Layout  
1/15 Scale Model  
IV-2



### SECOND THROAT DIFFUSER



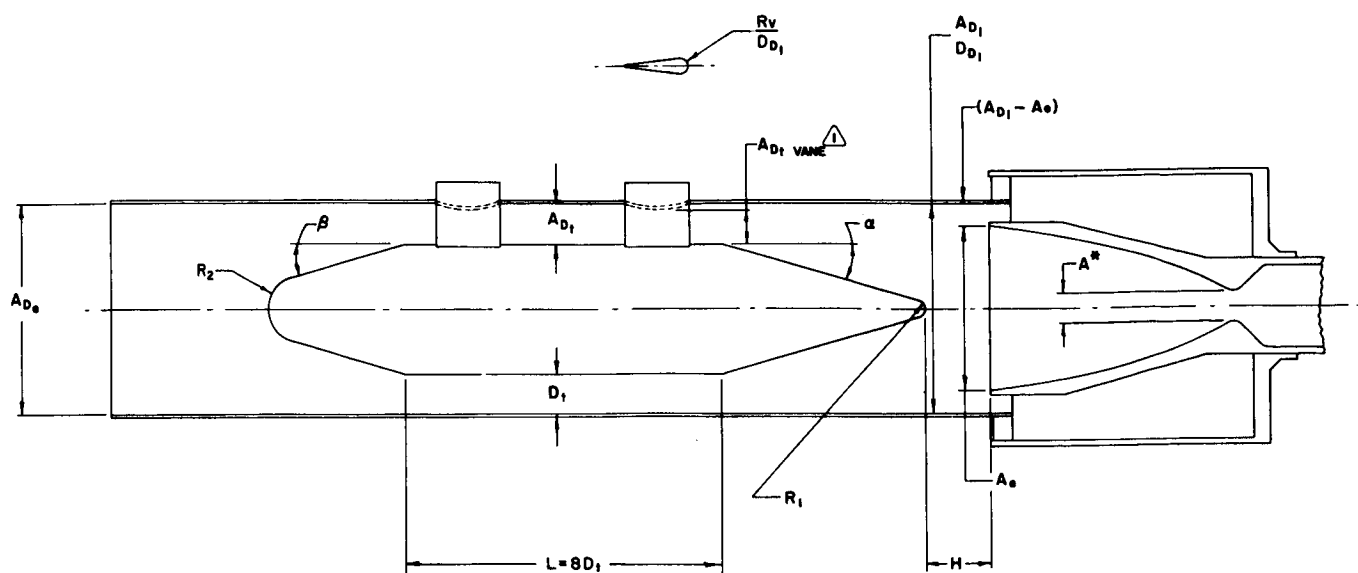
### CENTERBODY DIFFUSER

Both types may be constructed with 4 distinct sections characterized by the parameters as shown below:

Sections	Second-Throat Diffuser	Centerbody Diffuser
(1) Straight Duct Entrance Section	duct diam. $D_d$ length $H$	duct diameter $D_d$ length $H$
(2) Convergent Flow Section	cone angle length $C$	spike tip angle spike tip radius $R_1$ length $C$
(3) Constant Area Section	Second throat diam. $D_{th}$ , length $N = 8 D_{th}$	center body diameter $D_c$ width of annular passage $W_{th}$ , length $N = 8 W_{th}$
(4) Divergent Flow Section	cone angle length $E$	spike tail angle spike tail radius $R_2$ length $E$

Figure IV-1a

Comparison of a Centerbody Diffuser  
to an Equivalent Second-Throat Diffuser



$\frac{A_e}{A^*}$	$\frac{A_{D1}}{A^*}$	$\frac{A_{Dt}}{A^*}$	$\frac{A_{Dt}}{A^*_{VANE}}$	$\frac{A_{D1}}{A_{Dt}}$	$\frac{A_{D1}}{A_{Dt VANE}}$	$\frac{A_{De}}{A_{Dt}}$	$\frac{A_{De}}{A_{Dt VANE}}$	$\frac{A_{D1} - A_e}{A^*}$	$\frac{H}{D_{D1}}$	$\alpha$	$\beta$	$\frac{R_1}{D_{D1}}$	$\frac{R_2}{D_{D1}}$	$\frac{R_v}{D_{D1}}$
40	61.5	38.2	34.6	1.61	1.78	1.61	1.78	21.5	0.3	16° 23° 30°	16°	.0405 .0892 .1620	.165	.0405

NOSEPIECE CONFIGURATIONS	$\frac{R_1}{D_{D1}}$	$\alpha$
039-16	.0405	16
039-23	.0405	23
039-30	.0405	30
087-16	.0892	16
087-23	.0892	23
087-30	.0892	30
158-16	.1620	16
158-23	.1620	23
158-30	.1620	30

△ MINIMUM FRONTAL ANNULAR AREA BETWEEN VANES

Figure IV-1b  
Centerbody Diffuser Parameters

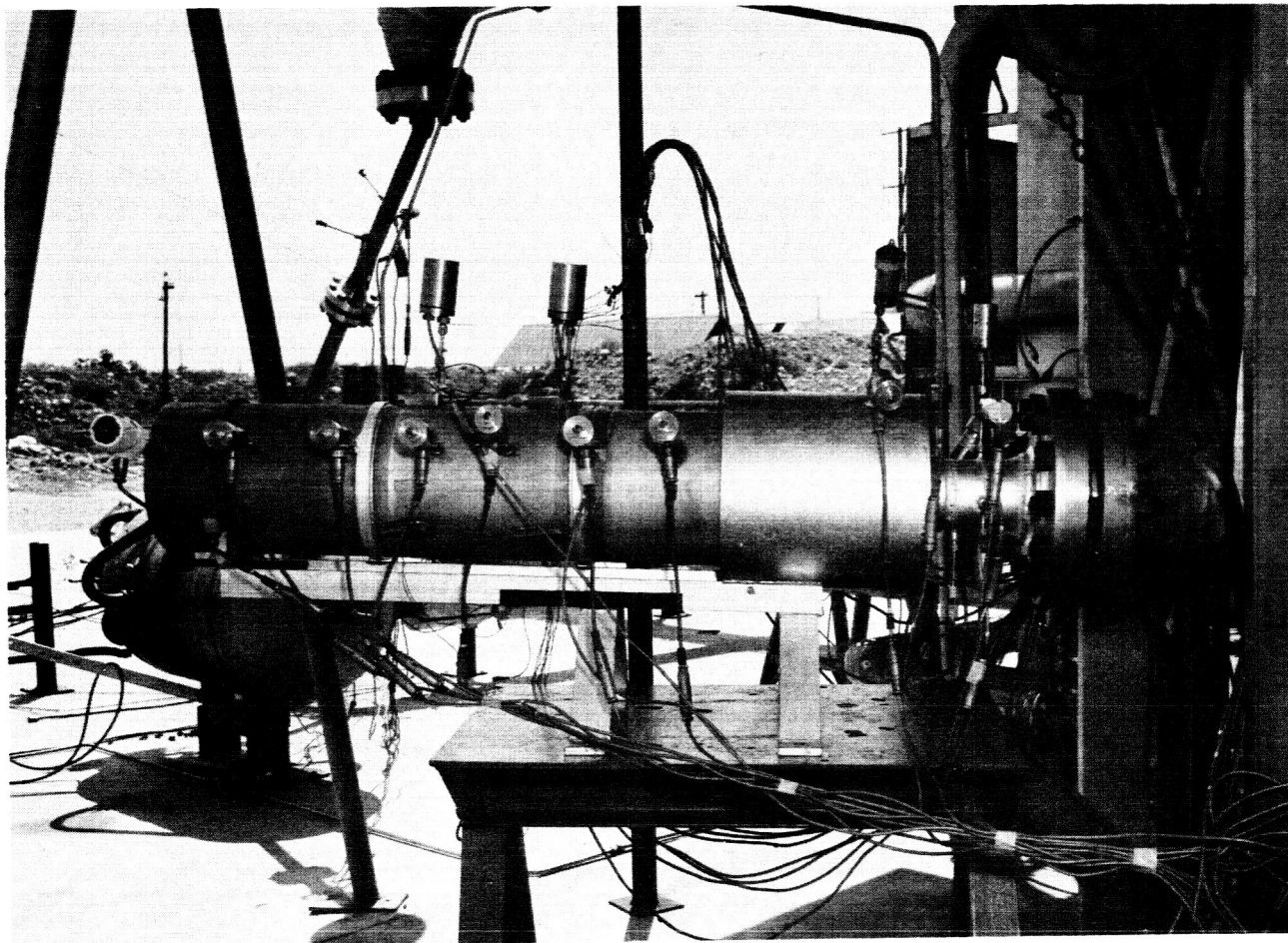


Figure IV-2

NERVA II Centerbody Diffuser  
1/15 Scale Model

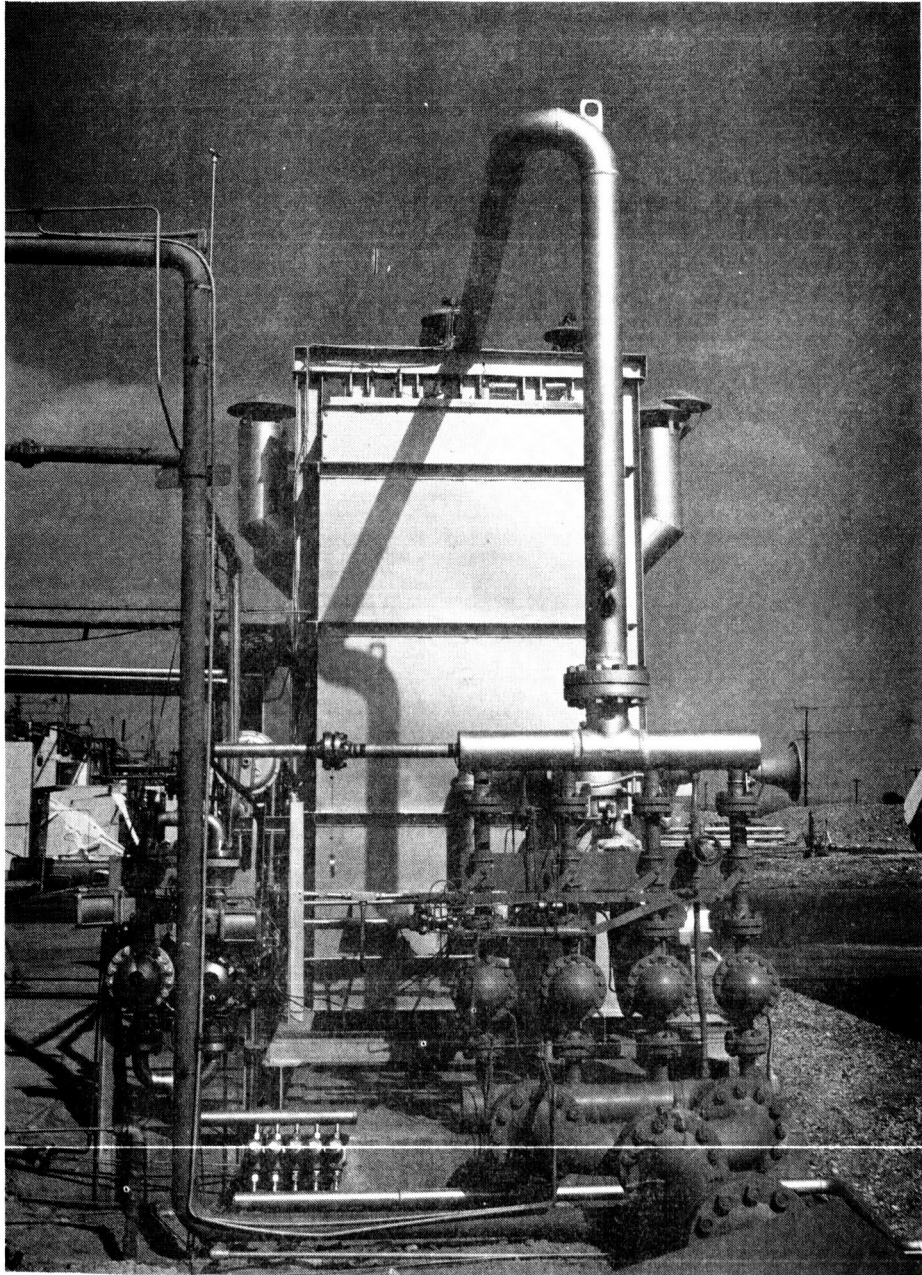


Figure IV-3

Stored Energy Heater, Azusa Proving Grounds

## B. CENTERBODY DIFFUSERS

The 1/15 scale-model centerbody diffuser is shown in Figure IV-1. Nine variations in nose cone configuration were tested; overall nose cone length varied according to differing nose radii and cone half angles, but the spacing between the nozzle exit and the tip of the nose cone was held constant at  $0.3 D_d$  by repositioning the diffuser duct into the engine compartment for each of the nine nose cone configurations. The two nose cone geometrical parameters were varied to obtain nine unique test pieces as listed below:

<u>Nosecone Configuration</u>	<u>Nose Radius (<math>R/D_d</math>)</u>	<u>Cone Half Angle</u>
1	0.0405	16°
2	0.0405	23°
3	0.0405	30°
4	0.0892	16°
5	0.0892	23°
6	0.0892	30°
7	0.162	16°
8	0.162	23°
9	0.162	30°

Only one aft cone was used for all of the tests and its geometry was: tail radius of  $R/D_d = 0.162$  and cone half angle of 16°. The centerbody was suspended in the center of the diffuser duct by six aerodynamic vanes, three fore and three aft, in-line, as indicated in Figure IV-4. The vanes were spaced radially at 120°. The leading edge radius of the vanes was  $R = 0.0405 D_d$  which corresponds to the smallest nosecone radius tested.

## C. FABRICATION TECHNIQUES

The three small radius nose cones are shown in Figures IV-5 and IV-6. Intermediate radius nose cones are shown in Figure IV-7 and IV-8. Figures IV-9 and IV-10 show the large radius nose cones.

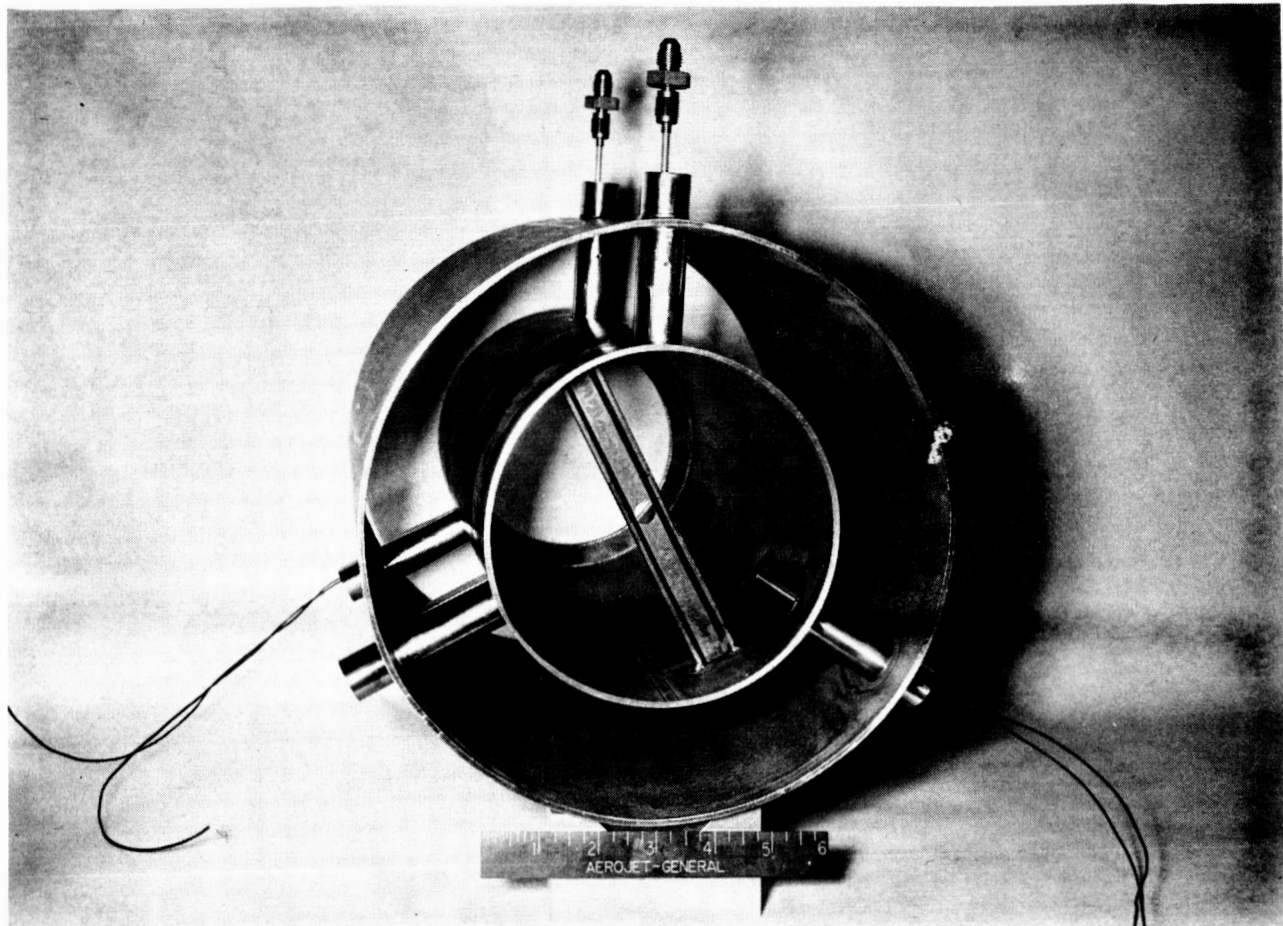


Figure IV-4  
Centerbody Weldment, Downstream View

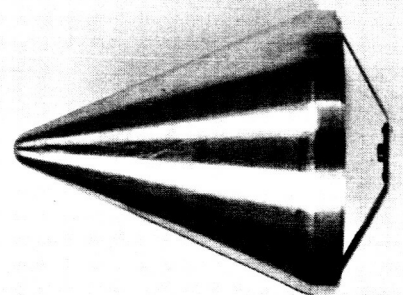
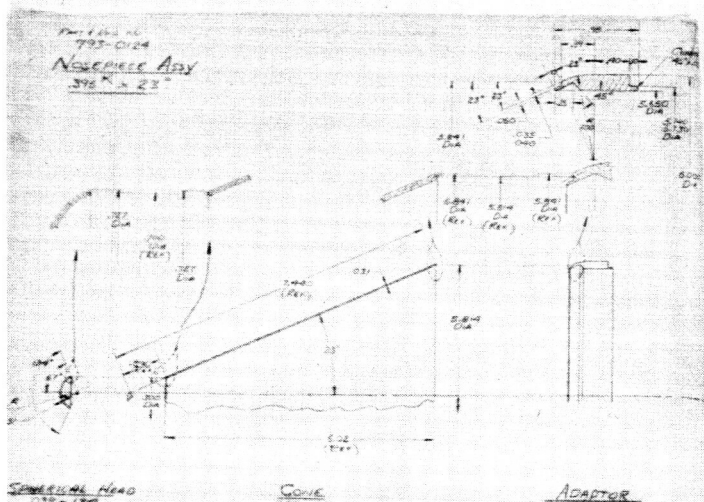
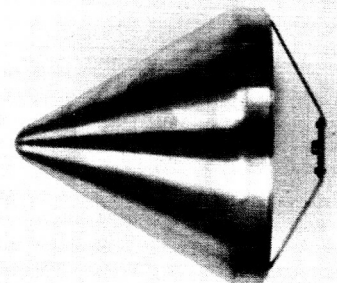
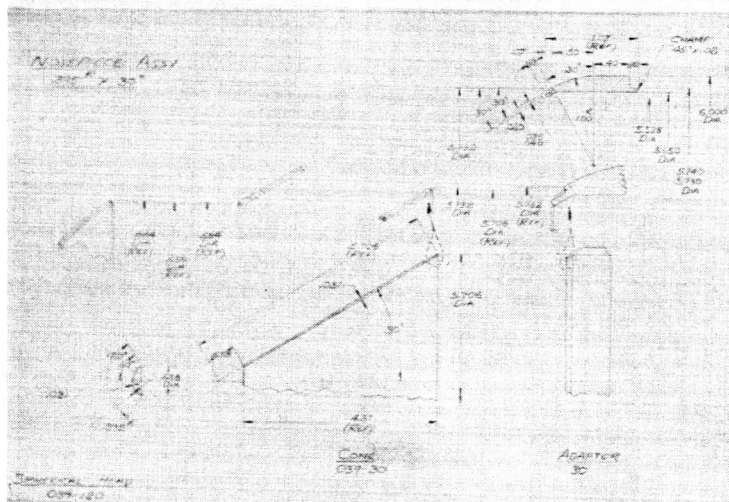
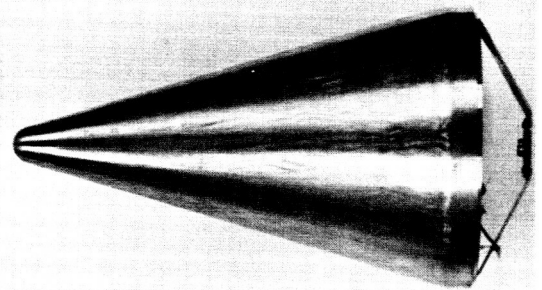
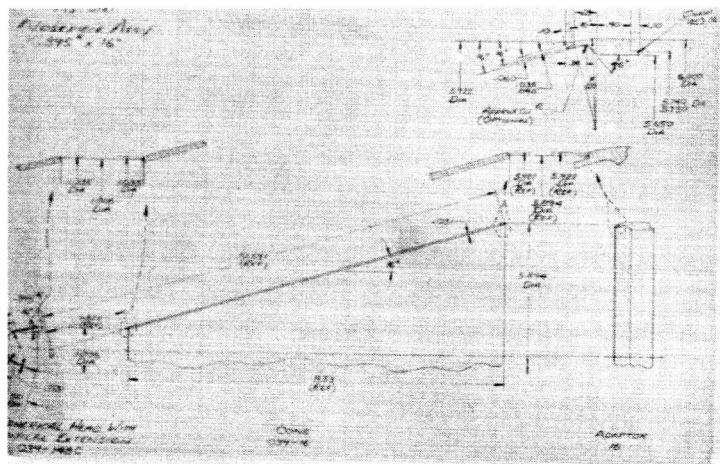


Figure IV-5

Small Radius Nosecones with Specifications

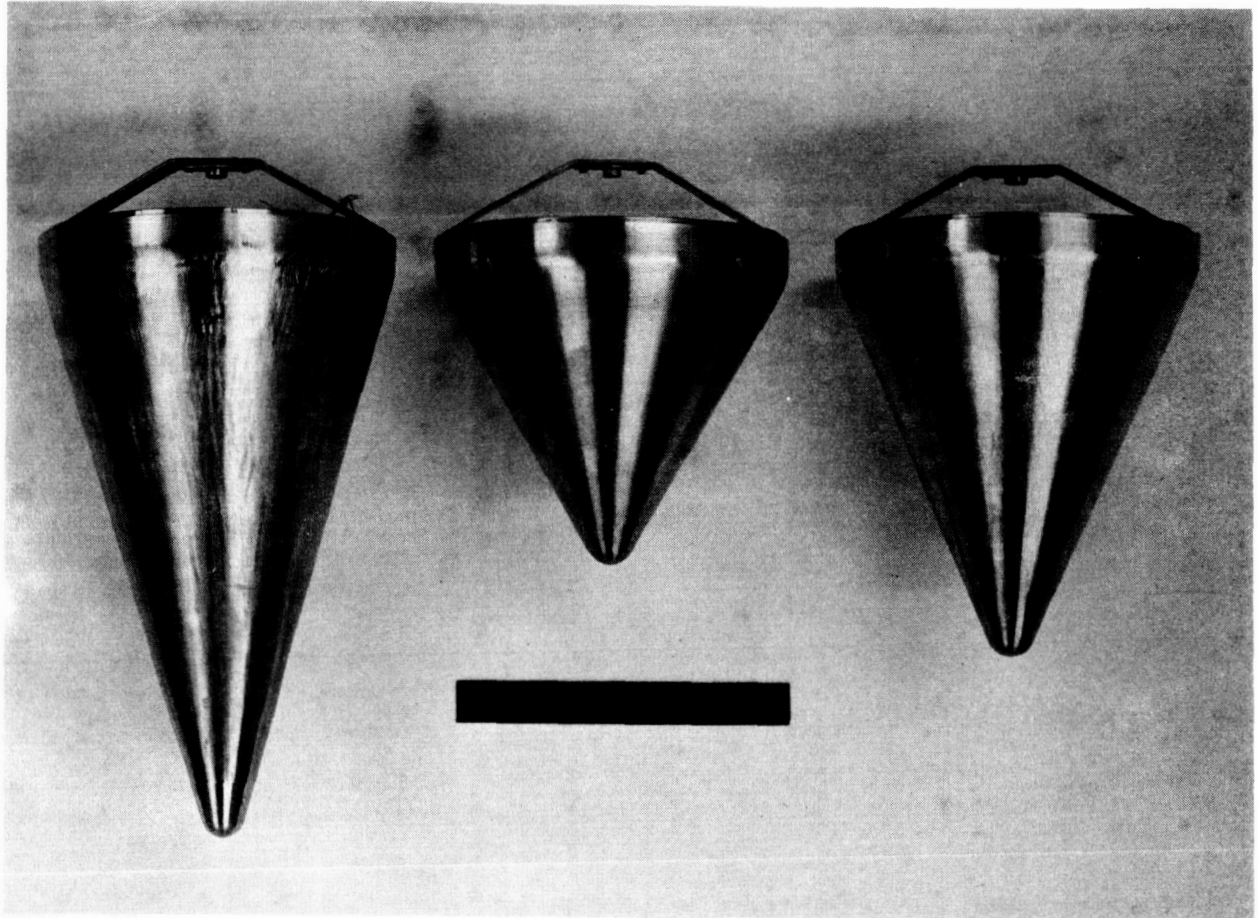


Figure IV-6

Small Radius Nosecones, A Closeup Photograph

IV-10

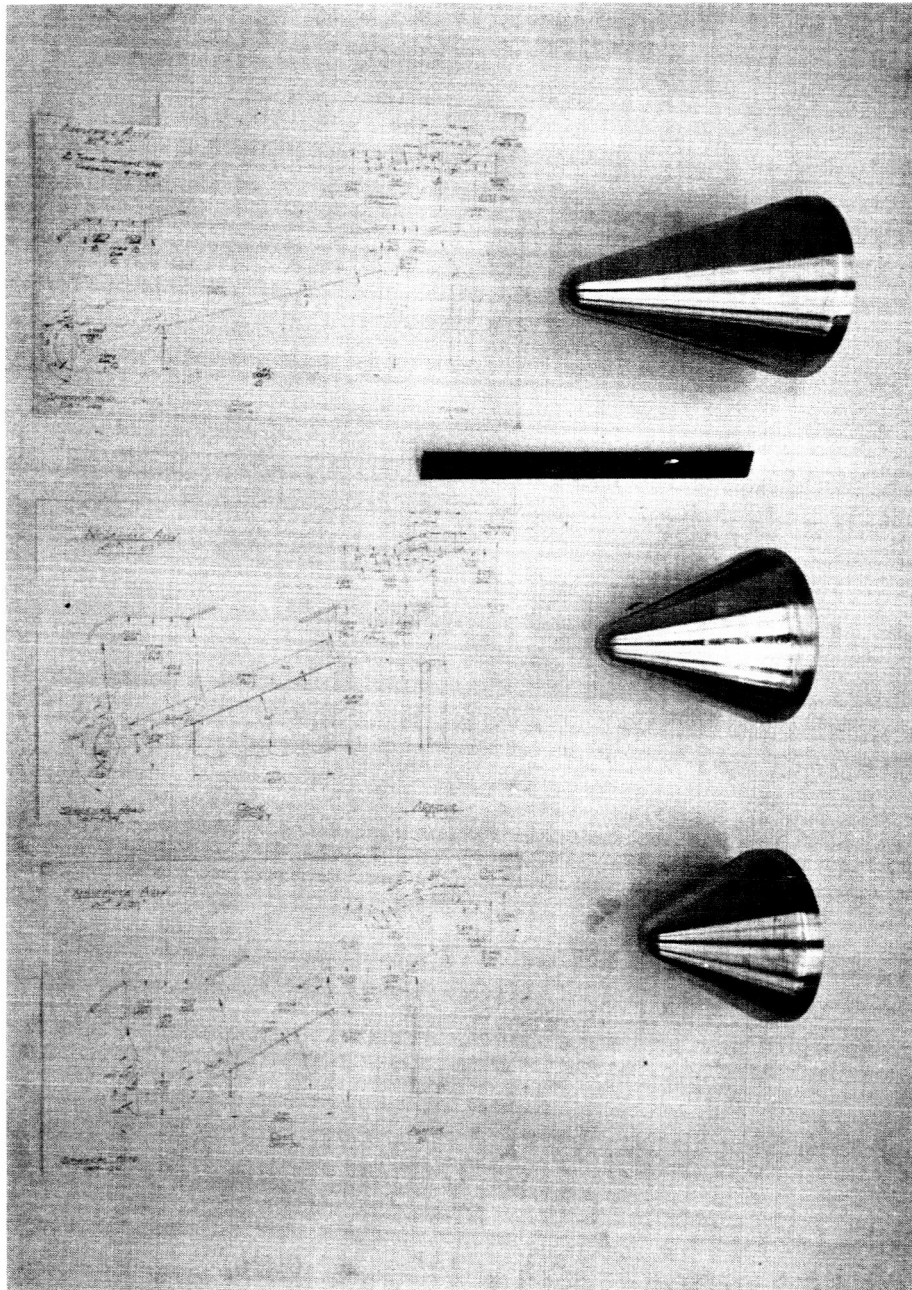


Figure IV-7

Intermediate Radius Nosecones with Specifications

IV-11

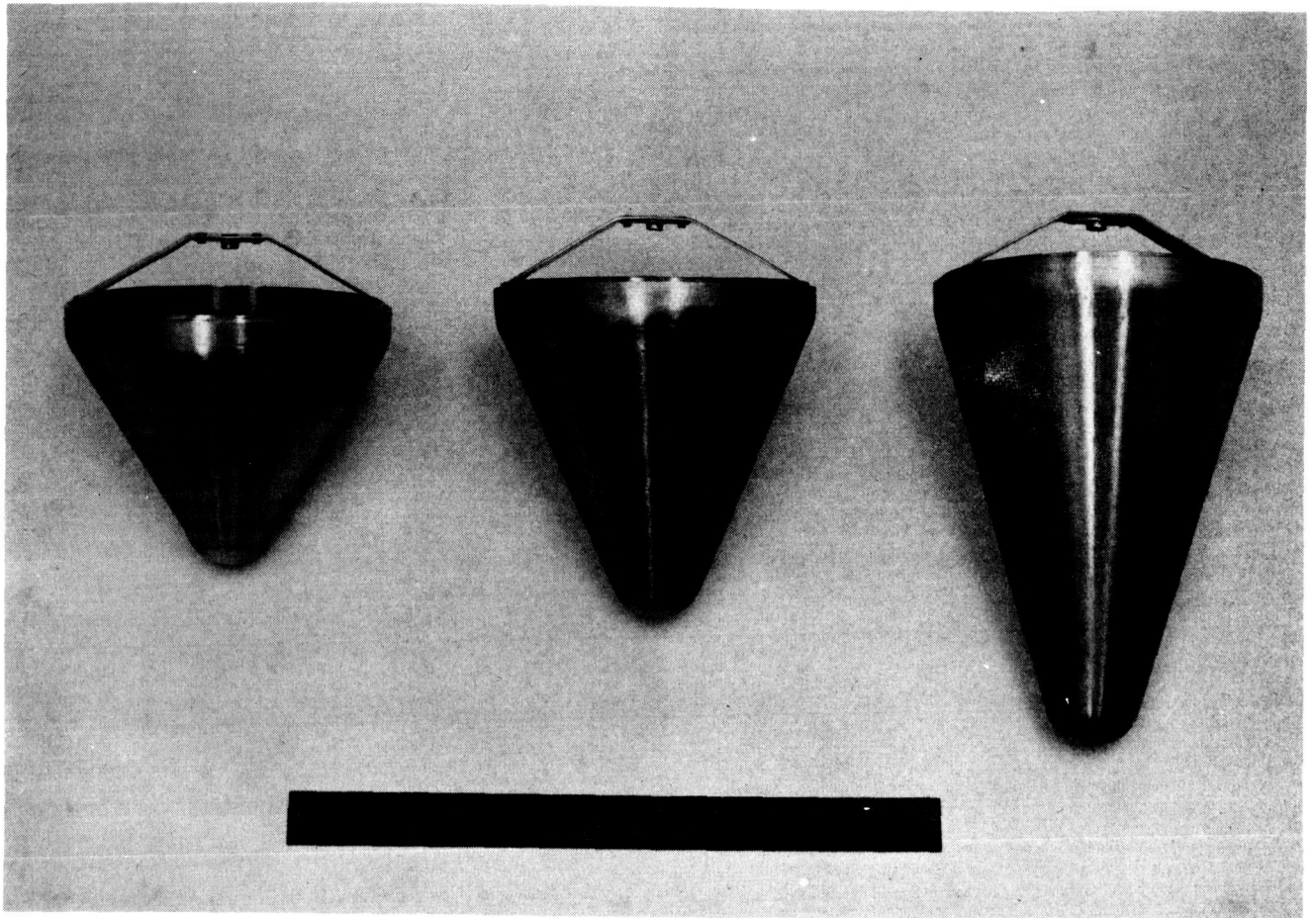


Figure IV-8

Intermediate Radius Nosecones, A Closeup Photograph

IV-12

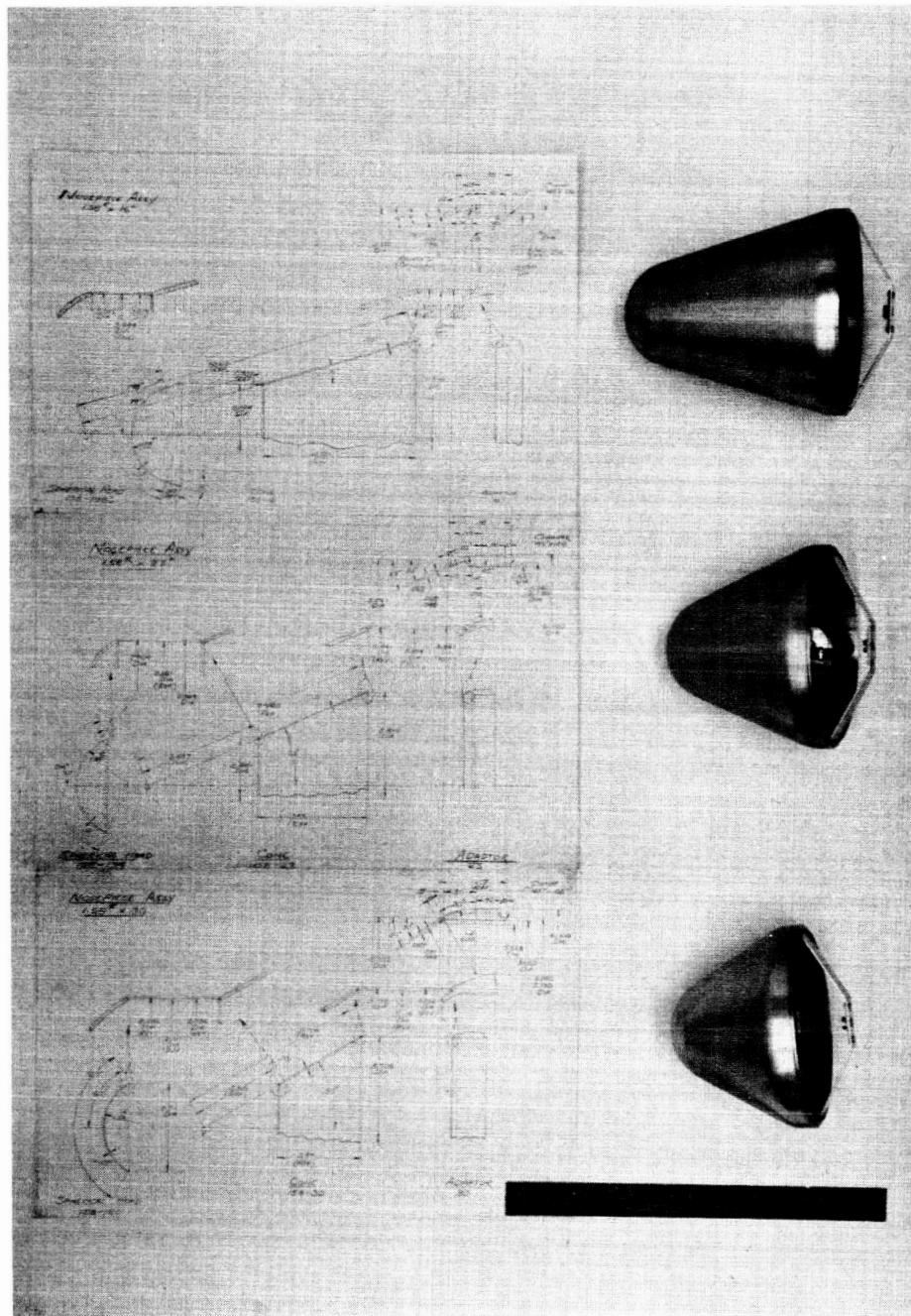


Figure IV-9

Large Radius Nosecones with Specifications

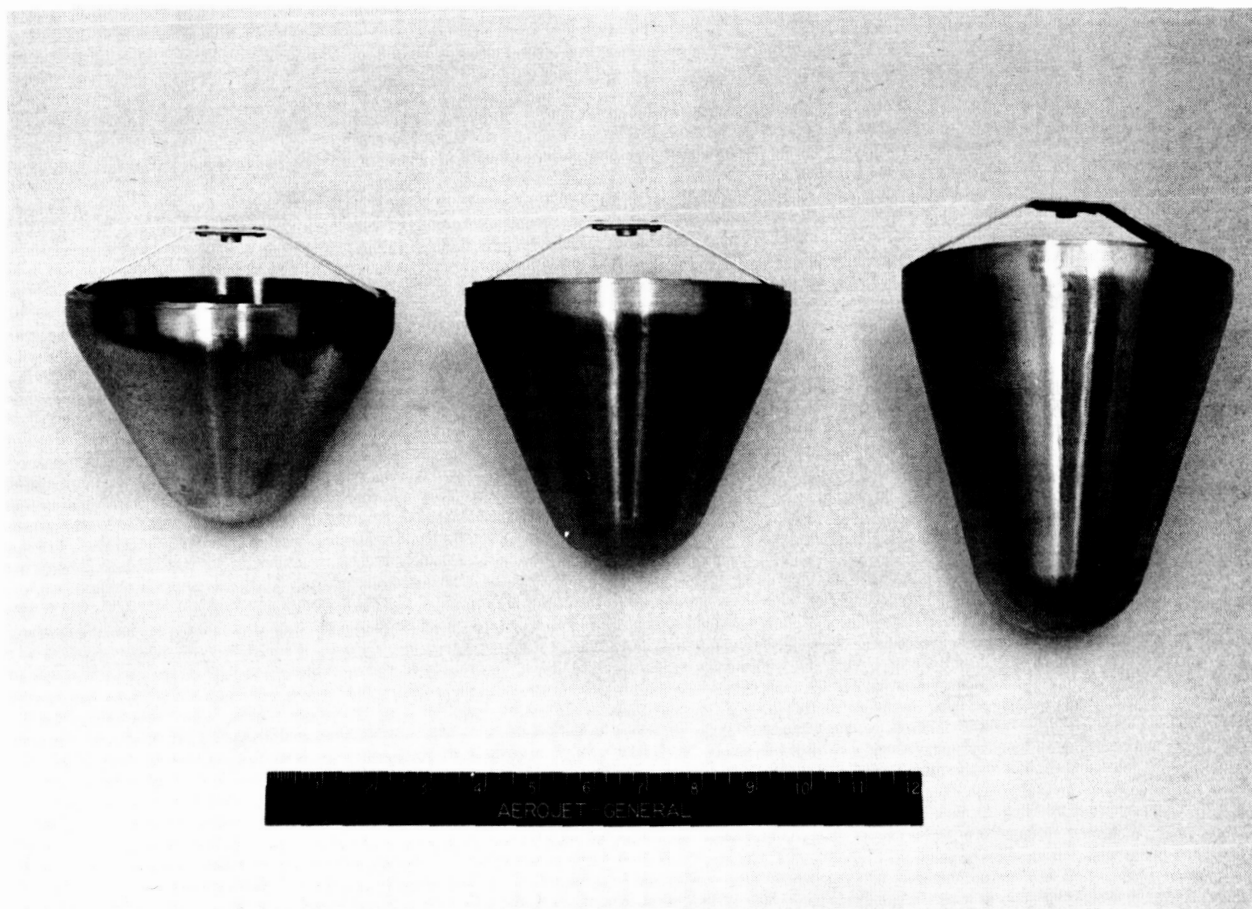


Figure IV-10

Large Radius Nosecones, A Closeup Photograph

IV-14

Thermocouples were attached every  $10^\circ$  to the inside of the noses and every 0.50-in. along the inside of the cones. Notice in Figure IV-11 that these operations were performed before the noses were welded to the cones; otherwise, the thermocouples could not have been attached because of inaccessability.

The actual welding of the noses to the cones was very critical, because of the thin (0.030-in.) material thicknesses used. It was essential that no weld joint mismatches occurred that would disturb the flow from the intended pattern, thereby affecting the heat transfer to be measured by the thermocouples.

In order to accomplish this butt weld, a special welding fixture had to be developed (Figure IV-12). The weld fixture:

1. Forced the end of the cone into a circular shape by "stretching" it over a mandrel.
2. Forced the nose into a circular shape by compressing it with a cup-ended cylinder over the same mandrel as mentioned above.
3. Compressed the two nosepiece parts together and held them solidly despite the thermal stresses of welding.
4. Provided an inert gas back up for the welding operation.

The welds produced were quite successful, as may be seen in Figure IV-6, IV-8 and IV-10.

An interior view of a nosecone may be seen in Figure IV-13 which shows the thermocouple lead-out wires. These wire bundles were threaded through the hollow vanes supporting the centerbody (Figures IV-4, IV-14, IV-15 and IV-16) where attachment was made to the monitoring system. Note the total pressure taps on two of the vanes in the photographs, also four thermocouples were spotted inside, under the leading edge, of two vanes.

Three views of the centerbody diffuser on the test stand at the Azusa Proving Grounds are shown in Figures IV-2, IV-16 and IV-17.

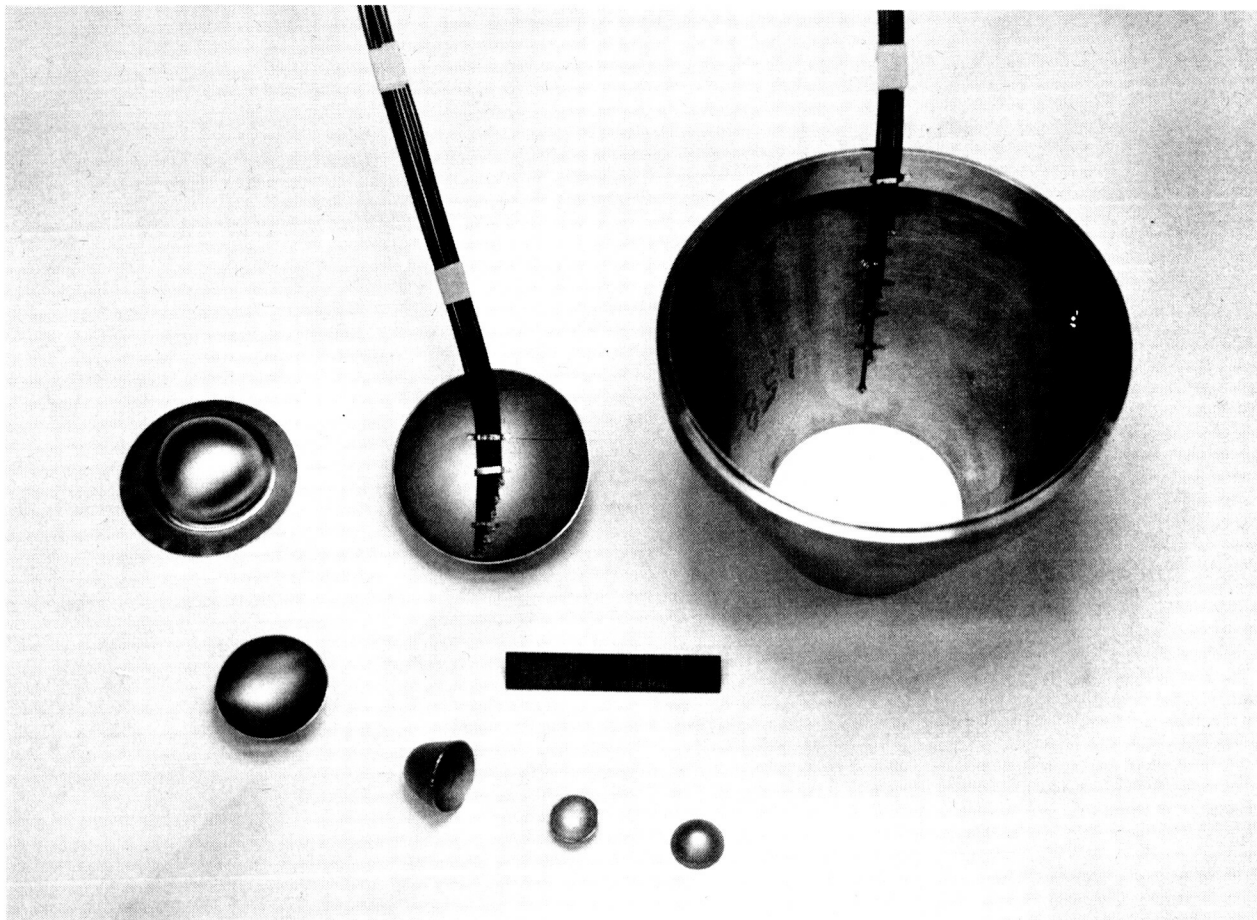


Figure IV-11

Thermocouples attached to Nose and Cone prior to Final Weld

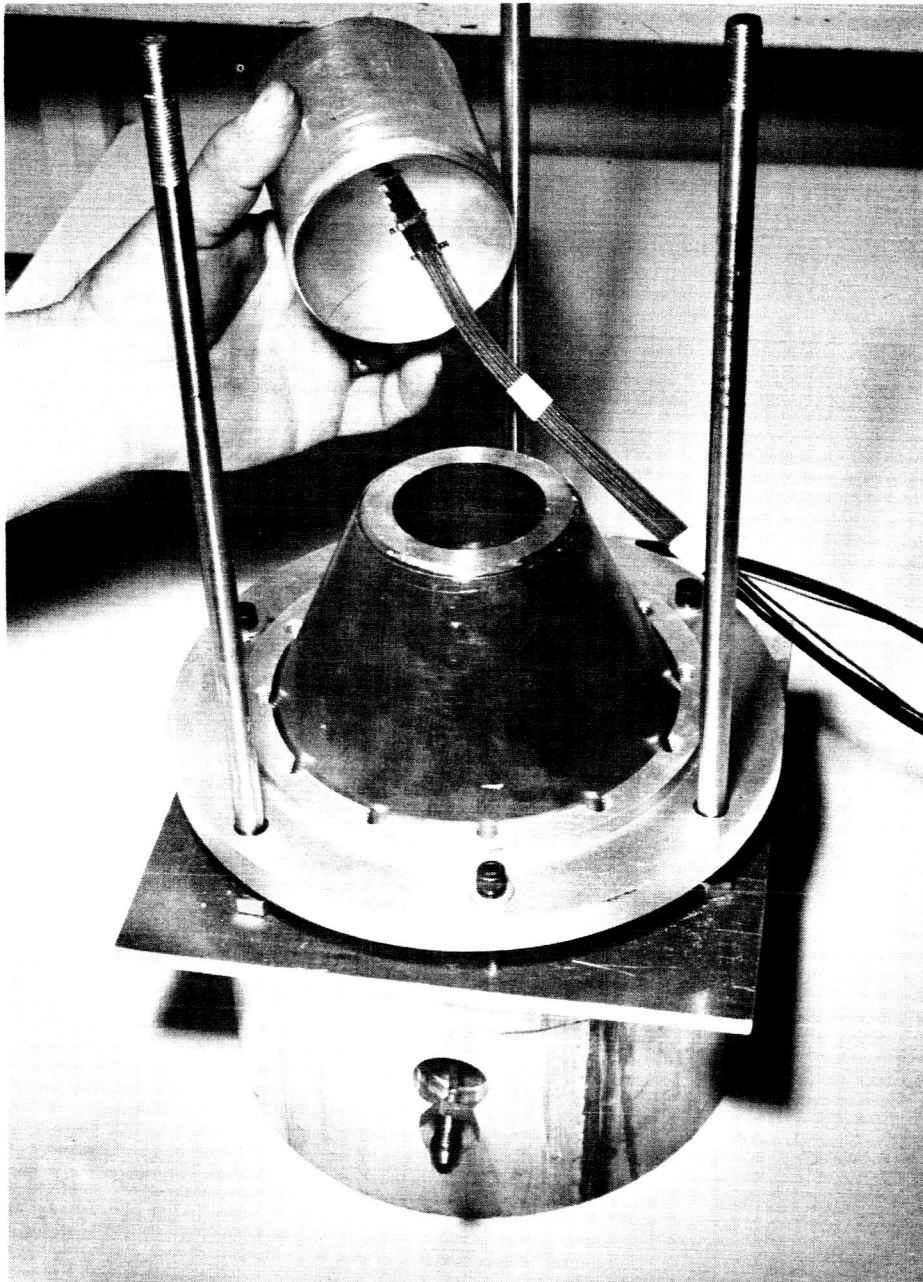


Figure IV-12

Special Welding Fixture for Nose to Cone Weld Joint

IV-17

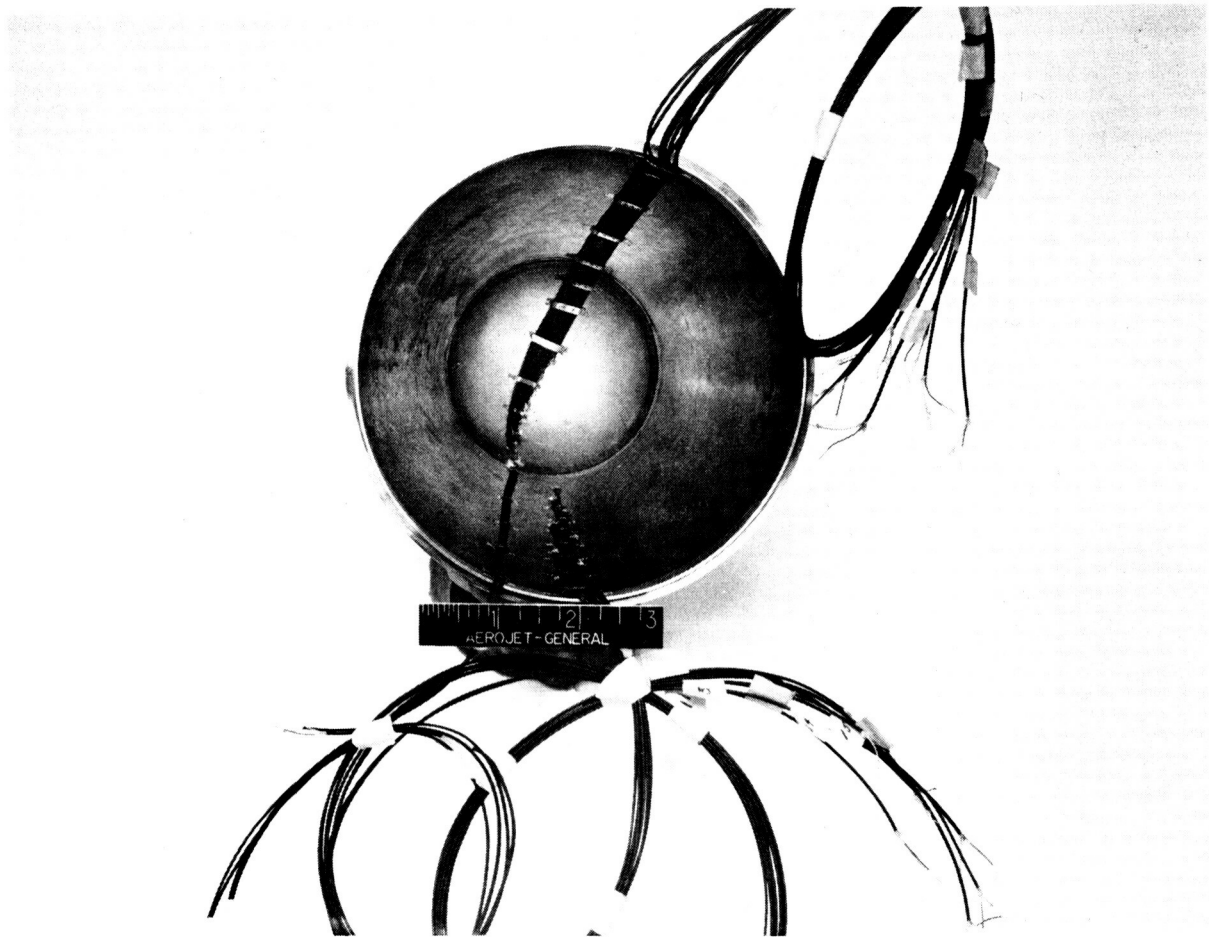


Figure IV-13

Thermocouple Wires on the Interior of Nosecone

IV-18

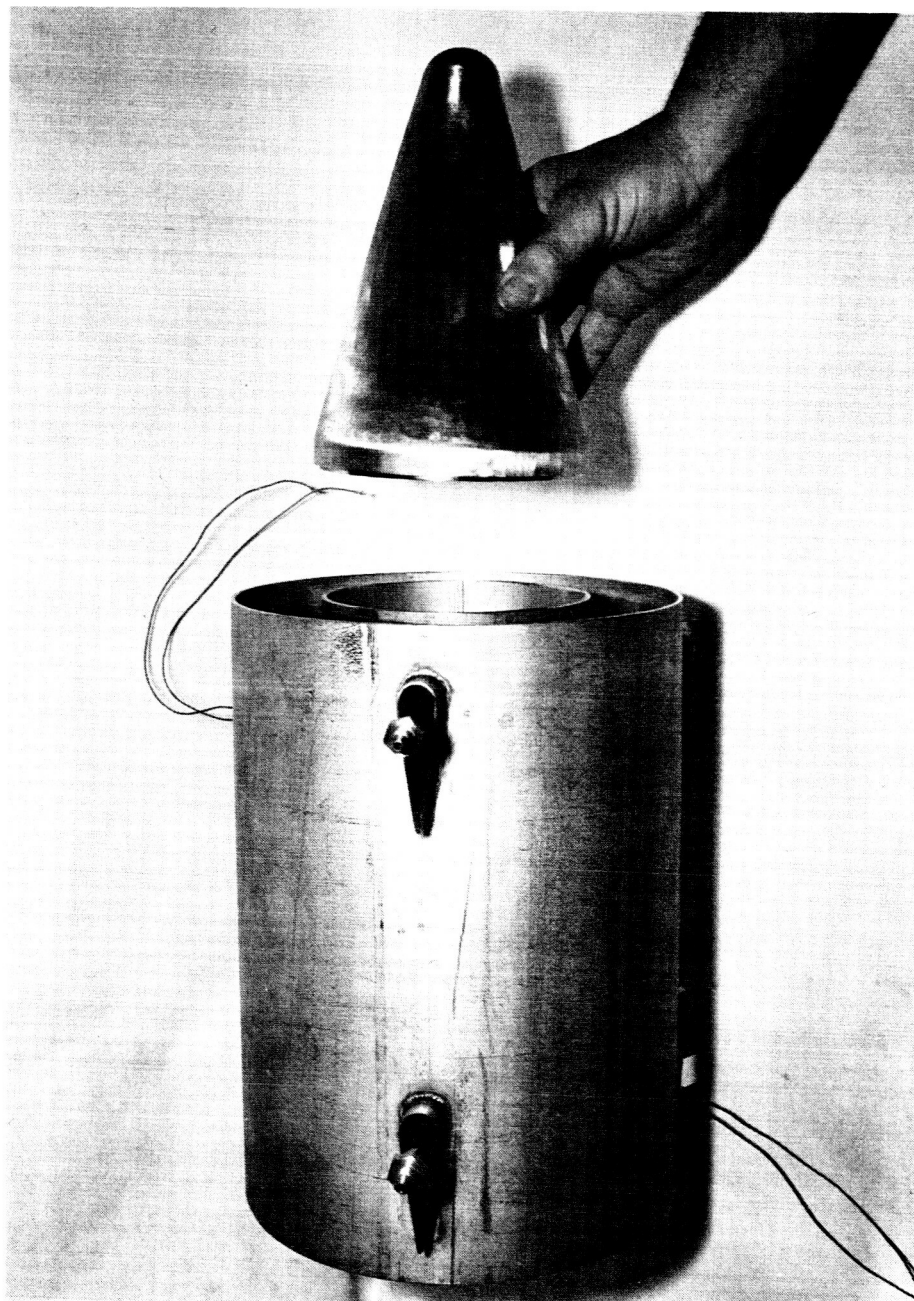


Figure IV-14

Centerbody Weldment - Side View

IV-19

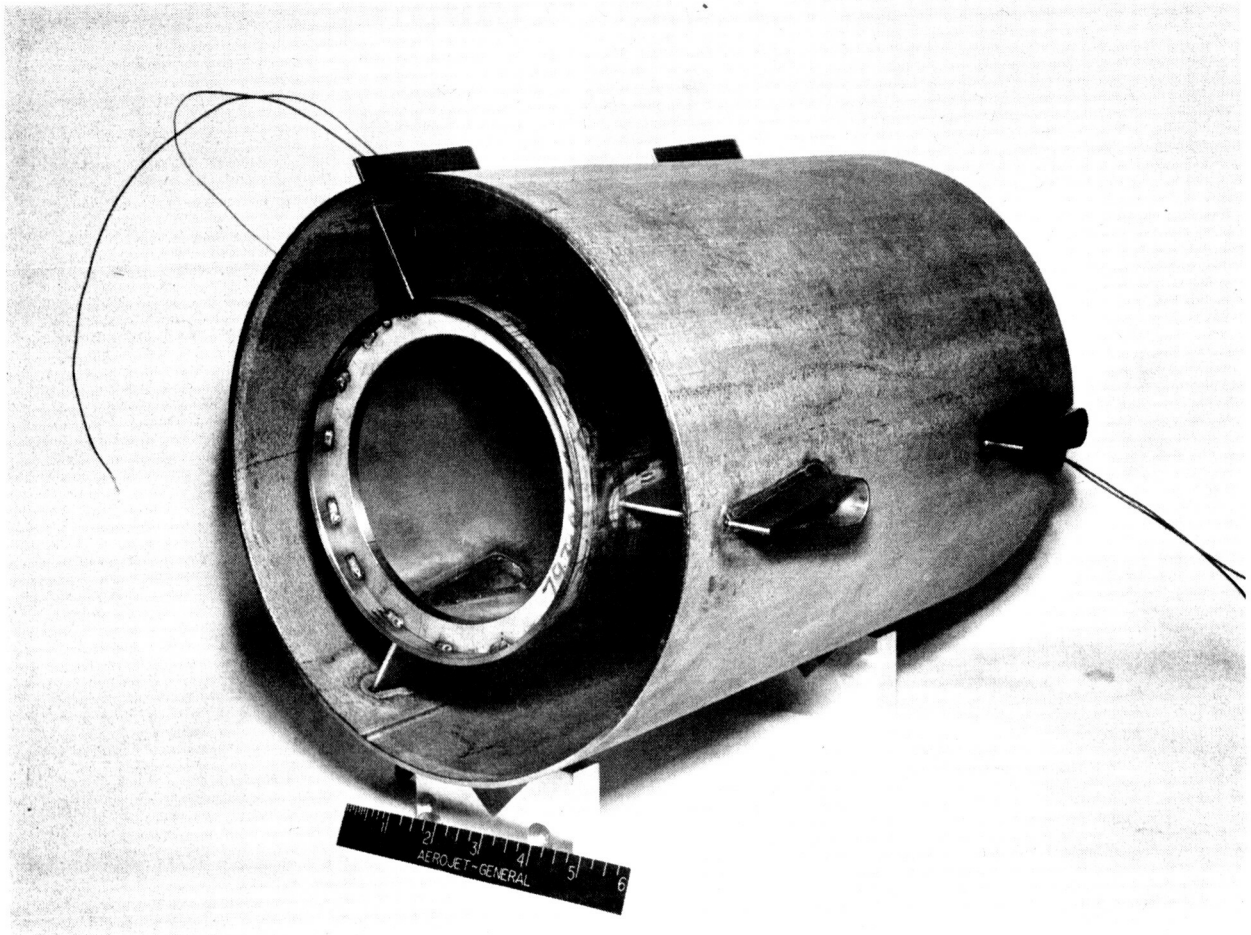


Figure IV-15

Centerbody Weldment - Upstream View

IV-20

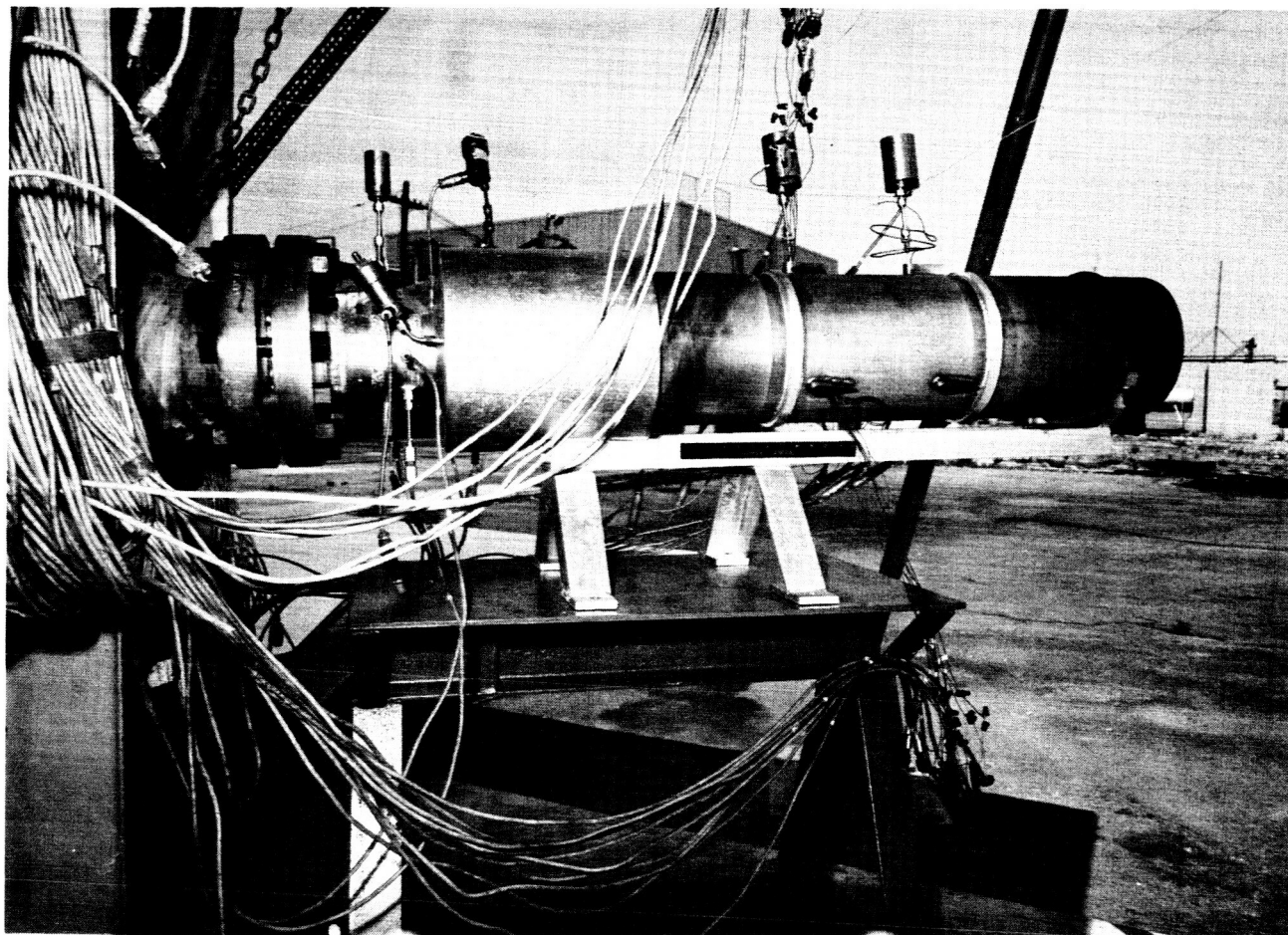


Figure IV-16

NERVA II Centerbody Diffuser

Note Thermocouple Wires in Vane

IV-21

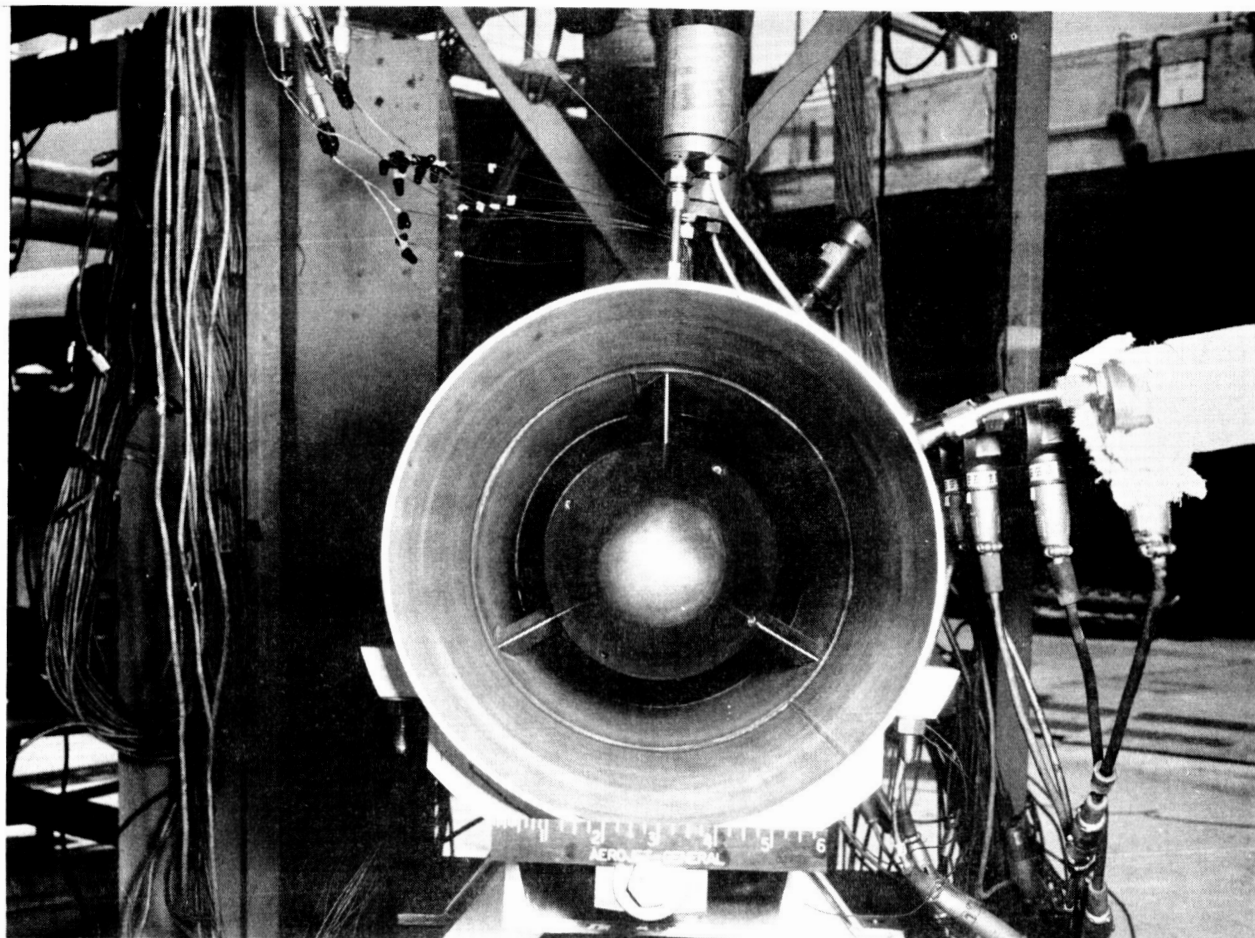


Figure IV-17

NERVA II Centerbody Diffuser, Upstream View

#### D. INSTRUMENTATION

To fulfill the objectives of the 1/15 scale model centerbody diffuser program, instrumentation was provided to measure the primary chamber pressure and temperature, nozzle exit pressure, cell pressure, various static pressures along the duct wall, total pressure at the stagnation point on a front and on a rear strut, transient skin temperature on the centerbody nose cone, transient skin temperature at the stagnation point of a front and rear strut, and the transient skin temperature at the aft section (at the centerbody axis) of the centerbody.

All pressure measurements except ambient were taken using Wiancko pressure transducers and were recorded on oscillographs. The transducers that recorded pressures at less than atmospheric were referenced to a vacuum through use of a vacuum pump with vacuum manifolds extending to each transducer to enable more accurate measurements to be made. The ambient pressure was measured with a mercury manometer and corrected for ambient temperature effects.

All temperature measurements were taken with chromel-alumel thermocouples. A high speed internal sampling switch was used to sample the induced voltage of each thermocouple at the rate of 75 samples per second. Each thermocouple voltage was immediately transferred to IBM magnetic tape which stored the voltage for future use.

Table IV-1 lists the important characteristics of the instrumentation used and Figure IV-18 shows the location of this instrumentation. Figures IV-19 to IV-21 show the location of the thermocouples in the various centerbody nose pieces.

Table IV-1  
Instrumentation Characteristics

FUNCTION	SYMBOL	INSTRUMENTATION	RANGE
CHAMBER PRESSURES	$P_{C-1}$ & $P_{C-3}$	WIANCKO PRESSURE TRANSDUCER	0 to 1000 PSIG
CHAMBER TEMPERATURES	$T_{C_1}$ & $T_{C_2}$	C/A THERMOCOUPLE	490 to 3000 °R
CELL PRESSURE	$P_V$	WIANCKO PRESSURE TRANSDUCER	0 to 20 PSIA
NOZZLE EXIT PRESSURE	$P_{NE}$	WIANCKO PRESSURE TRANSDUCER	0 to 20 PSIA
DUCT WALL PRESSURES	$P_{D-1}$ to $P_{D-7}$	WIANCKO PRESSURE TRANSDUCER	0 to 20 PSIA
FRONT STRUT STAGNATION PRESSURE	$P_{TV-1}$	WIANCKO PRESSURE TRANSDUCER	0 to 50 PSIG
REAR STRUT STAGNATION PRESSURE	$P_{TV-2}$	WIANCKO PRESSURE TRANSDUCER	0 to 50 PSIG
FRONT STRUT STAGNATION TEMP. (INNER)	$T_{F1}$	C/A THERMOCOUPLE	490 to 3000 °R
FRONT STRUT STAGNATION TEMP. (OUTER)	$T_{FO}$	C/A THERMOCOUPLE	490 to 3000 °R
REAR STRUT STAGNATION TEMP. (INNER)	$T_{R1}$	C/A THERMOCOUPLE	490 to 3000 °R
REAR STRUT STAGNATION TEMP. (OUTER)	$T_{RO}$	C/A THERMOCOUPLE	490 to 3000 °R
CENTERBODY NOSECONE TEMPERATURES	$T_1, T_2, T_3$ --- $T_n$	C/A THERMOCOUPLE	490 to 3000 °R
CENTERBODY AFT TEMPERATURE	$T_A$	C/A THERMOCOUPLE	490 to 3000 °R

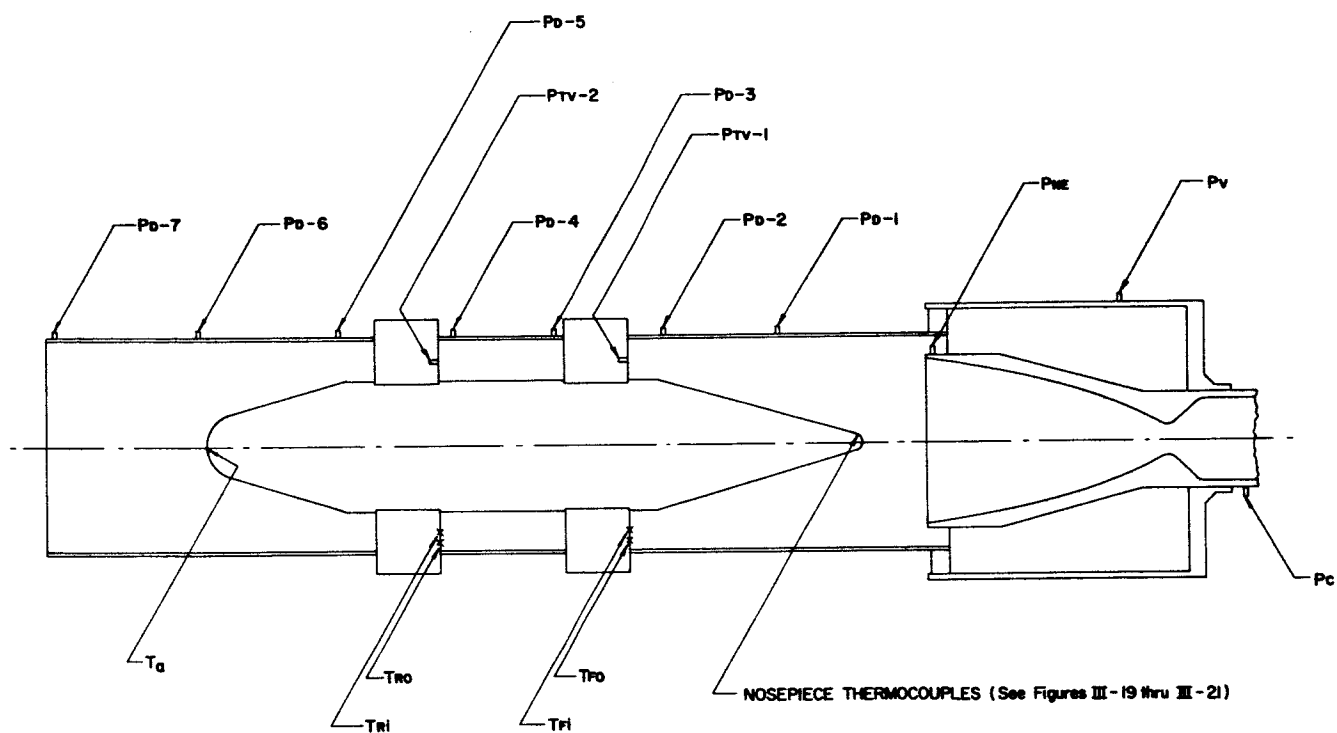
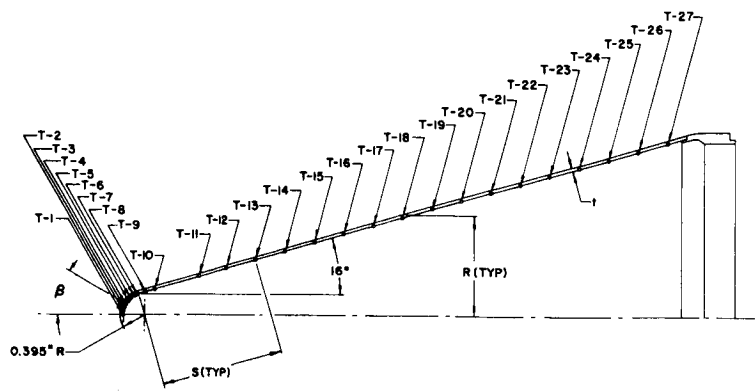
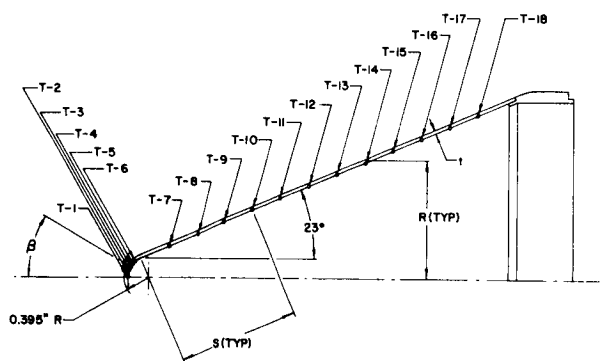


Figure IV-18  
 Instrumentation Locations  
 1/15 Scale-Model Centerbody Diffuser  
 IV-25



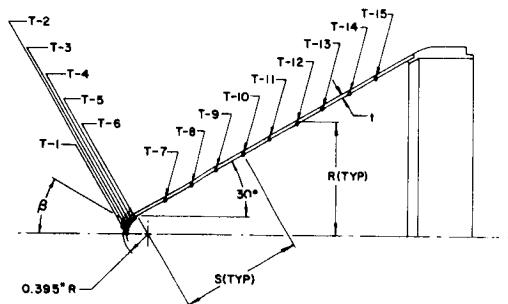
THERMOCOUPLE NO.	MATERIAL THICKNESS(t)	ANGLE (β) or RADIUS (R)	S
T-1	0.0296	0°	-
T-2	0.0292	10°	-
T-3	0.0286	20°	-
T-4	0.0288	30°	-
T-5	0.0275	40°	-
T-6	0.0270	50°	-
T-7	0.0271	60°	-
T-8	0.0278	70°	-
T-9	0.0280	0.41	0.10
T-10	0.0290	0.46	0.30
T-11	0.0292	0.66	1.00
T-12	0.0288	0.79	1.50
T-13	0.0290	0.93	2.00
T-14	0.0290	1.07	2.50
T-15	0.0290	1.21	3.00
T-16	0.0290	1.36	3.50
T-17	0.0290	1.48	4.00
T-18	0.0288	1.62	4.50
T-19	0.0284	1.76	5.00
T-20	0.0283	1.90	5.50
T-21	0.0280	2.03	6.00
T-22	0.0282	2.17	6.50
T-23	0.0283	2.31	7.00
T-24	0.0284	2.45	7.50
T-25	0.0278	2.59	8.00
T-26	0.0283	2.72	8.50
T-27	0.0285	2.86	9.00

NOSEPIECE -(0.395" radius x 16° cone)



THERMOCOUPLE NO.	MATERIAL THICKNESS(t)	ANGLE (β) or RADIUS (R)	S
T-1	0.0302	0°	-
T-2	0.0300	10°	-
T-3	0.0291	20°	-
T-4	0.0282	30°	-
T-5	0.0280	40°	-
T-6	0.0274	50°	-
T-7	0.0272	0.57	0.50
T-8	0.0270	0.77	1.00
T-9	0.0266	0.97	1.50
T-10	0.0269	1.18	2.00
T-11	0.0288	1.38	2.50
T-12	0.0299	1.58	3.00
T-13	0.0299	1.79	3.50
T-14	0.0300	1.99	4.00
T-15	0.0296	2.19	4.50
T-16	0.0292	2.40	5.00
T-17	0.0293	2.60	5.50
T-18	0.0292	2.80	6.00

NOSEPIECE -(0.395" radius x 23° cone)

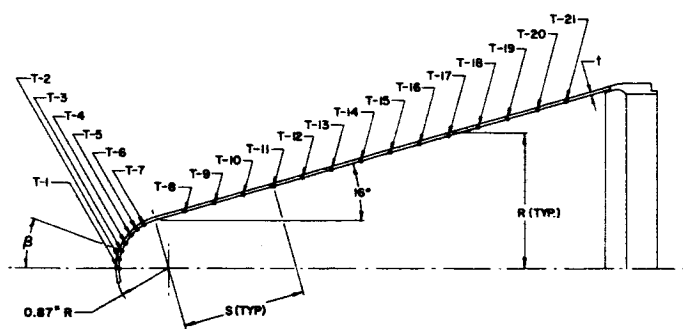


THERMOCOUPLE NO.	MATERIAL THICKNESS(t)	ANGLE (β) or RADIUS (R)	S
T-1	0.0289	0°	-
T-2	0.0284	10°	-
T-3	0.0278	20°	-
T-4	0.0274	30°	-
T-5	0.0274	40°	-
T-6	0.0272	50°	-
T-7	0.0300	0.59	0.50
T-8	0.0316	0.84	1.00
T-9	0.0317	1.09	1.50
T-10	0.0312	1.34	2.00
T-11	0.0303	1.59	2.50
T-12	0.0296	1.84	3.00
T-13	0.0300	2.09	3.50
T-14	0.0290	2.34	4.00
T-15	0.0305	2.59	4.50

NOSEPIECE -(0.395" radius x 30° cone)

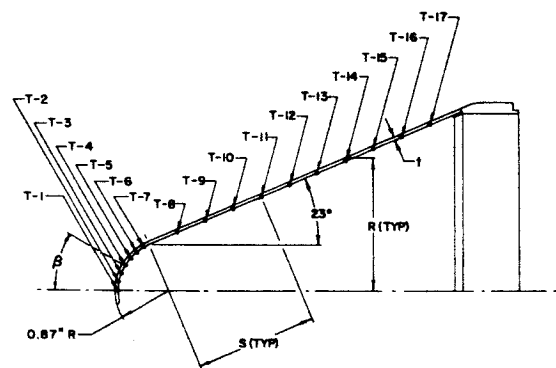
Figure IV-19

Thermocouple Locations - Small Radius Nosepieces



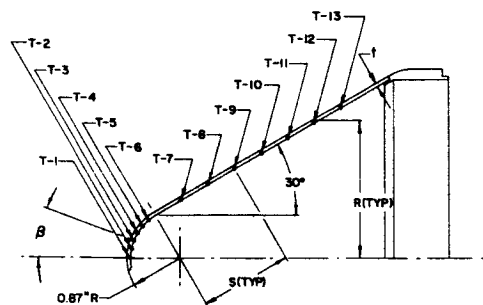
THERMOCOUPLE NO.	MATERIAL THICKNESS (t)	ANGLE (β) or RADIUS (R)	S
T-1	0.0202	0°	—
T-2	0.0199	10°	—
T-3	0.0203	20°	—
T-4	0.0211	30°	—
T-5	0.0220	40°	—
T-6	0.0228	50°	—
T-7	0.0239	60°	—
T-8	0.0292	0.98	0.50
T-9	0.0290	1.12	1.00
T-10	0.0293	1.25	1.50
T-11	0.0290	1.39	2.00
T-12	0.0287	1.53	2.50
T-13	0.0289	1.67	3.00
T-14	0.0290	1.80	3.50
T-15	0.0296	1.94	4.00
T-16	0.0290	2.08	4.50
T-17	0.0297	2.22	5.00
T-18	0.0300	2.36	5.50
T-19	0.0302	2.50	6.00
T-20	0.0304	2.63	6.50
T-21	0.0310	2.77	7.00

NOSEPIECE — (0.87" radius x 16° cone)



THERMOCOUPLE NO.	MATERIAL THICKNESS (t)	ANGLE (β) or RADIUS (R)	S
T-1	0.0203	0°	—
T-2	0.0204	10°	—
T-3	0.0205	20°	—
T-4	0.0210	30°	—
T-5	0.0215	40°	—
T-6	0.0228	50°	—
T-7	0.0240	60°	—
T-8	0.0300	0.99	0.50
T-9		1.19	1.00
T-10		1.39	1.50
T-11		1.58	2.00
T-12		1.78	2.50
T-13		1.97	3.00
T-14		2.17	3.50
T-15		2.36	4.00
T-16		2.56	4.50
T-17	0.0300	2.75	5.00

NOSEPIECE — (0.87" radius x 23° cone)

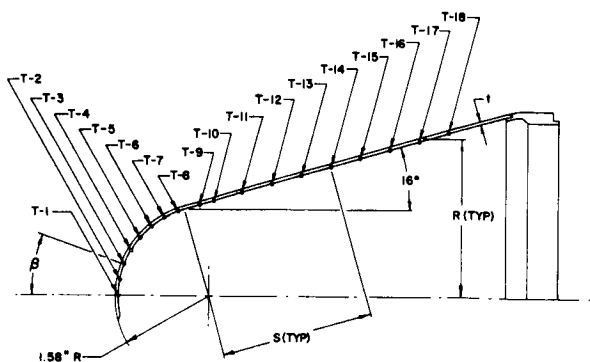


THERMOCOUPLE NO.	MATERIAL THICKNESS (t)	ANGLE (β) or RADIUS (R)	S
T-1	0.0200	0°	—
T-2	0.0201	10°	—
T-3	0.0205	20°	—
T-4	0.0210	30°	—
T-5	0.0219	40°	—
T-6	0.0228	50°	—
T-7	0.0285	1.00	0.50
T-8	0.0282	1.25	1.00
T-9	0.0287	1.50	1.50
T-10	0.0290	1.75	2.00
T-11	0.0288	2.00	2.50
T-12	0.0282	2.25	3.00
T-13	0.0283	2.50	3.50

NOSEPIECE — (0.87" radius x 30° cone)

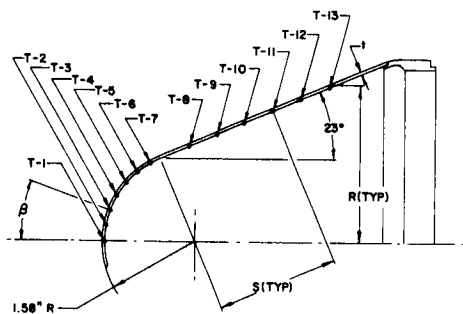
Figure IV-20

Thermocouple Locations - Intermediate Radius Nosepieces



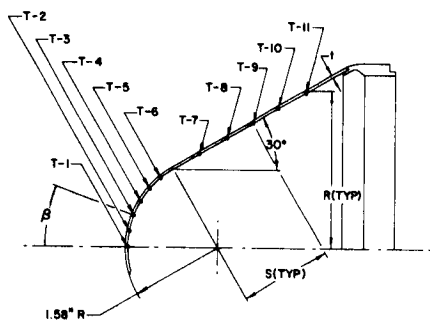
THERMOCOUPLE NO.	MATERIAL THICKNESS (t)	ANGLE ( $\beta$ ) or RADIUS (R)	S
T-1	0.0292	0°	—
T-2	0.0292	10°	—
T-3	0.0291	20°	—
T-4	0.0293	30°	—
T-5	0.0309	40°	—
T-6	0.0305	50°	—
T-7	0.0310	60°	—
T-8	0.0312	70°	—
T-9	0.0312	1.59	0.25
T-10	0.0305	1.66	0.50
T-11	0.0296	1.80	1.00
T-12	0.0297	1.93	1.50
T-13	0.0298	2.07	2.00
T-14	0.0300	2.21	2.50
T-15	0.0294	2.35	3.00
T-16	0.0287	2.48	3.50
T-17	0.0315	2.62	4.00
T-18	0.0317	2.76	4.50

NOSEPIECE -(1.58" radius x 16° cone)



THERMOCOUPLE NO.	MATERIAL THICKNESS (t)	ANGLE ( $\beta$ ) or RADIUS (R)	S
T-1	0.0308	0°	—
T-2	0.0302	10°	—
T-3	0.0293	20°	—
T-4	0.0290	30°	—
T-5	0.0295	40°	—
T-6	0.0300	50°	—
T-7	0.0305	60°	—
T-8	0.0288	1.85	0.50
T-9	0.0289	1.85	1.00
T-10	0.0290	2.04	1.50
T-11	0.0290	2.24	2.00
T-12	0.0292	2.43	2.50
T-13	0.0293	2.63	3.00

NOSEPIECE -(1.58" radius x 23° cone)



THERMOCOUPLE NO.	MATERIAL THICKNESS (t)	ANGLE ( $\beta$ ) or RADIUS (R)	S
T-1	0.0300	0°	—
T-2	0.0295	10°	—
T-3	0.0294	20°	—
T-4	0.0292	30°	—
T-5	0.0300	40°	—
T-6	0.0305	50°	—
T-7	0.0286	1.62	0.50
T-8	0.0290	1.87	1.00
T-9	0.0288	2.12	1.50
T-10	0.0287	2.37	2.00
T-11	0.0282	2.62	2.50

NOSEPIECE -(1.58" radius x 30° cone)

Figure IV-21

Thermocouple Locations - Large Radius Nosepieces

## V. RESULTS AND DISCUSSION

### A. TEST PROCEDURE

The objectives for this scale model centerbody diffuser program were to obtain aerodynamic and heat transfer performance data for selected centerbody diffuser configurations. Three different nose radii (0.395-in., 0.87-in., and 1.58-in.) and three different nose cone angles ( $16^\circ$ ,  $23^\circ$ , and  $30^\circ$ ) were selected to be tested. Combining these nose radii and nose cone angles gives nine different configurations.

The working fluid used in all the tests was hot gaseous nitrogen. The nitrogen was preheated to approximately  $1350^\circ\text{R}$  by a stored energy heater and injected into the subscale 40:1 contoured NERVA II nozzle at the desired chamber pressure. The chamber pressure and nozzle throat size governed the flow rate.

Aerodynamic performance for the centerbody diffusers was evaluated by measuring the chamber conditions (pressure and temperature), nozzle exit pressure, cell pressure, and selected pressures along the inside of the duct wall.

Maximum aerodynamic heat transfer occurs in the vicinity of the stagnation region; therefore, heat transfer measurements using the transient "thin wall technique" were made on each centerbody nosecone and the stagnation portion of the front and rear centerbody mounting struts. Each centerbody diffuser configuration was tested for heat transfer at a nozzle chamber pressure of approximately 40 atmospheres. Burst diaphragms were used just upstream of the nozzle to obtain steady-state conditions in the shortest possible time. Both the flow-rate and gas total temperature were held as nearly constant as possible throughout the test runs.

During a given test, only a limited number of experimental measurements could be sensed and recorded; therefore, testing was divided into two groups - Group I being pressure profile tests, i.e., fluid flow performance; and Group II being heat transfer tests.

## B. EXPERIMENTAL HEAT TRANSFER COEFFICIENTS

### 1. Method

The transient "thin-wall" technique was chosen to obtain the local heating rates and heat transfer convection coefficients at the expected hot spots in the centerbody diffuser system. K. M. Nicoll\* of Princeton University has used this method and in regard to its use he states:

"The primary advantages of this method are

- a. There is virtually no limit to the number of measuring points on a particular model, and each point gives a time "local" measurement.
- b. Models are simple to construct, and instrumentation is not complicated.
- c. The temperature distribution on the model at any time is a continuous function of position. (cf. the "insulate" technique)

The disadvantages of the method are that one must differentiate experimental data, and that data reduction is rather tedious and involved."

In order for the transient "thin wall" technique to be valid, the thermal resistance of the thin wall must be small (10% or less) when compared to the thermal resistance of the thermal boundary layer. This ensures that the thermal gradient normal to the thin wall is negligible during the heating transient. This condition was fulfilled in this test program by fabricating the sections to be tested for heat transfer (centerbody nose and portions of the mounting struts and aft section) of thin (20 to 30 thousandths of an inch thick) 304 stainless steel.

---

\* K. M. NICOLL, The Use of the Transient "Thin-Wall" Technique in Measuring Heat Rates in Hypersonic Separated Flows, Princeton University, Report 628, July 1962

Using the transient "thin wall" technique, the local heat flux ( $q$ ) at a point  $n$  is given by the expression

$$q = \rho c t \frac{dT_n}{d\beta} \quad (\text{Btu/in.}^2\text{sec}) \quad (1)$$

where  $\rho$ ,  $c$ , and  $t$  are, respectively, the thin wall material density, specific heat, and thickness, and the  $dT_n/d\beta$  is the instantaneous change of wall temperature  $T_n$  with respect to time  $\beta$ . The variation of the specific heat  $c$  with temperature was taken into account by assuming a linear change with respect to the temperature. The local heat transfer convection coefficient  $h$  is then determined from the expression

$$h = \frac{q}{(T_R - T_n)} \left( \frac{\text{Btu}}{\text{in.}^2\text{-sec } ^\circ\text{R}} \right) \quad (2)$$

where  $(T_R - T_n)$  is the difference between the local gas recovery temperature and the local wall temperature.

In the present program, heat transfer coefficients were obtained on the centerbody nose piece (see Figures IV-5 through IV-10), on the centerbody mounting struts, and on the aft section of the centerbody along the duct axis.

The centerbody nose pieces are blunt cones - the blunt part consisting of a spherical segment. A numerical method was devised and programmed on a 7040 IBM computer to correct for conduction effects in the nose piece spherical segment and conical sections. This method accounted for thermal conductivity changes in the wall material. This method is presented in Appendix A.

Heat transfer coefficients were measured at two locations on a front mounting strut and two locations on a rear mounting strut (see Figure IV-4). Where heat transfer measurements were to be made, the struts were fabricated from 0.030 in. thick 304 stainless steel sheet.

A single heat transfer measurement was made at the aft section.

## 2. Test Results

### a. Centerbody Nose Cone

Experimental heat transfer coefficients for each of the nine centerbody nose cones are presented in Figures V-1 through V-9 as a function of position on the nose piece. Each of these coefficients has been normalized\* to design scale model chamber conditions of 550 psia and 1400°R. The experimentally determined heat transfer coefficients at the stagnation point are also presented in Figure V-10 as a function of the nose cone radius.

The experimentally determined heat transfer coefficients in the stagnation region are much lower than those predicted by theory. This fact will be discussed in Section V, D, below. Comparison of Experimental and Analytical Results.

### b. Centerbody Mounting Struts

Experimental heat transfer coefficients measured at the stagnation point on the front and rear mount struts are presented in Table V-1. These coefficients have been normalized to the scale model design chamber conditions of 1400°R and 550 psia assuming laminar flow at the stagnation point.

### c. Centerbody Aft Section

An average experimental heat transfer coefficient of  $1.54 \times 10^{-4}$  (Btu/in.<sup>2</sup>-sec-°R) was measured at the aft section of the centerbody.

### d. Determination of Centerbody Nose Cone Heat Transfer Coefficient Using Hy-Cal Asymptotic Calorimeter

During one run, the heat transfer coefficient was also measured using a calorimeter. A Hy-Cal asymptotic type calorimeter was positioned at the  $\theta = 30^\circ$  location in the spherical segment of the nose cone for which

\* Normalized assuming laminar flow at the stagnation point and  $\theta = 10^\circ$ ; all other positions are normalized assuming turbulent flow.

NOTES.

1. NOSECONE RADIUS  $R = 0.395"$ , CONE HALF ANGLE  $\alpha = 16^\circ$

2. RUN NO. 13.

CHAMBER PRESSURE VARIED FROM 561 TO 579 psia.

CHAMBER TEMPERATURE VARIED FROM 1393 TO 1422 °R

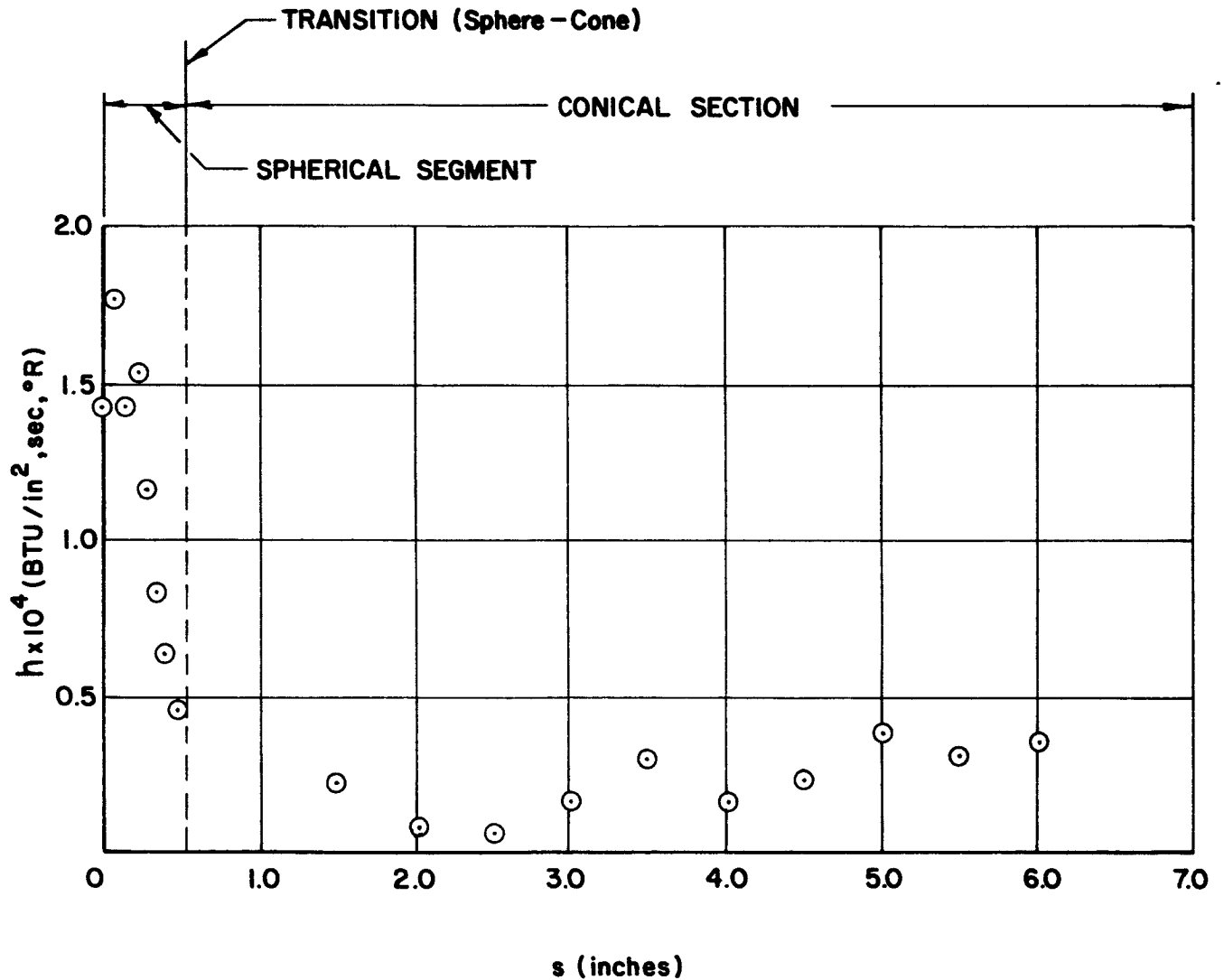


Figure V-1

Experimental Heat Transfer Coefficient ( $h$ )  
as a Function of Developed Contour Length ( $s$ ),

Run No. 13

NOTES.

1. NOSECONE RADIUS  $R = 0.395$ ", CONE HALF ANGLE  $\alpha = 23^\circ$

2. RUN NO. 15.

CHAMBER PRESSURE VARIED FROM 549 TO 565 psia

CHAMBER TEMPERATURE VARIED FROM 1315 TO 1342 °R

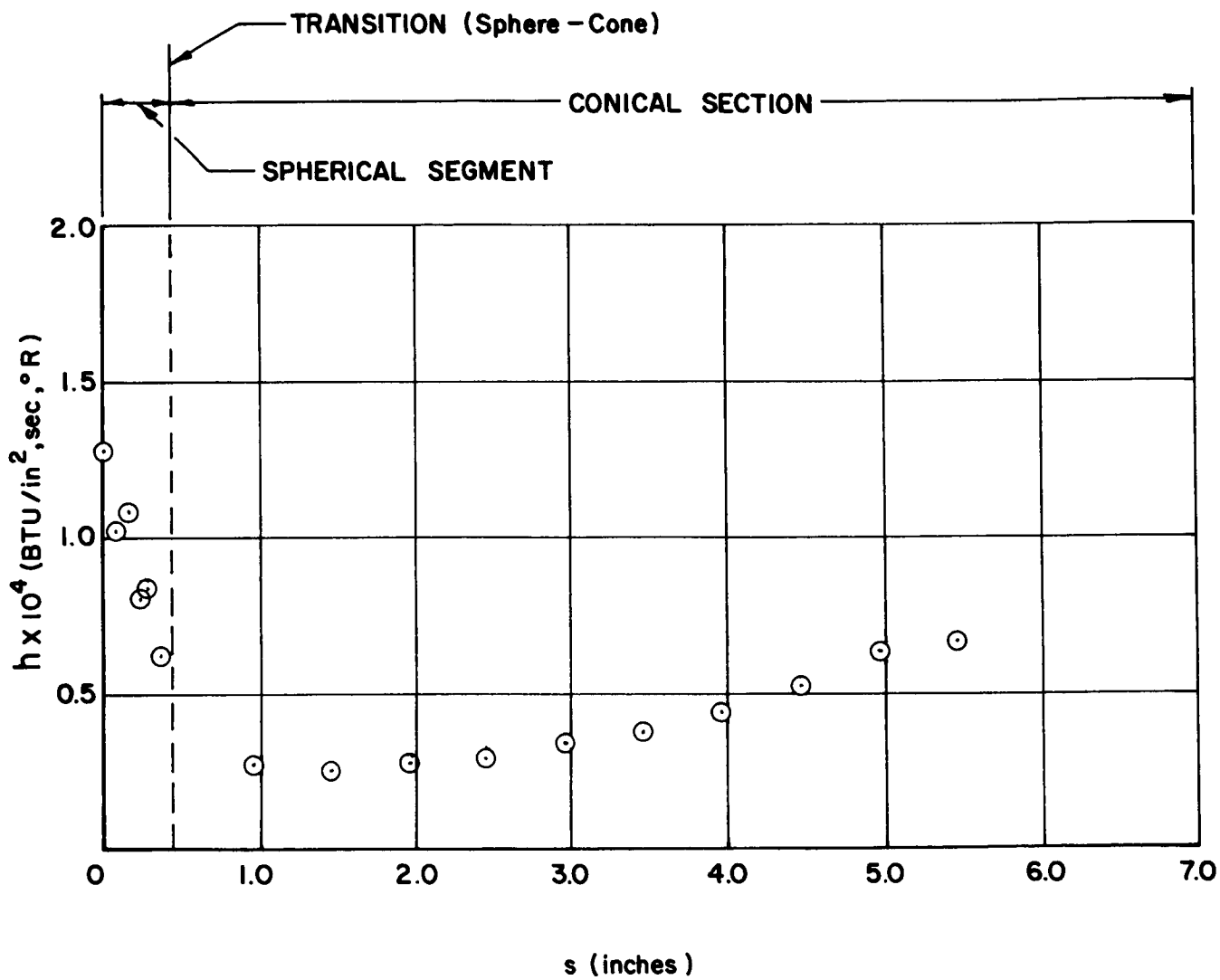


Figure V-2

Experimental Heat Transfer Coefficient ( $h$ )  
as a Function of Developed Contour Length ( $s$ ),

Run No. 15

NOTES.

1. NOSECONE RADIUS  $R = 0.395''$ , CONE HALF ANGLE  $\alpha = 30^\circ$

2. RUN NO. 17.

CHAMBER PRESSURE VARIED FROM 543 TO 567 psia

CHAMBER TEMPERATURE VARIED FROM 1266 TO 1314 °R

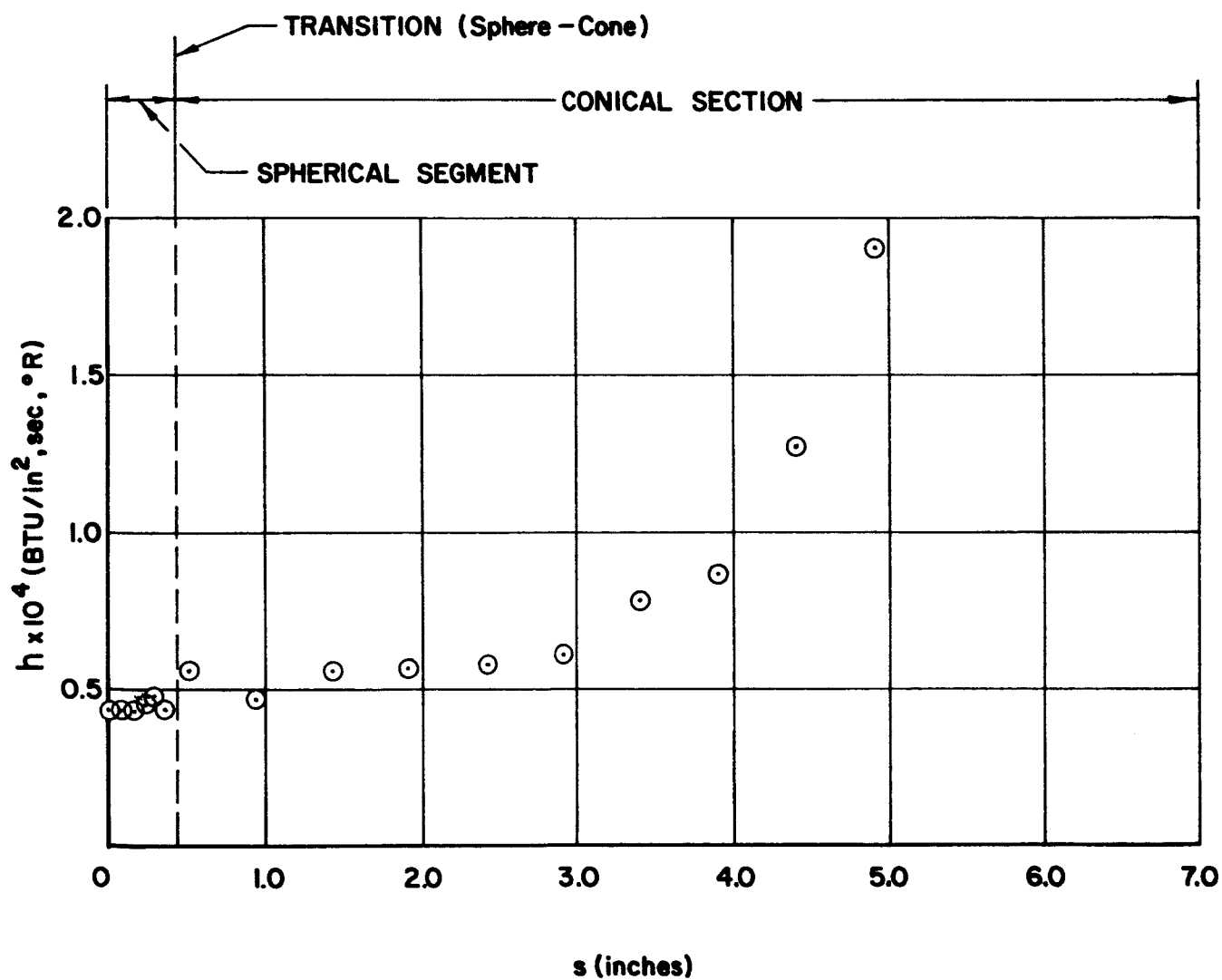


Figure V-3

Experimental Heat Transfer Coefficient ( $h$ )  
as a Function of Developed Contour Length ( $s$ ),

Run No. 17

V-7

NOTES.

1. NOSECONE RADIUS  $R = 0.87$  ", CONE HALF ANGLE  $\alpha = 16^\circ$

2. RUN NO. 23.

CHAMBER PRESSURE VARIED FROM 553 TO 573 psia.

CHAMBER TEMPERATURE VARIED FROM 1397 TO 1436 °R

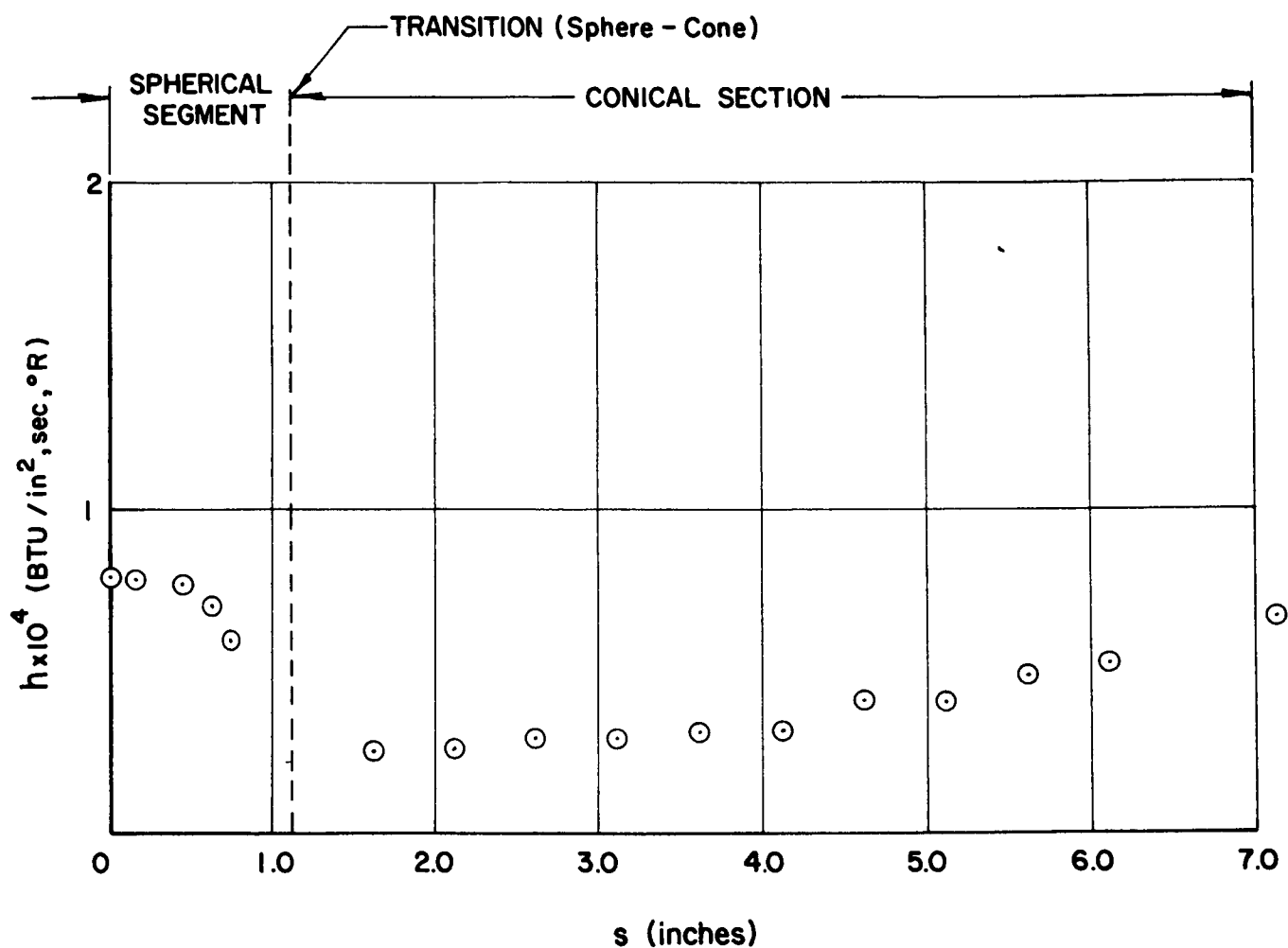


Figure V-4

Experimental Heat Transfer Coefficient ( $h$ )  
as a Function of Developed Contour Length ( $s$ ),

Run No. 23

NOTES.

1. NOSECONE RADIUS  $R = 0.87''$ , CONE HALF ANGLE  $\alpha = 23^\circ$

2. RUN NO. 24.

CHAMBER PRESSURE VARIED FROM 549 TO 577 psia

CHAMBER TEMPERATURE VARIED FROM 1357 TO 1413° R

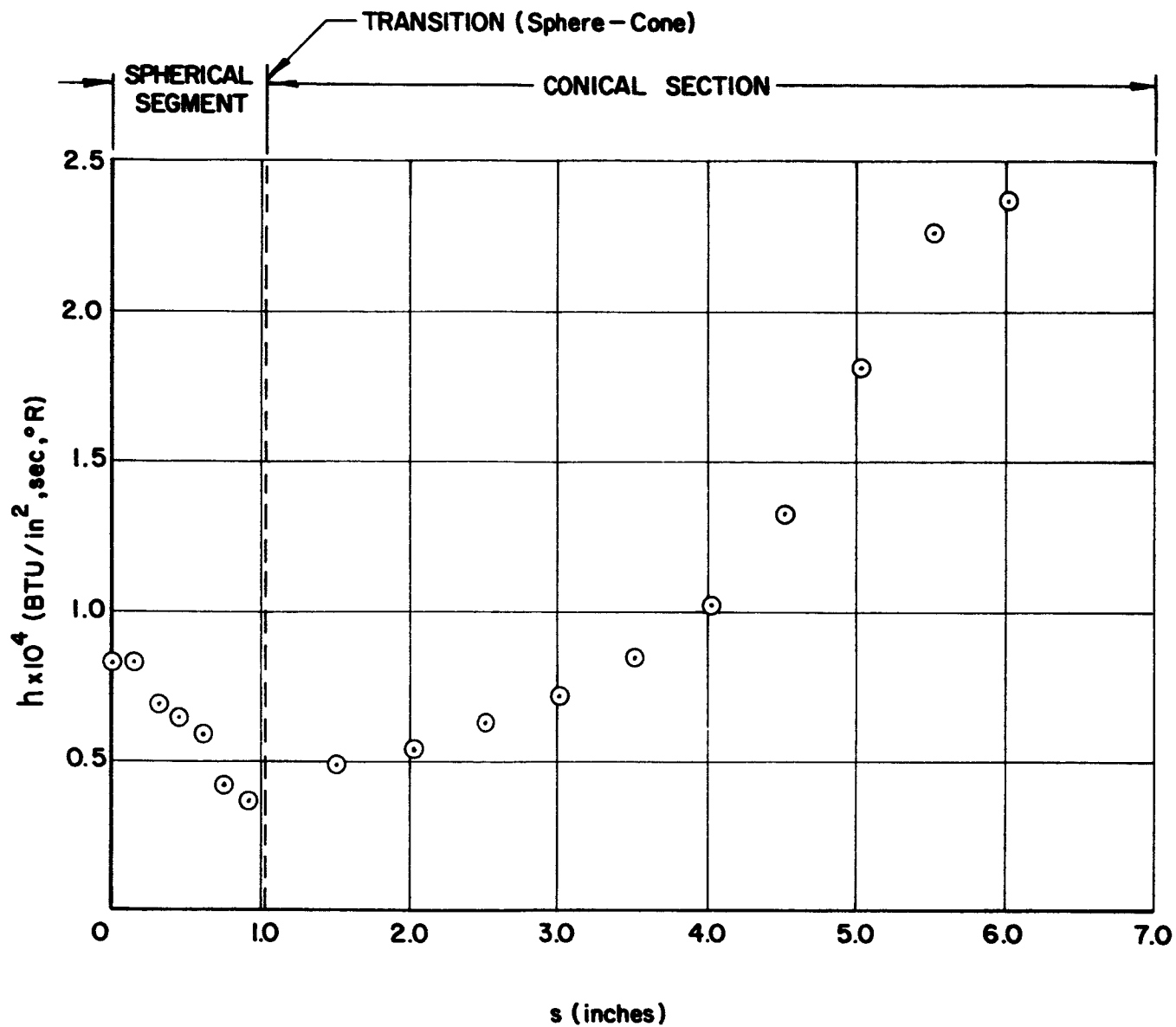


Figure V-5

Experimental Heat Transfer Coefficient (h)  
as a Function of Developed Contour Length (s),

Run.No. 24

NOTES.

1. NOSECONE RADIUS  $R = 0.87''$  , CONE HALF ANGLE  $\alpha = 30^\circ$

2. RUN NO. 22

CHAMBER PRESSURE VARIED FROM 499 TO 551 psia

CHAMBER TEMPERATURE VARIED FROM 1332 TO 1373° R

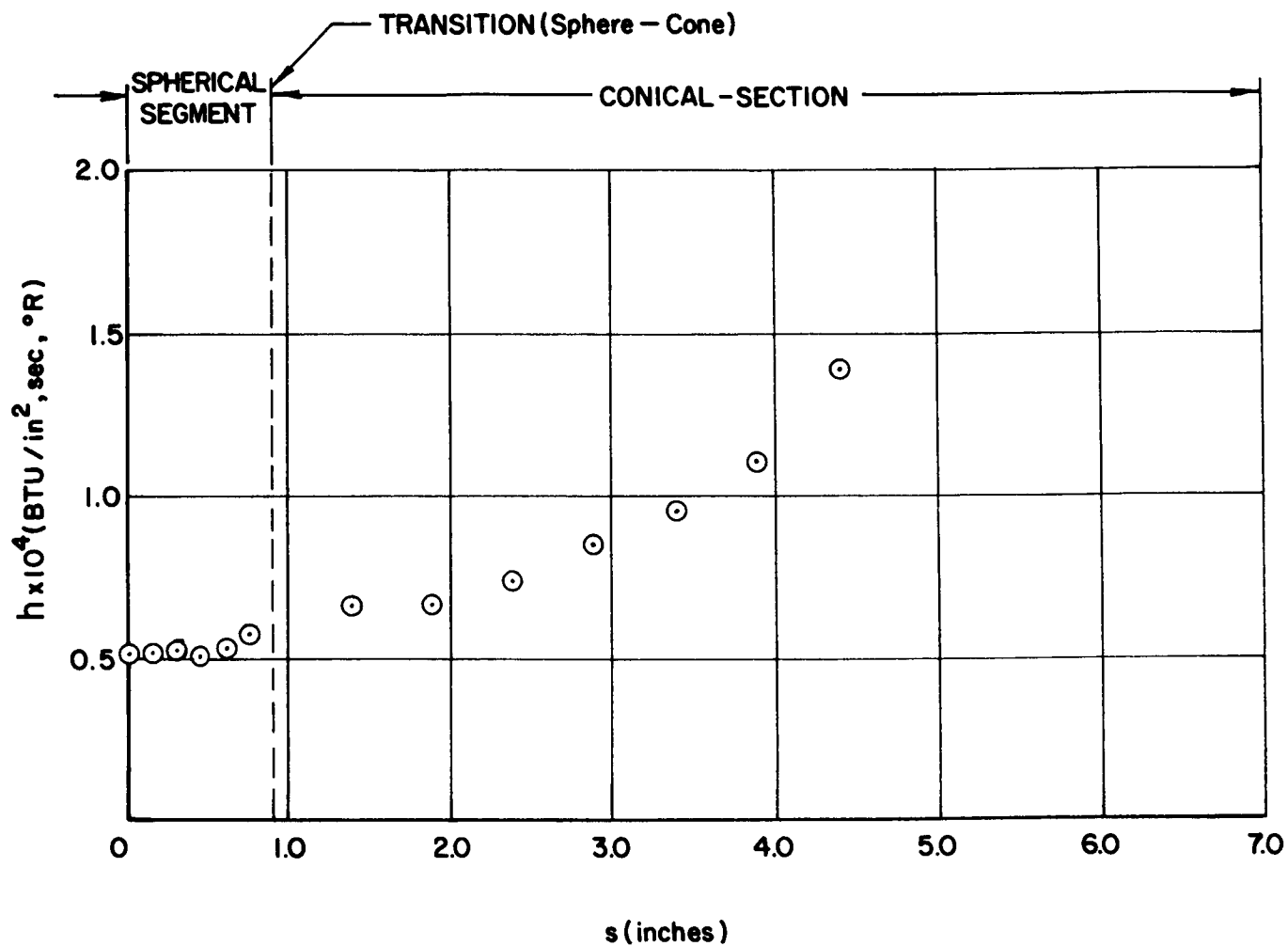


Figure V-6

Experimental Heat Transfer Coefficient ( $h$ )  
as a Function of Developed Contour Length ( $s$ ),

Run No. 22

NOTES.

1. NOSECONE RADIUS  $R = 1.58''$  , CONE HALF ANGLE  $\alpha = 16^\circ$

2. RUN NO. 21.

CHAMBER PRESSURE VARIED FROM 543 TO 567 psia

CHAMBER TEMPERATURE VARIED FROM 1321 TO 1380 °R

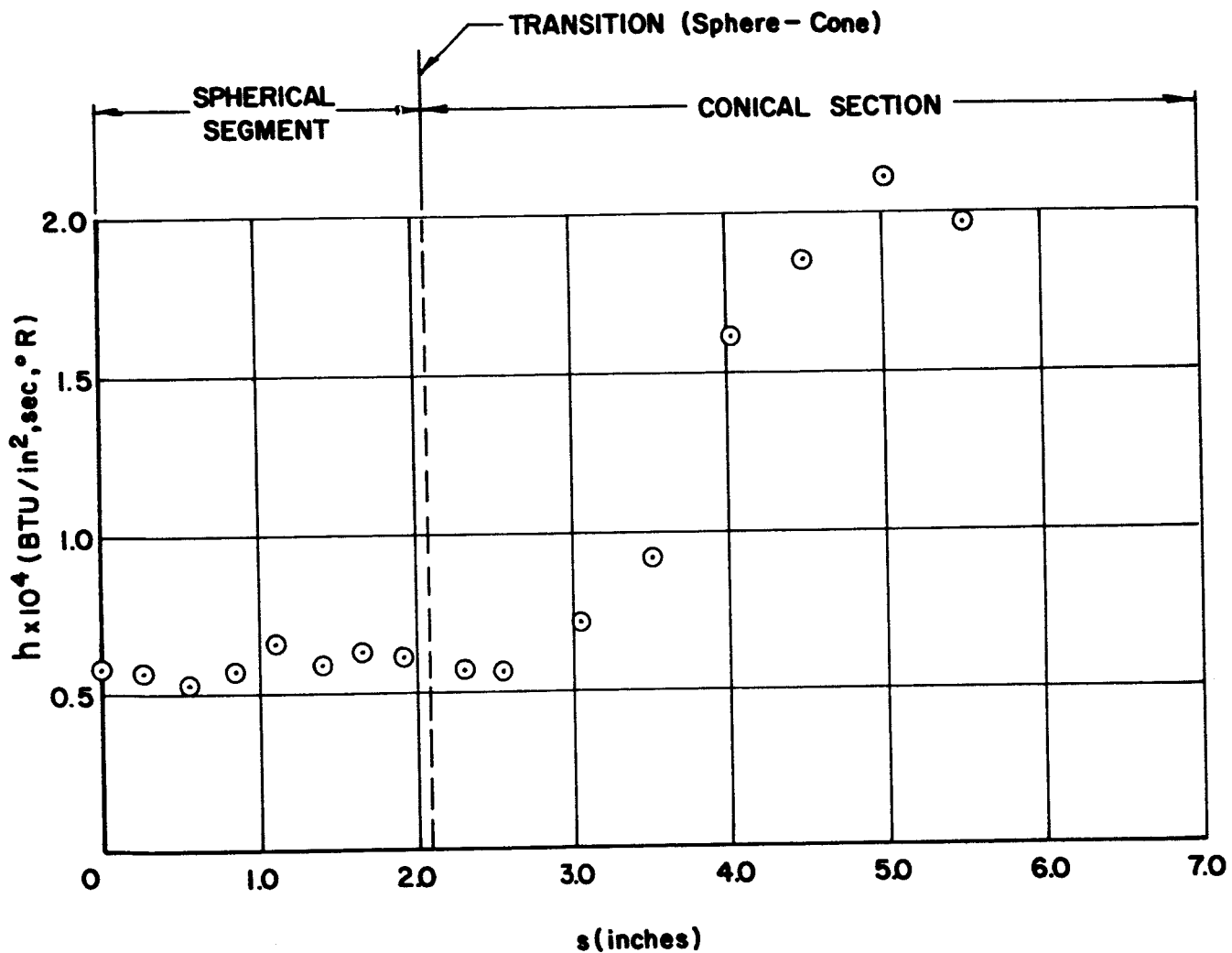


Figure V-7

Experimental Heat Transfer Coefficient ( $h$ )  
as a Function of Developed Contour Length ( $s$ ),

Run No. 21

V-11

NOTES.

1. NOSECONE RADIUS  $R = 1.58''$  , CONE HALF ANGLE  $\alpha = 23^\circ$

2. RUN NO. 20.

CHAMBER PRESSURE VARIED FROM 547 TO 573 psia

CHAMBER TEMPERATURE VARIED FROM 1304 TO 1364 °R

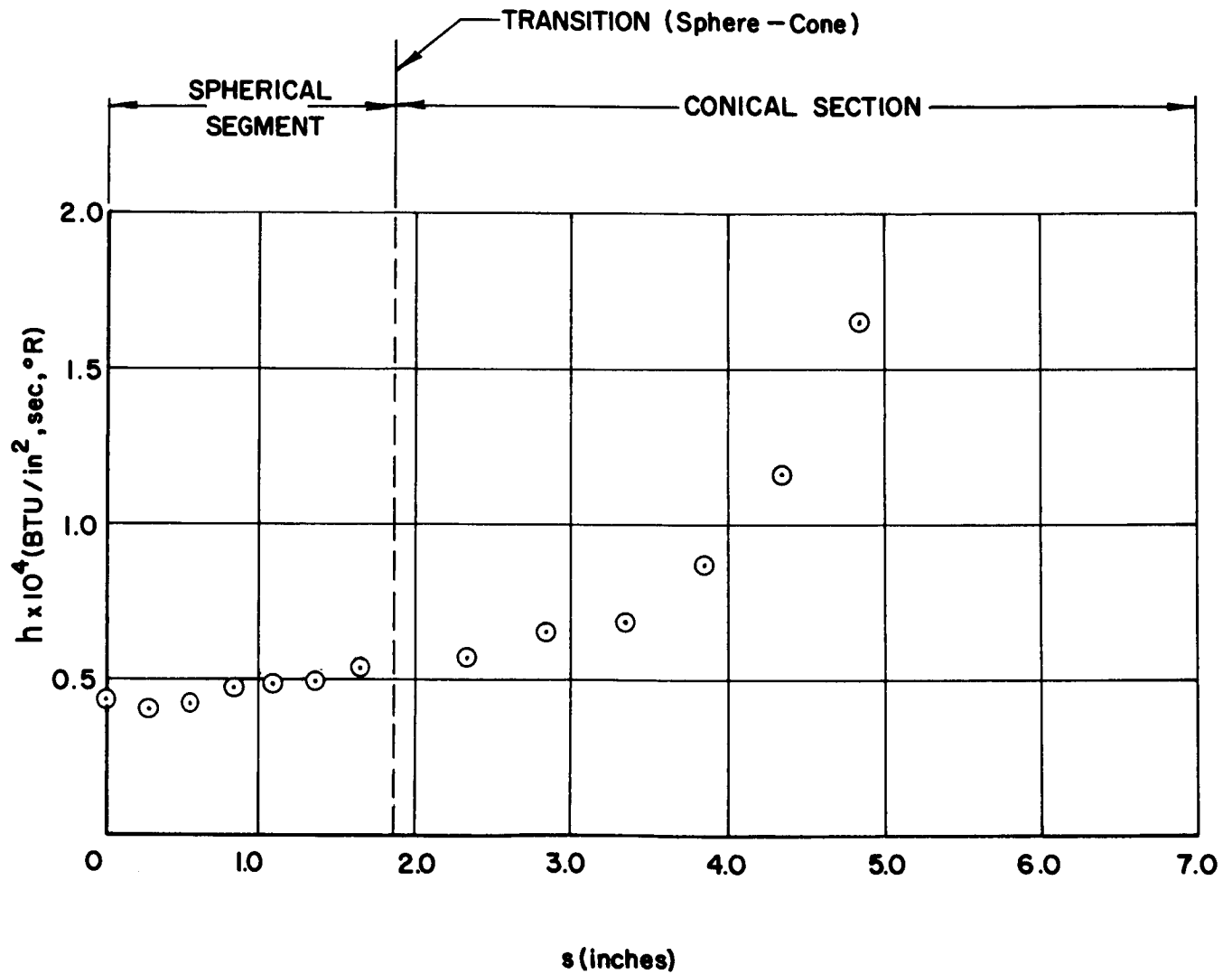


Figure V-8

Experimental Heat Transfer Coefficient ( $h$ )  
as a function of Developed Contour Length ( $s$ ),

Run No. 20

V-12

NOTES.

1. NOSECONE RADIUS  $R = 1.58''$ , CONE HALF ANGLE  $\alpha = 30^\circ$

2. RUN NO. 19.

CHAMBER PRESSURE VARIED FROM 565 TO 577 psia

CHAMBER TEMPERATURE VARIED FROM 1319 TO 1355 °R

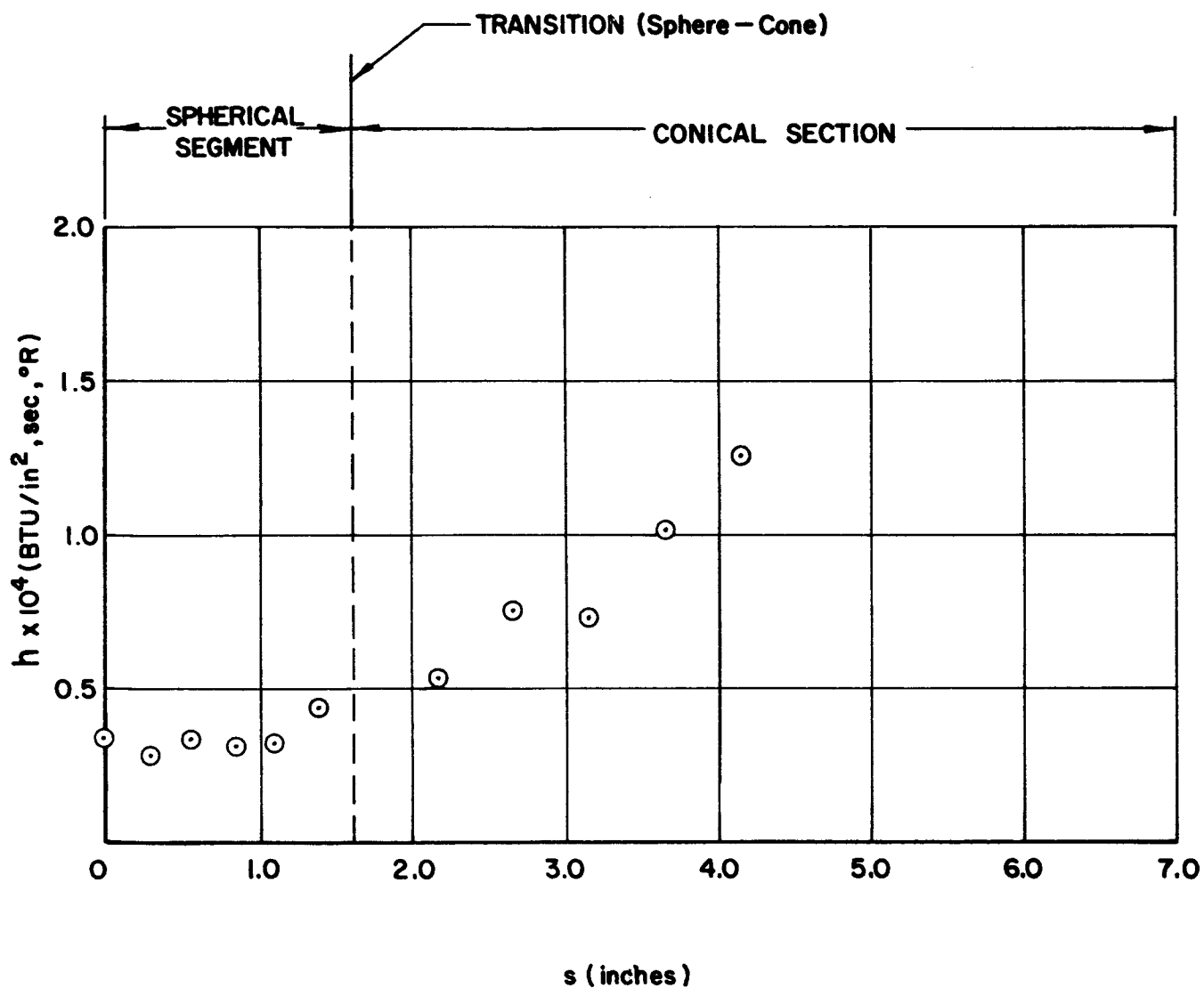


Figure V-9

Experimental Heat Transfer Coefficient ( $h$ )  
as a Function of Developed Contour Length ( $s$ ),

Run No. 19

V-13

# NOTES.

## 1. COEFFICIENTS ADJUSTED TO NORMAL CHAMBER CONDITIONS

$P_c = 550 \text{ psia}$  ,  $T_c = 1400^\circ\text{R}$

NOSE CONE ANGLE	SYMBOL
$30^\circ$	$\odot$
$23^\circ$	$\square$
$16^\circ$	$\triangle$

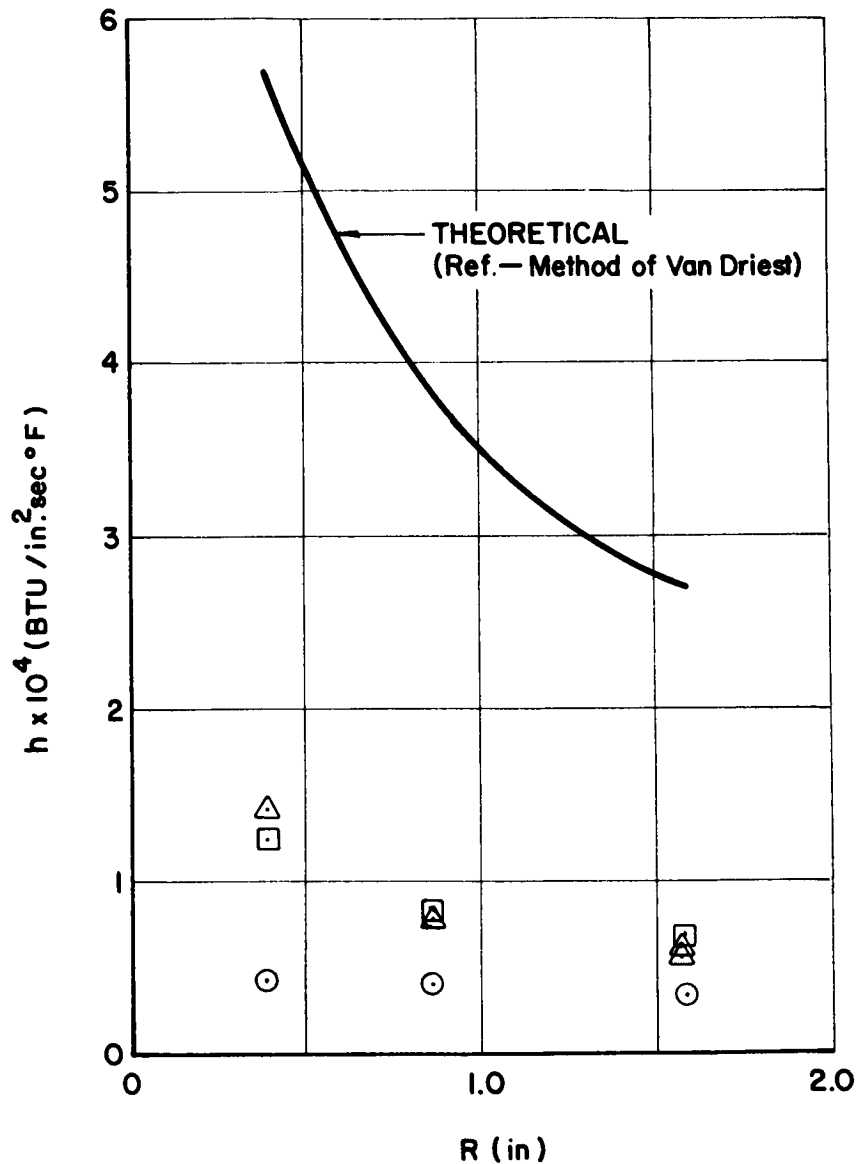


Figure V-10

Experimental Centerbody Stagnation Point Heat Transfer Coefficients  
as a Function of Nosecone Radius

TABLE V-1  
STAGNATION POINT HEAT TRANSFER COEFFICIENTS  
ON CENTERBODY MOUNTING STRUTS

<u>LOCATION</u>	<u>RUN NO.</u>	<u><math>h \times 10^4</math> (Btu/in<sup>2</sup>-sec-°R)</u>
T <sub>fi</sub>	20	14.9
T <sub>fo</sub>	20	12.4
T <sub>ri</sub>	3	5.6
T <sub>ro</sub>	20	10.6

$R = 1.58$ -in. and  $\alpha = 30^\circ$  during the test D-285-LQ-19. During the early part of the test, a heat transfer coefficient equal to  $7.8 \times 10^{-5}$  (Btu/in.<sup>2</sup>-sec-°R) was measured using the calorimeter, and a corresponding heat transfer coefficient equal to approximately  $3.0 \times 10^{-5}$  (Btu/in.<sup>2</sup>-sec-°R) was measured using the transient thin wall technique.

## C. ANALYTICAL HEAT TRANSFER COEFFICIENTS

### 1. Introduction

At the beginning of the Contract Year, a literature survey was made, dealing with diffusers in general (Reference 1). Part IV of this compilation lists a number of papers referring to heat transfer on a body of revolution. These papers, plus some additional references, were studied to determine their applicability to a centerbody diffuser and to find out which theories would be most reliable to predict heat transfer rates to a centerbody in a supersonic gas stream.

For various reasons, the works of many authors, including Sibulkin, Mark, Romig, and Cohen & Reshotko were eliminated, leaving those of Lester Lees, Fay & Riddell and Van Driest as recommended methods to predict heating rates. (References 1-10).

### 2. Purpose of Analytical Heat Transfer Studies

The main reasons for performing analytical heat flux studies can be summarized as follows:

a. Obtain a preliminary idea about the range of full scale heat flows and judge whether they are low enough to allow a practical full scale design of a centerbody type diffuser.

b. Obtain an approximate range of heat transfer rates for proper design and instrumentation techniques for subscale model tests.

c. Obtain a valid basis to compare predicted heating values to those secured from the experimental tests and thus learn more about the complexity and intricacies of the problem.

d. Increase the confidence level in subscale and full scale heat transfer predictions.

### 3. Scope of Work

The theoretical work encompasses a series of individual studies over various regions of the centerbody and its support. In accordance with the regions analyzed, the following studies were made:

- a. Forward stagnation point heat transfer.
- b. Effect of wall temperature and transport properties on forward stagnation point heat transfer.
- c. Laminar heat transfer rates of the spherical center body surface with emphasis on the region from  $0^\circ$  to  $45^\circ$ .
- d. Turbulent heat transfer rates of the spherical center body surface (same region as under c, above).
- e. Heat transfer rates along the conical section of the center body.
- f. Approximation of heating rates at transition point of sphere to cone.
- g. Composite heating rates.
- h. Heat transfer rates to centerbody mounting struts.

#### 4. Discussion

##### a. Forward Stagnation Point Heat Transfer

A preliminary study consisted in a test of methods and formulas suggested by various papers selected from a literature survey (Reference 1). The authors developed their method starting from some simple expression for the heat flux, i.e., the product of film coefficient and temperature difference between wall surface and outer edge of boundary layer, or the product of thermal conductivity and temperature gradient. By mathematical development they arrive at forms which are very similar to each other and of which the following equation is a typical example. (See Appendix B for the mathematical development.)

$$q = f(\rho \mu)^{0.5} \left( \frac{\partial u}{\partial x} \right)^{0.5} \Delta H$$

This expression contains four basic terms, or group of terms:

(1) The total enthalpy or enthalpy difference; sometimes a temperature difference times an average specific heat, the latter being rather difficult to determine.

(2) The velocity gradient at the one-half power.

(3) The density-viscosity product at the one-half power. These transport properties are generally chosen for stagnation conditions outside the boundary layer.

(4) A dimensionless heat transfer parameter. The difference between the various methods stems mainly from the way these term-groups are assembled and evaluated.

Sibulkin's method (Reference 2) is practically identical with that of Van Driest. Mark (Reference 3) does not relate the heat transfer parameter to the transport properties. Romig (Reference 4) evaluates transport properties at a reference enthalpy equal to the average of that between wall and boundary edge.

Cohen & Reshotko (Reference 5) use an erroneous velocity gradient. Lees (Reference 6) uses for the enthalpy-term the value of  $\frac{U_{\infty}^2}{2 g J}$  which results in a heat flux to a cold wall; for large temperature differences the deviation by his procedure is negligible.

Van Driest and Fay & Riddell (Reference 7, 8, 9 and 10) suggest almost the same formula, except that the "transport-property term" for Fay & Riddell is the product  $(\rho \mu)_w^{0.1} \cdot (\rho \mu)_{es}^{0.4}$  as compared to  $(\rho \mu)_{es}^{0.5}$  for Van Driest.

The methods were checked with a numerical example for a hydrogen-gas flow and chamber conditions of 800 psia and 5000°R. The expanded gases were assumed to have reached  $M = 5$  just ahead of the bow shock caused by the center-body. For three of the methods, the following laminar heating rates were computed for the forward stagnation point:

Lester Lees:	$q_o = \frac{397}{\sqrt{R}}$
Van Driest:	$q_o = \frac{423}{\sqrt{R}}$
Fay & Riddell:	$q_o = \frac{426}{\sqrt{R}}$

While these figures are within 7% of each other, the results of the remaining methods gave much higher deviations up to a maximum of 30% for the worst case.

The above values correspond to laminar flow conditions as this is the only possible case at the forward stagnation point. The values do not reflect the effects of gas dissociation, which for hydrogen gas become noticeable at temperatures above 4000°R.

The purpose of this analysis was achieved by reducing the methods under consideration to those that are the most applicable and giving closest results.

b. Effect of Wall Temperature and Transport Properties on Forward Stagnation Point Heat Transfer

It has been shown that three methods to compute heating rates and film coefficient (Van Driest, Fay & Riddell and Lester Lees) would lead to almost identical results. However, this is correct only when the ratio of wall temperature to stagnation temperature is much smaller than unity. A study was made to evaluate how the heat transfer coefficient would be influenced by changing transport properties and a small total temperature difference of perhaps 400° to 800°R, a range most likely to be witnessed during the small scale test with nitrogen gas.

As a matter of clarification, the formulas corresponding to the above methods are shown, first, in the explicit form for  $(q_w)_o$ , the flux at the forward stagnation point, and second, solved for the film coefficient (h) by lumping into a constant the terms which do not change with rising wall temperature during the tests.

Lester Lees:

$$(q_w)_o = \frac{0.707}{P_r^{0.666}} G (\rho \mu)_{es}^{0.5} \frac{U_\infty^{0.5}}{R^{0.5}} \cdot \frac{U_\infty^2}{2 g J} \quad (4)$$

$$\frac{(q_w)_o}{T_R - t_w} = h \frac{\text{const.}}{T_R - t_w} \quad (4a)$$

Fay & Riddell:

$$(q_w)_o = \frac{0.763}{P_r^{0.6}} \left( \frac{\partial u}{\partial x} \right)^{0.5} (\rho \mu)_{es}^{0.4} (\rho \mu)_w^{0.1} \Delta H \quad (5)$$

$$\frac{(q_w)_o}{T_R - t_w} = h = \text{const.} (\rho \mu)_w^{0.1} \quad (5a)$$

Van Driest:

$$(q_w)_o = f \left( \frac{\partial u}{\partial x} \right)^{0.5} (\rho \mu)_{es}^{0.5} \Delta H \quad (6)$$

$$\frac{(q_w)_o}{T_R - t_w} = h = \text{const.} \quad (6a)$$

For the purpose of this study, in relations (5a) and (6a) the enthalpy difference has been replaced by an equivalent term, the product of total temperature drop and an average specific heat.

In the small scale tests, nitrogen with 1400°R and 550 psia is used as supply gas. During the tests, the wall temperature will rise. The following Table gives the variation of the variable terms for a series of different wall temperatures.

1	2	3	4	5	6
$t_w$ °R	$p_w$	$10^6 \times \mu_w$	$\left(\frac{p \mu}{10^6}\right)_w$	$\left(\frac{p \mu}{10^6}\right)_w^{0.1}$	$\frac{1}{T_R - t_w}$
600	0.1475	13.0	1.917	0.2680	0.00125
800	0.1108	15.9	1.76	0.2552	0.00167
1000	0.0886	18.6	1.648	0.2633	0.00250
1400	0.0737	20.9	1.54	0.2620	0.00500
				Fay & Riddell	Lester Lees

As shown in Column 5, Fay & Riddell give variations of 2.5% while those from Lester Lees' method (Column 6) amount to several hundred percent. Thus, the latter method is not recommended for cases with small temperature differences.

#### c. Laminar Heat Transfer Rates Along the Spherical Centerbody Surface

This analysis is limited to a region on the spherical centerbody tip from the forward stagnation point to a point located 45° away from it. Computations were made for a number of locations 5° apart; they were based upon a supply of gaseous nitrogen with a chamber pressure of 550 psia and 1400°R.

In accordance with Sections V -C-4 and V -C-4-b, the method of Van Driest (References 9 and 10) was finally chosen, because a considerable amount of his work was published and thus readily available, particularly regarding the region away from the forward stagnation point. Van Driest's procedure was refined by substituting Newtonian pressure distribution by that of Van Dyke (Reference 11).

The basic formula for the heat flux is:

$$(q_w)_x = f_{LX} (\rho \mu)_x^{0.5} \left( \frac{\partial u}{\partial x} \right)_x^{0.5} \Delta H_x \quad (7)$$

where the suffix x denotes locations at an arc distance X from the forward stagnation point.

The  $q_w$  - values are computed with four major assumptions:

- (1) Mach 5 is reached just ahead of the bow shock at the centerbody.
- (2) A constant wall temperature of 800°R is used in the calculation of the enthalpy difference.
- (3) Constant specific heat and Prandtl Number.
- (4) Hypothetical case of laminar flow conditions for the entire region under study.

Some of the terms in equation (7) change appreciably for locations away from the stagnation point.

The heat transfer parameter  $f_L$  is taken from a study by Stine and Wanlass (Reference 12).

$$f_L = \frac{1}{P_r} \left( \frac{Nu}{Re^{0.5}} \right) \quad (8)$$

The term in parenthesis is plotted in Figure 4b of Reference 12. In the summary of their Paper, Stine and Wanlass mention that this distribution of  $f_L$  is representative of all Mach numbers larger than 1.97 and of temperatures less than that of dissociation.

The transport properties for points outside the stagnation area are obtained from pressure distribution over the spherical surface and isentropic expansion from the stagnation point. The pressure distribution was obtained from numerical solutions worked out by Van Dyke (Reference 11). The use of this method is more realistic than the acceptance of a Newtonian pressure distribution.

The velocity gradient is based on the same pressure distribution. The velocities are obtained from isentropic tables in the form of dimensionless  $U/a^*$  - values. Resorting to a graphical procedure, the tangents to the velocity curve furnish the velocity gradients.

Enthalpy values are determined for a variable recovery temperature, changing with free stream temperature and Mach number at the edge of the boundary layer, which are both obtained from isentropic tables.

As long as laminar flow conditions prevail, the maximum heat flux occurs at the forward stagnation point with a gradually faster drop-off away from this point. At  $45^\circ$ , the heating rates would be approximately 64% of that of the center body tip. This drop-off is characteristic for all three nose configurations.

The convective laminar heat transfer coefficient is computed with a variable temperature difference (gas to wall) corresponding to a variable recovery temperature.

Figures V-11 and V-12 show heat flux and film coefficient for three different nose configurations as a function of distribution angle  $\theta$ .

The details of the computations are given in Appendix C in tabular form.

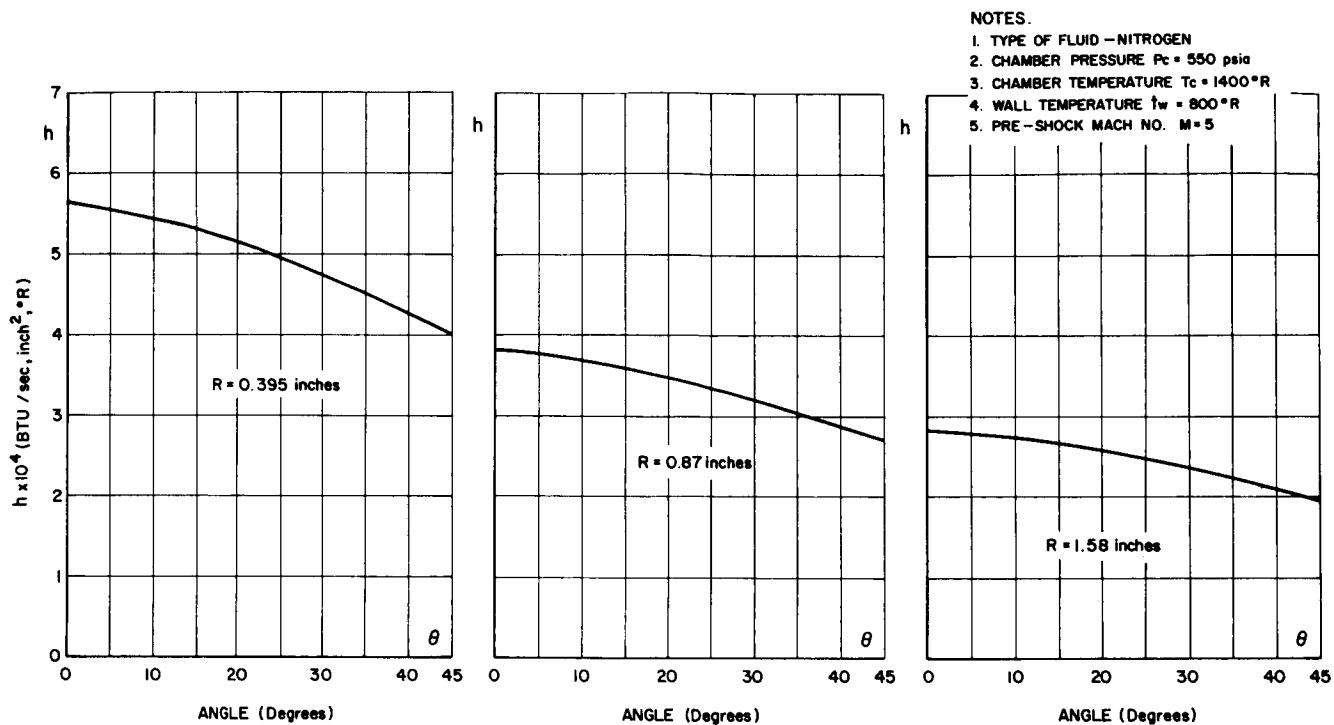


Figure V-11  
Laminar Heat Transfer Coefficient ( $h$ ) on a Spherical Centerbody versus  
Nose Radius and Location

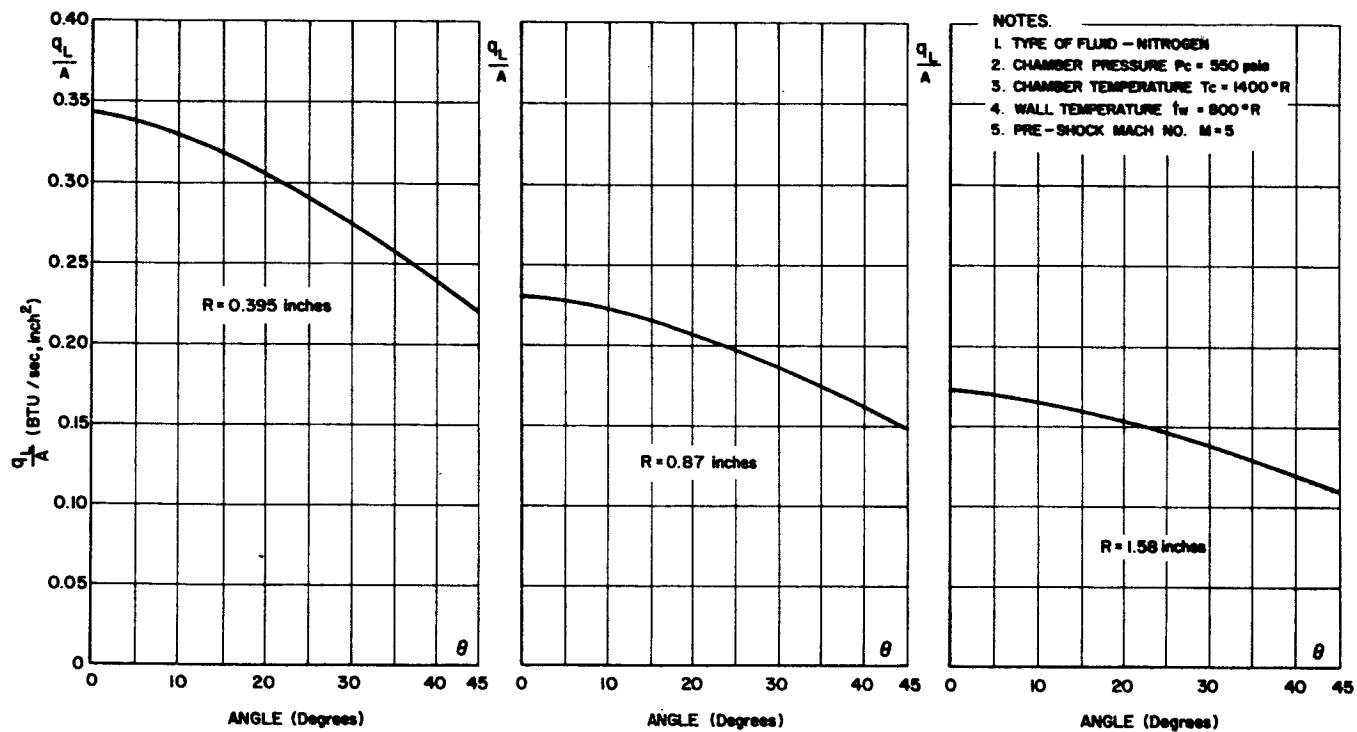


Figure V-12

Laminar Heating Rates ( $q_1$ ) on a Spherical Centerbody versus  
Nose Radius and Locations

d. Turbulent Heat Transfer Rates Along the Spherical Centerbody Surface

As in Section V-C-4-c, the region of concern for this study extends from forward stagnation point to a location  $45^\circ$  away. Calculations were performed for a number of points  $5^\circ$  apart.

Again Van Driest's procedure (Reference 9 and 10) was chosen. The equation used has the following form:

$$q_w = f_T (\rho^{0.8} \mu^{0.2}) \left( \frac{\partial u}{\partial x} \right)^{0.8} x^{0.6} \Delta H \quad (9)$$

The heat transfer parameter  $f_T$  diminishes with angle  $\theta$  and for  $90^\circ$  would assume the value for flow over a flat plate. Appendix C contains a simplified relation to calculate  $f_T$  - values.

The transport properties  $\rho$  and  $\mu$ , and the velocity gradient are evaluated as shown in Appendix C.

The enthalpy values are calculated for variable recovery temperatures, changing with Mach number and free stream temperature, both obtained from isentropic tables.

The computed  $q_w$  values are based upon an assumed Mach number of 5 just ahead of the bow shock, a wall temperature of  $800^\circ\text{R}$ , and constant Prandtl number and specific heat.

Convective heat transfer conditions are computed in accordance with a variable recovery temperature for turbulent flow conditions.

The turbulent heat transfer rate increases rapidly with the distance from the stagnation point. However, because of a gradual decrease of the transport properties (especially the density) with increasing velocities, the change of the heating rate approaches zero and then becomes negative. The heating

rate curves show a maximum at approximately  $41^\circ$  away from the stagnation point. All three nose configurations present the same heat flux pattern with smaller values for the larger nose diameter and vice versa.

Figures V-13 and V-14 illustrate this pattern for both the heat flux and the convective heat transfer coefficients as a function of distribution angle  $\theta$ .

All computations are shown in detail in Appendix D.

e. Laminar Heat Transfer Rates Along Conical Section of the Centerbody

The heat transfer rates to the surface of a cone frustum capped by a spherical tip are computed by a procedure suggested by Lester Lees in Chapter 3 (Case II) of Reference 6. It should be noted here that the heat transfer rate distribution is not quite the same as for a sharp-nosed cone. To illustrate the difference, Lester Lees gives the equations for both cases. In general, the heat flows to a frustum are larger for cone angles of  $30^\circ$  and above  $30^\circ$  than for a similar uncapped cone. For slender cones with angles of less than  $30^\circ$ , the opposite is true.

The relation for the cone frustum is given in a form referenced to the stagnation point heat transfer at the centerbody nose for laminar flow conditions:

$$\frac{(q_w)_s}{(q_w)_o} = \frac{A \alpha \cdot s'/R_o}{[B \alpha + (s'/R_o)^3]^{1/2}} \quad (10)$$

where the subscript  $s$  indicates a location on the cone measured by the contour distance  $s$  from the forward stagnation point on the spherical segment, or equivalent to a given distribution angle  $\theta$ . In equation (10), the distance  $s'$  is that from the virtual sharp-nosed cone tip. This distance is related to cone angle and distribution angle by the equation

$$s' = \frac{R_o}{\sin(\alpha + \theta)} \cdot \frac{\sin \theta}{\sin \alpha} = R_o [\cot \alpha + \cot (\theta + \alpha)] \quad (11)$$

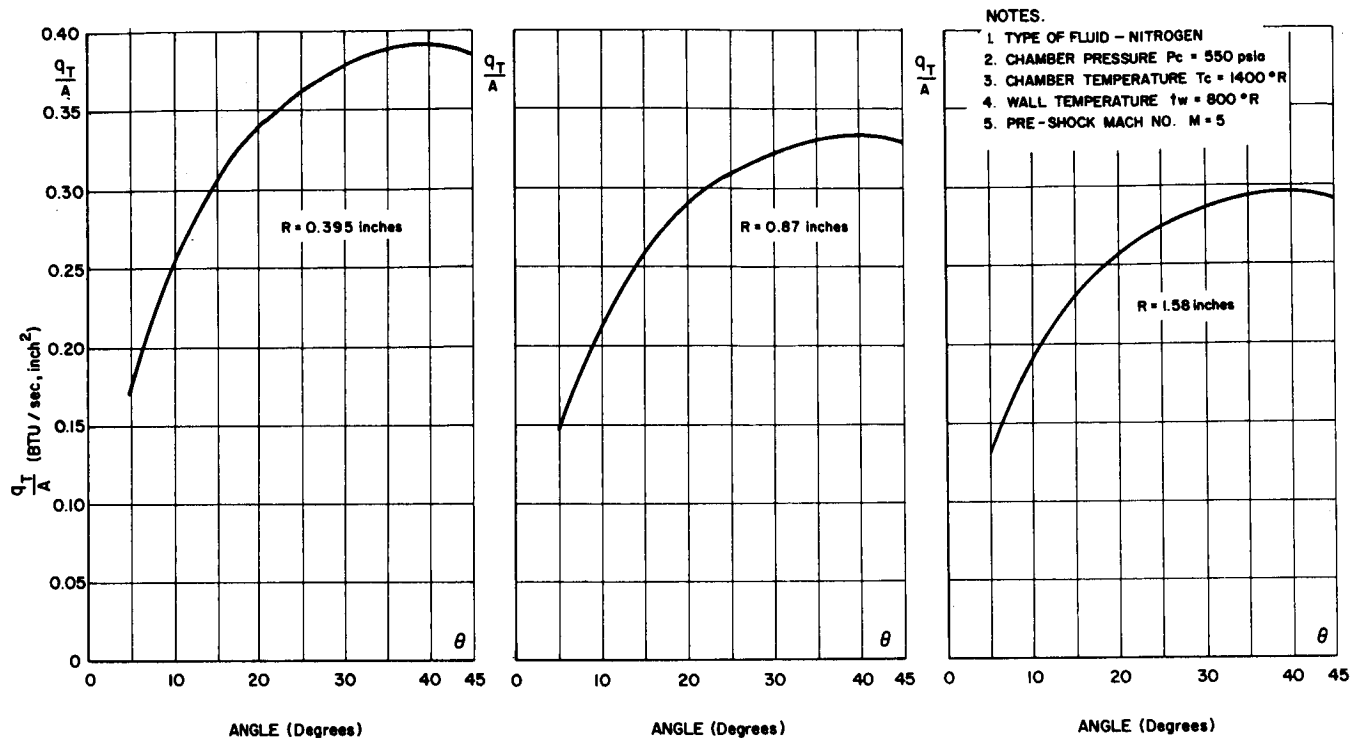


Figure V-13

Turbulent Heating Rates ( $q_t$ ) on a Spherical Centerbody versus  
Nose Radius and Location

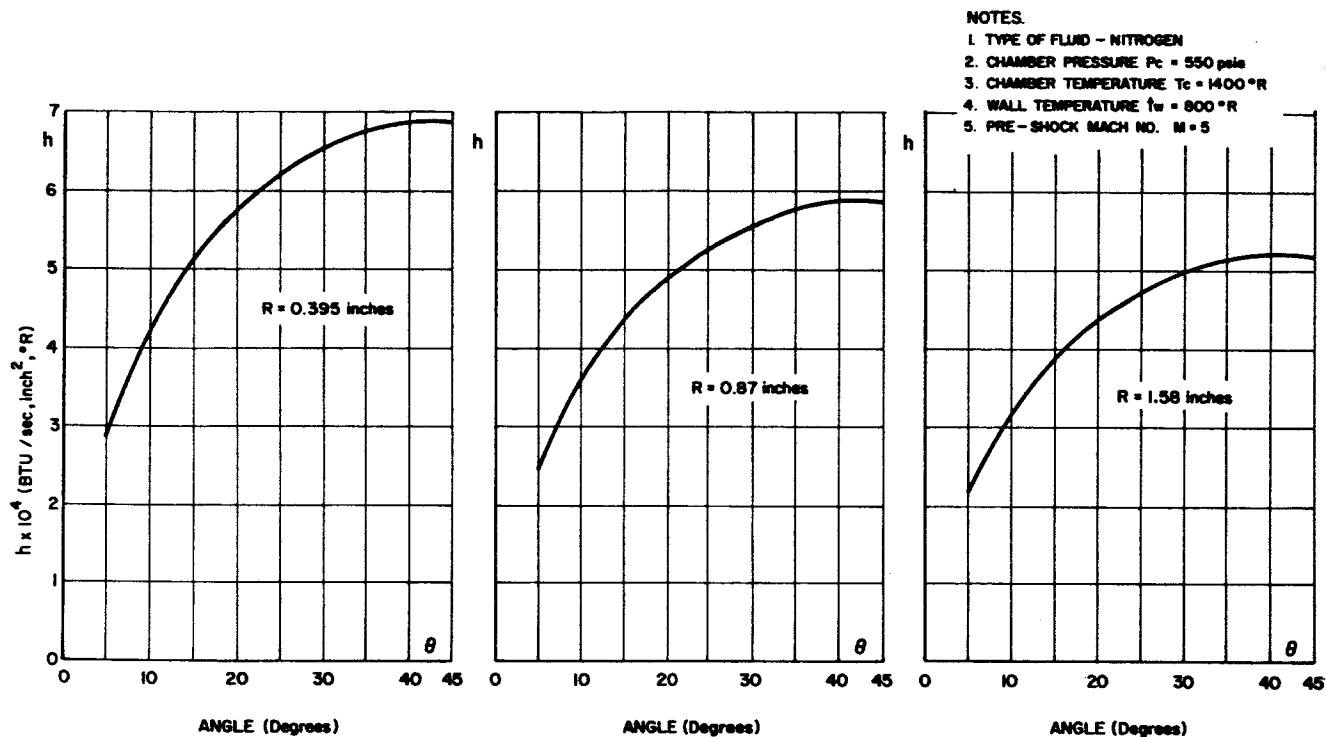


Figure V-14  
Turbulent Heat Transfer Coefficient ( $h$ ) on Spherical Centerbody versus  
Nose Radius and Location

The parameters  $A_\alpha$  and  $B_\alpha$  are mainly dependent upon the cone angle  $\alpha$ . Their formulas are given in Appendix E, where the computed values are given in tabular form (see Tables I and II of Appendix E). Table III gives the values of  $s$  for the corresponding angles  $\alpha$  and  $\theta$ . Tables IV and V list the computed values of  $q_{ws}$  and  $h$ . These are also shown in graphical form by Figures V-15, V-16, V-17.

It can be seen from the results that the heating rates are higher with large cone angles. They drop-off faster with distance along the cone frustum for larger cone angles. For very small angles, the heating rates are almost constant with distance.

These results hold as long as the duct boundary does not impose too much of an area reduction upon the flow. In the latter case, a correction would be necessary.

#### f. Turbulent Heating Rates at Transition Point of Sphere to Cone

In Section V -C-4-d turbulent heat transfer rates were analyzed for the spherical segment between  $0^\circ$  and  $45^\circ$ , where an accurate pressure distribution (Reference 11) is used for a number of points. Unfortunately, the method of Stine and Wanlass does not yield any figures beyond  $45^\circ$  and using a Newtonian pressure distribution would be inconsistent with the work done in Sections V -C-4-c and V -E-4-c. Thus, an approximate procedure had to be used.

Of particular interest are the heating rates at the tangential point of sphere-to-cone, as theoretically this point can be considered as having the highest rate for the conical segment. The following approximation is used to compute a rate for the tangential point to a  $30^\circ$  cone and a nose radius of  $R_0 = 1.58$ -in. This point is located at an angle  $\theta = 60^\circ$ . First, the pressure at this point has to be determined. Using Figure 1 of Appendix C, an extrapolation would indicate a possible range of 0.1 to 0.15 for the energy ratio

$$\frac{p_2}{\rho_{\infty} U^2}$$

These two extremes are used in separate calculations. By the method shown in Appendix C, pressure and temperature, and thus the transport properties  $\rho$  and  $\mu$

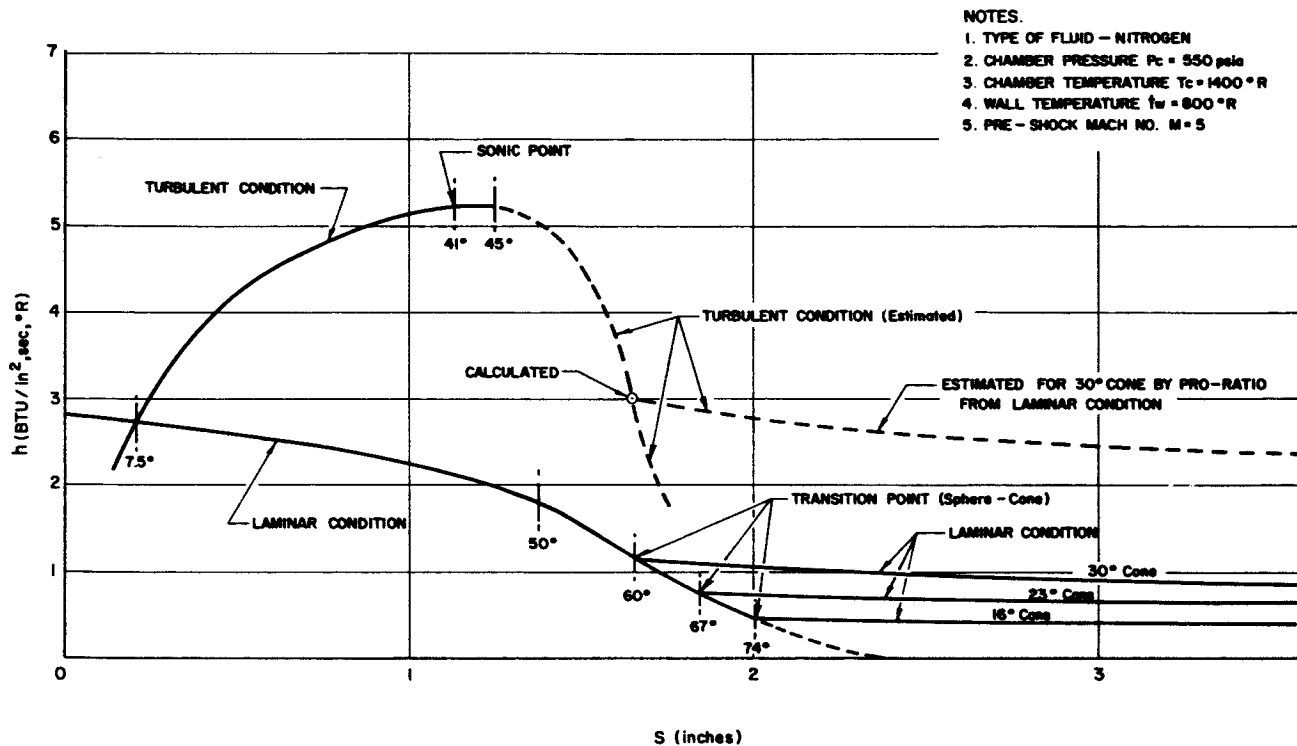


Figure V-15

Composite Heat Transfer Coefficients versus  
Contour Distance from Stagnation Point  
(Nose Radius  $R = 1.58''$ )

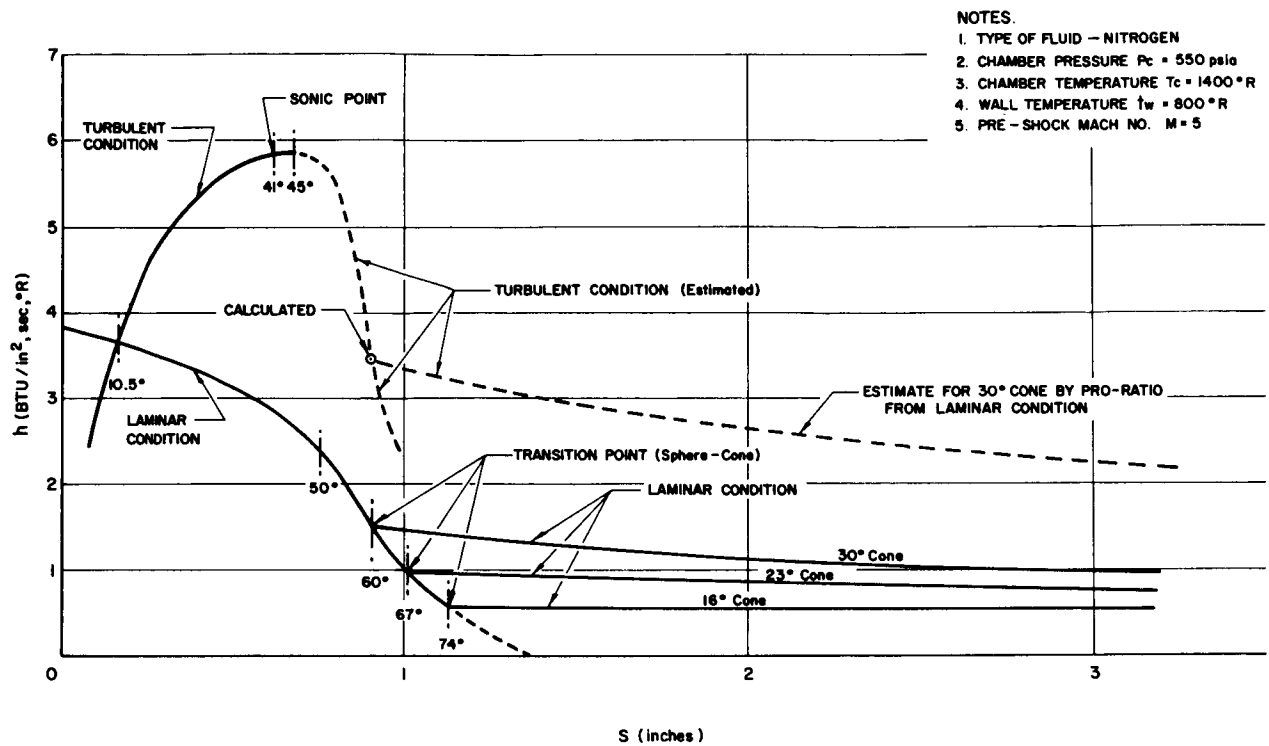


Figure V-16  
 Composite Heat Transfer Coefficients versus  
 Contour Distance from Stagnation Point  
 (Nose Radius  $R = 0.87''$ )

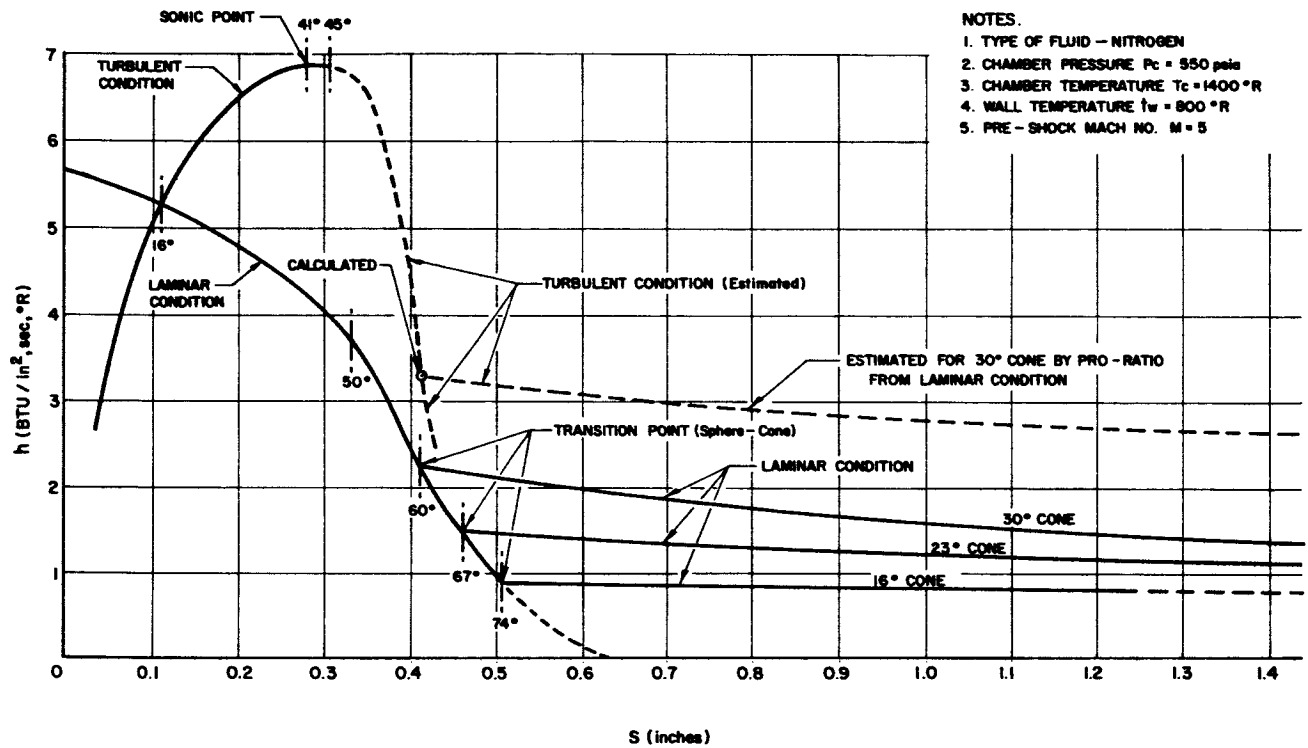


Figure V-17

Composite Heat Transfer Coefficients versus  
Contour Distance from Stagnation Point  
(Nose Radius  $R = 0.395$ " )

are determined. Then the velocity gradient is obtained by using successively relations (10) and (7). Equation (10) yields a laminar value for  $q_w$  and consequently  $h_L$ . Then this value of  $h_L$  is used to obtain  $\frac{\partial U}{\partial X}$  in the form:

$$\frac{\partial U}{\partial X} = \frac{1}{\rho \mu} \left( \frac{144 h_L}{f_L c_p} \right)^2 \quad (12)$$

where  $h_L$  is in BTU/in.<sup>2</sup>-sec-°R

The turbulent value  $h_T$  is obtained from

$$h_T = \frac{f_T c_p}{144} ( \rho^{0.8} \mu^{0.2} ) \frac{\partial U}{\partial X}^{0.8} X^{0.6} \quad (13)$$

For the assumed energy ratios  $\left( \frac{p_2}{p_\infty U^2} \right)$  of 0.1 and 0.15, equation (13) yields values of  $h_T$  equal  $3.08 \times 10^{-4}$  and  $2.94 \times 10^{-4}$ . A value of  $h_T = 3 \times 10^{-4}$  is plotted on Figure V-15. This is close to 60% of the maximum turbulent heat value at the 41° location (sonic point).

#### g. Composite Heating Rates

The analytical studies, as detailed in Sections V-C-4-c, d, e and f, are summarized in graphical form by Figures V-15, V-16, and V-17. The convective heat transfer coefficient  $h$  is shown as a function of  $s$ , which is the centerbody contour distance from the forward stagnation point to any point along the spherical or conical section.

Each of the above figures gives laminar and turbulent flow heat transfer coefficients for a given nose radius. The laminar values were all calculated for the spherical section and three cone angles. The turbulent values were calculated up to a 45° location on the spherical cap. From there on downstream, the values as shown by a dotted line, are estimates based upon a calculated transition point T (see Section V-C-4-f) using pro-ratio and extrapolation on either side of point T. The turbulent values along the conical section are only shown for a 30° cone angle as this is representative of the higher values.

From a closer look and a comparison of all three charts, the following features can be observed:

(1) Except for a small area close to the forward stagnation point, the maximum heating rates are those resulting from turbulent flow conditions.

(2) The absolute maximum for all three nose configurations occurs at approximately  $41^\circ$  from the stagnation point. This location coincides with the region where the flow becomes supersonic (sonic point).

(3) For any given location on spherical cap or cone, the heating rates are highest for the smaller nose radius and they decrease with larger nose configurations.

(4) For the cases under consideration, but not for all possible designs, the laminar heating rate at the forward stagnation point is smaller than the turbulent value at the sonic point.

(5) The intersection of laminar and turbulent curves is located at approximately  $7.5^\circ$  for the larger nose radius, but occurs further away ( $16^\circ$ ) for the smaller nose. There is an uncertainty where the transition from laminar to turbulent flow may happen and thus it may not occur at or close to the intersection of the two curves. If, for example, the transition would happen downstream from the intersection, then this fact would result in a sudden sharp increase of the heating rates.

(6) Laminar heating rates are highest at the forward stagnation point and decrease from there on along spherical and conical contour.

(7) Turbulent heating rates rise from zero at the stagnation point to a maximum at the sonic point and then decrease sharply along the spherical cap. On the conical surface, the decrease is only very slight at best.

(8) Forming the ratio of maximum turbulent heat transfer coefficient to that at the stagnation point for laminar flow, it is seen that for the smaller nose size, this ratio is 1.17 while it becomes 1.77 for the

large configuration. This comes mainly from the fact that the transport properties are evaluated at the 0.8 power for the turbulent flow versus a 0.5 power for laminar flow. Thus, the maximum heating rate does not change as fast with a change in nose radius than the value at the stagnation point.

All the above conclusions are purely theoretical and based upon unrestricted gas flow over blunt bodies. In the small scale tests, it is assumed that this condition prevails for the spherical portion of the centerbody and a good part of the cone frustrum. However, the flow area restriction from the duct boundaries may become large enough in the downstream section of the cone frustrum to exert an influence upon the convective heat transfer.

Thus, it is entirely possible that the trend, as shown on the graphs of Figures V-15, -16, and -17 by the dotted line, could be reversed and that an increase in heating rates could be in effect by the time the flow enters the second-throat region. Although the heating rates may be higher at the downstream portion of the conical section than shown by the graphs, it still would be considerably lower than the maximum heating rate at the sonic point.

#### h. Heat Transfer Rates to Centerbody Mounting Struts

The struts which serve to position the centerbody and attach it to the duct wall should be designed so as to be capable of withstanding the aerodynamic and thermodynamic effects from a high velocity gas stream. As this stream may be supersonic, it is of prime interest to estimate the heat transfer rates as a function of (1) the strut bluntness, (2) the comparative bluntness ratio of centerbody to strut and (3) Mach number.

Heat flux computations were performed for an hypothetical case with conditions close to those of the full scale model, i.e., use of hydrogen gas at 800 psia, 5000°R chamber temperature and a wall cooled to 1500°R. For such a case, Lester Lees' method is fully valid and was used because it allows adjustment for flow at the cylindrical surface of the struts versus the spherical surface of the centerbody. Equation (14) was used with a constant of 0.47 versus 0.707 for the centerbody tip.

The major assumptions used with the computations included:

- (1) Continuous steady-state flow with no loss in total temperature.
- (2) Mach number 5 ahead of the bow shock at the center body nose.
- (3) Circular curvature for both centerbody nose and strut edge.
- (4) Constant values of 1.4 for the specific heat ratio and 0.68 for the Prandtl Number.
- (5) Three possible values of 2.0, 1.5 and 1.0 for the Mach number for the flow ahead of the bow shock at the struts.
- (6) Constant wall surface temperatures of 1500°R.

As can be seen from the computations, (Appendix F), the heat flux to the struts is referenced to the stagnation point heat transfer at the centerbody nose for laminar boundary conditions. The latter value was previously calculated and found to be  $(q_{wo})_{CB} = 423/\sqrt{R_{OCB}}$  BTU/ft<sup>2</sup>-sec, where the nose curvature radius is given in feet. The use of dimensionless heating rates at the struts has the advantage of minimizing errors resulting from certain assumptions or divergences between predictions and test results.

Densities were computed from the ideal gas law. Viscosities (Figure V-18) were taken from Aerojet Report 9050-65, temperatures and pressures from NACA-R1135 tables.

The heat flux to the struts is given in the form  $(q_w)_o = \frac{C}{\sqrt{R_o}}$ , which shows that it is inversely proportional to the square root of the circular curvature radius. The value of C is related to the assumed Mach number and found to vary from 44.7 for M = 1 to 172 for M = 2.

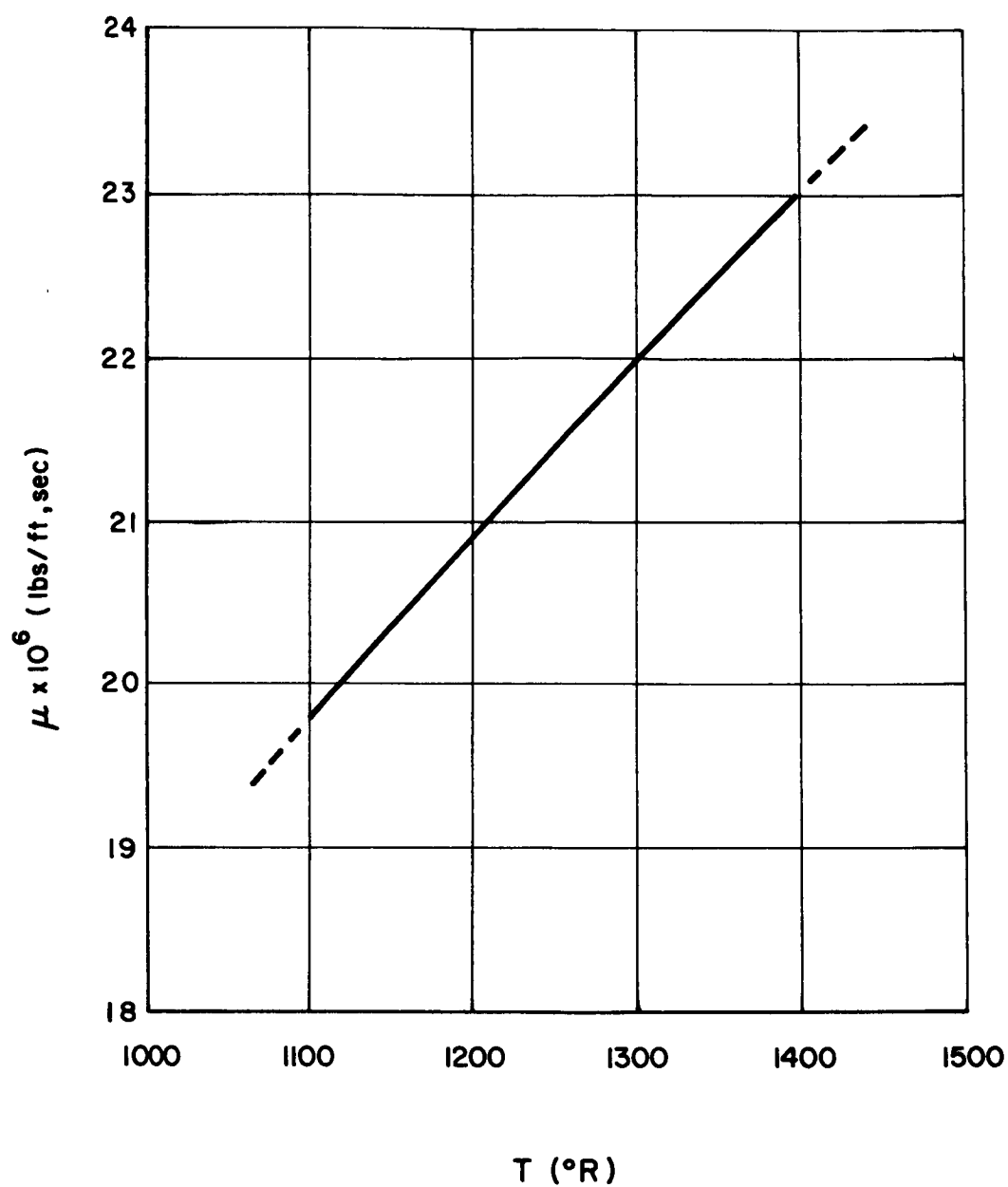


Figure V-18

Dynamic Viscosity  $\mu$  of  $\text{N}_2$  as a Function of Absolute Temperature  
V-38

Table F-2 of Appendix F gives the dimensionless heat flux at the struts as a function of Mach number and ratio of curvature radii. It shows that these values could be as low as 10% and as high as 81% of the heating rate at the nose.

Once structural requirements for the struts are satisfied, the major concern is to limit the size of the struts to a minimum but keeping the heat rate below the one expected for the nose. If the Mach number were higher than 2 or the strut smaller than one quarter that of the nose radius, the  $q_w$  - ratio could become larger than 1. The expected Mach number is less than 2; therefore, it is recommended that the struts be built for all tests with a radius of one quarter that of the largest centerbody nose radius.

#### D. COMPARISON OF EXPERIMENTAL AND ANALYTICAL RESULTS

The experimentally determined heat transfer coefficients for the nine nosecones tested are presented in Figures V-1 through V-9, and the corresponding analytical results are presented in Figures V-10 through V-18.

##### 1. Stagnation Region on Nosecone (Spherical Segment)

The experimentally determined heat transfer coefficients measured at and near the centerbody stagnation point were lower than predicted by theory. To be on the conservative side, the analytical values should be used when considering coolant requirements near the centerbody stagnation region.

##### 2. Conical Section of Nosecone

An approximate analytical method was used to predict the heat transfer coefficients. Comparison of the experimental heat transfer coefficients along the conical sections with the approximate analytical heat transfer coefficients shows (a) the analytical heat transfer coefficients to be higher than the experimental near the transition (sphere-cone) section, and (b) the experimental coefficients to be higher than the analytical near the downstream section of the conical section. For design purposes, the higher value of the heat transfer coefficient should always be used.

The reasons for the increase in the experimental heat transfer coefficient with increase in position(s) along the nose piece conical section are because of the decrease in diffuser cross-sectional flow area with increase in position(s) and because of the pressure of oblique shock waves which are reflecting off the centerbody surfaces. The approximate analytical model did not include these effects.

### 3. Adjustment of Analytical Prediction

The experimental results have to be corrected for the various heat losses, calibration errors, or other factors which normally occur in a routine test procedure. However, in order to allow a fair comparison, the analytical predictions must also be corrected to conform to the individual test conditions. These include geometrical changes which normally stay the same for all tests, plus the changes in operating conditions, i.e., the variations from test to test of chamber pressure and temperature. The latter influence the transport properties, mainly the density and viscosity, while the specific heat is assumed constant. The geometrical deviations cause a change in Mach number, which in turn influences the value of the velocity gradient.

With these facts in mind, conversion formulas have been developed, one for laminar and one for turbulent flow. In Section V-C-e, it is shown that the heating rates along the cone frustum are referenced to the forward stagnation point. Thus, the conversion formulas listed below are applicable for both the spherical and conical sections.

Laminar Flow:

$$\left( \frac{h_{th}}{h_{pr}} \right)_L = \frac{0.0285 (T_R)_{pr}}{(P_c \mu)_{pr}^{0.5}} \quad (14)$$

Turbulent Flow:

$$\left( \frac{h_{th}}{h_{pr}} \right)_T = \frac{2.04 (T_R)_{pr}^{0.4}}{(P_c)^{0.8} \mu_{pr}^{0.2}} \quad (15)$$

where  $(T_T)_{pr}$  and  $(P_c)_{pr}$  are obtained from the reduced test data and the viscosity  $\mu_{pr}$  from Figure V-18.

The heat transfer parameters  $f_L$  and  $f_T$  are also considered constant and thus are not contained in the conversion formulas. It should be noted that the theoretical values of these parameters were taken from a paper by Stine and Wanlass (Reference 12). However, Van Driest showed that experimental values of  $f$  occupy a broad range from 10% higher to 15% lower than the theoretical values (compare Reference 10, Figure 25). Consequently, for this factor alone, experimental heating rates may be higher or lower by the above amounts.

#### E. SCALING OF RESULTS TO FULL SIZE NERVA II DIFFUSER

##### 1. Heat Transfer

Conversion from the small scale heat transfer data to those for full scale NERVA II not only involves an appreciable change in hardware size, but also that of the operating fluid, i.e., from nitrogen to hydrogen, plus a higher chamber temperature. Developed conversion formulas are normally based on those used for the small-scale data. They present the great advantage of avoiding repetitious detail work. Their use is generally justified after a good confidence level has been reached for the subscale data, based upon a certain agreement between analytical predictions and experimental test results. Unfortunately, this prerequisite has not been reached, as divergences between analytical and experimental work remain unexplained.

As the analytical methods used have been proven correct in numerous technical applications in the aircraft field, and because their results are much more conservative than those obtained from the tests, it is recommended that the scale-up procedure be based upon available theories as used in Section V-C, with the actual full-scale parameters.

The change from the relatively low nitrogen temperature of 1400°R, involves gas dissociation effects. A preliminary study was made to evaluate trend

and amplitude of gas dissociation resulting from the 4500°R hydrogen gas. It was found that, because of dissociation, the heating rates are higher by about 10%. A procedure to perform more exact calculations on dissociated gases is given in the paper by Fay and Ridell (Reference 7 Equations 45 and 46, and Reference 8, Equations 7 and 8).

## 2. Aerodynamic

The aerodynamic performance, pressure profile, and local Mach numbers of the full scale duct will be essentially the same as those obtained from the sub-scale model because of the independence of scale size (boundary layer is small with respect to physical dimensions of scale model), working fluid (the ratio of specific heats are the same), and total temperature on the pressure and Mach number.

### F. AERODYNAMIC PERFORMANCE

#### 1. Diffuser Performance

Diffuser performance is defined as the effect of engine chamber pressure on the pressure in the environmental cell. This definition is simple and general and can be applied to any of the diffuser types which are currently used to simulate altitude conditions during the static testing of rocket propulsion systems.

During the present program, only the nose cone shape (cone angle and nose radius) was varied; all other geometric parameters were unchanged; thus, the nose cone shape was the only parameter affecting diffuser performance from an aerodynamic viewpoint, and was therefore the parameter to be studied and evaluated.

#### 2. Method

To obtain aerodynamic (fluid flow) performance data during the pressure profile tests, the chamber pressure was raised at an approximate rate of 30 psi/sec from ambient to 650 psia using heated nitrogen as the working fluid.

This relatively slow rise of chamber pressure permits accurate correlation of chamber pressure with the cell pressure and the other pressures being recorded in the centerbody diffuser system, and this in turn enhances the performance evaluation of the various nose cones undergoing testing.

### 3. Test Results

Figures V-19 through V-22 show the performance data of a typical centerbody diffuser tested. The diffuser starting pressure  $(P_c/P_a)_{st}$  was between 32.5 to 34 for all the nose cone configurations tested during this program and the average starting pressure ratio was approximately 33.

### 4. Discussion of Results

#### a. Test Data Correlation

Attempts to correlate the diffuser starting pressure ratios with the nose cone shapes, i.e., cone angles and nose radii, were unsuccessful. It is evident from examination of the test data that the range of centerbody nose cone angles and nose radii tested had practically no influence on the diffuser starting pressure ratio.

#### b. Comparison of Test Data with Other Experimental Test Data and Theory

Table V-2 presents and compares diffuser starting pressure ratio  $(P_c/P_a)_{st}$  for the present test series with theory and with other experimental data.

NOTES.

1. RUN NO. D-285-LQ-4
2.  $\epsilon = 40/1$  CONTOURED NOZZLE
3. WORKING FLUID -  $1390^{\circ}\text{R}$   $\text{GN}_2$  ;  $15 < P_c < 616$  at 29 psia/sec
4. CONFIGURATION -  $0.87''\text{R} \times 30^{\circ}$  NOSECONE

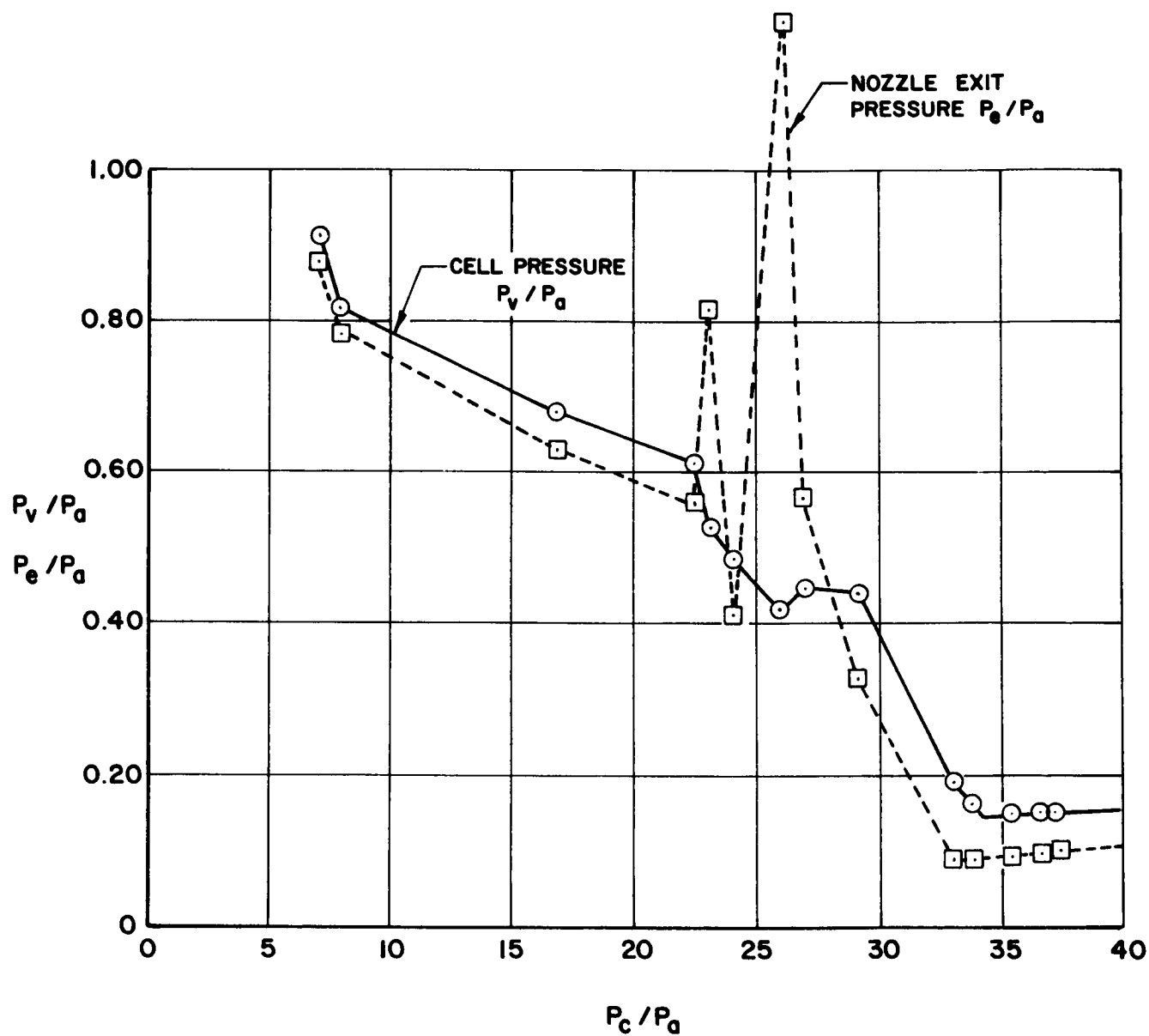


Figure V-19

Cell and Nozzle Exit Pressures versus Nozzle Chamber Pressure

NOTES.

1. RUN NO. D-285-LQ-4
2.  $\epsilon = 40/1$  CONTOURED NOZZLE
3. WORKING FLUID - 1390 °R  $\text{GN}_2$  ;  $15 < P_c < 616$  at 29 psia/sec
4. CONFIGURATION - 0.87" R x 30° NOSECONE

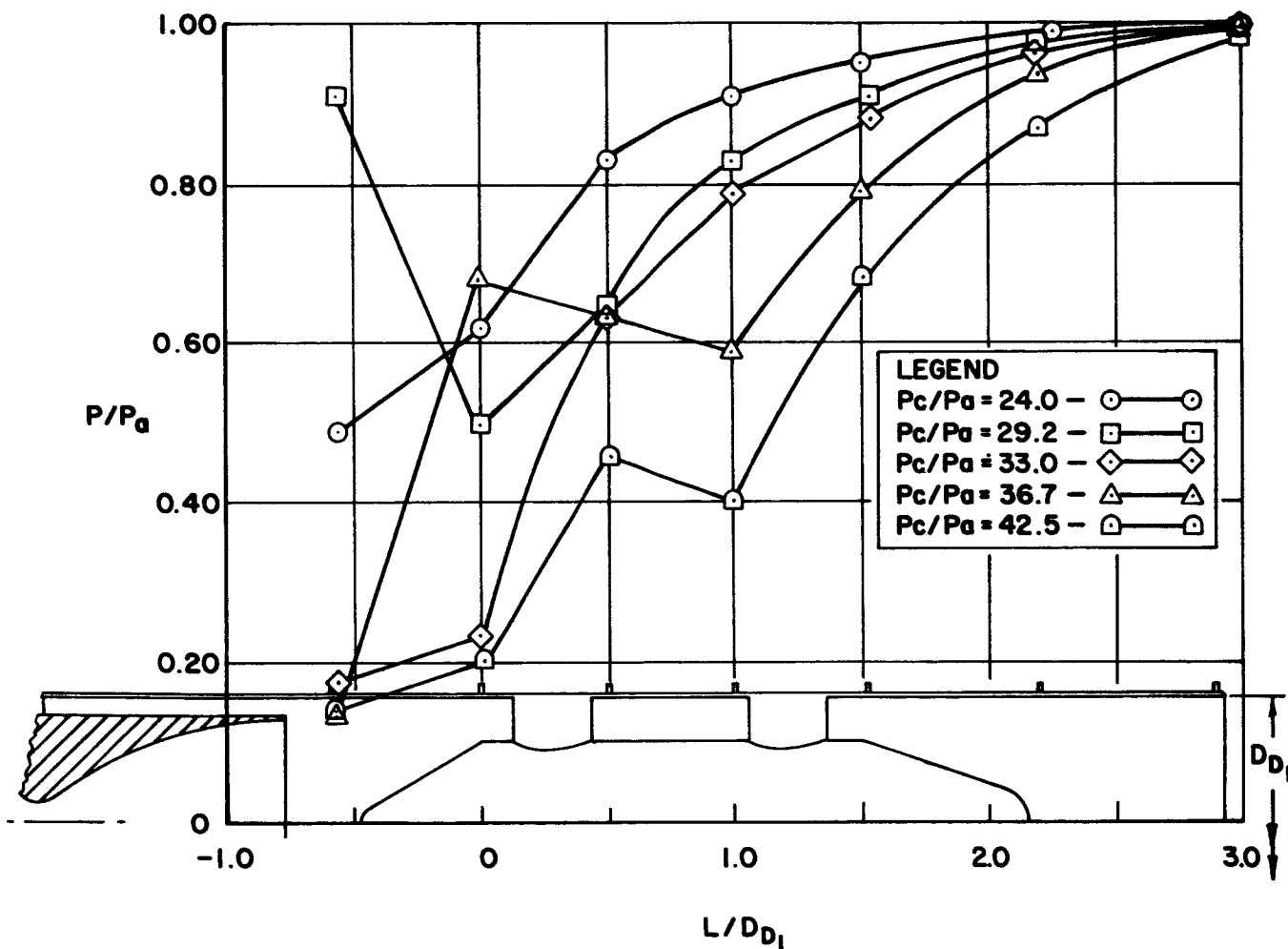


Figure V-20

Static Wall Pressures versus Longitudinal Position

NOTES.

1. RUN NO. D-285-LQ-4.
2.  $\epsilon = 40/1$  CONTOURED NOZZLE
3. WORKING FLUID -  $1390^{\circ}\text{R}$   $\text{GN}_2$  ;  $15 < P_c < 616$  at 29 psia/sec
4. CONFIGURATION -  $0.87\text{ R} \times 30^{\circ}$  NOSECONE

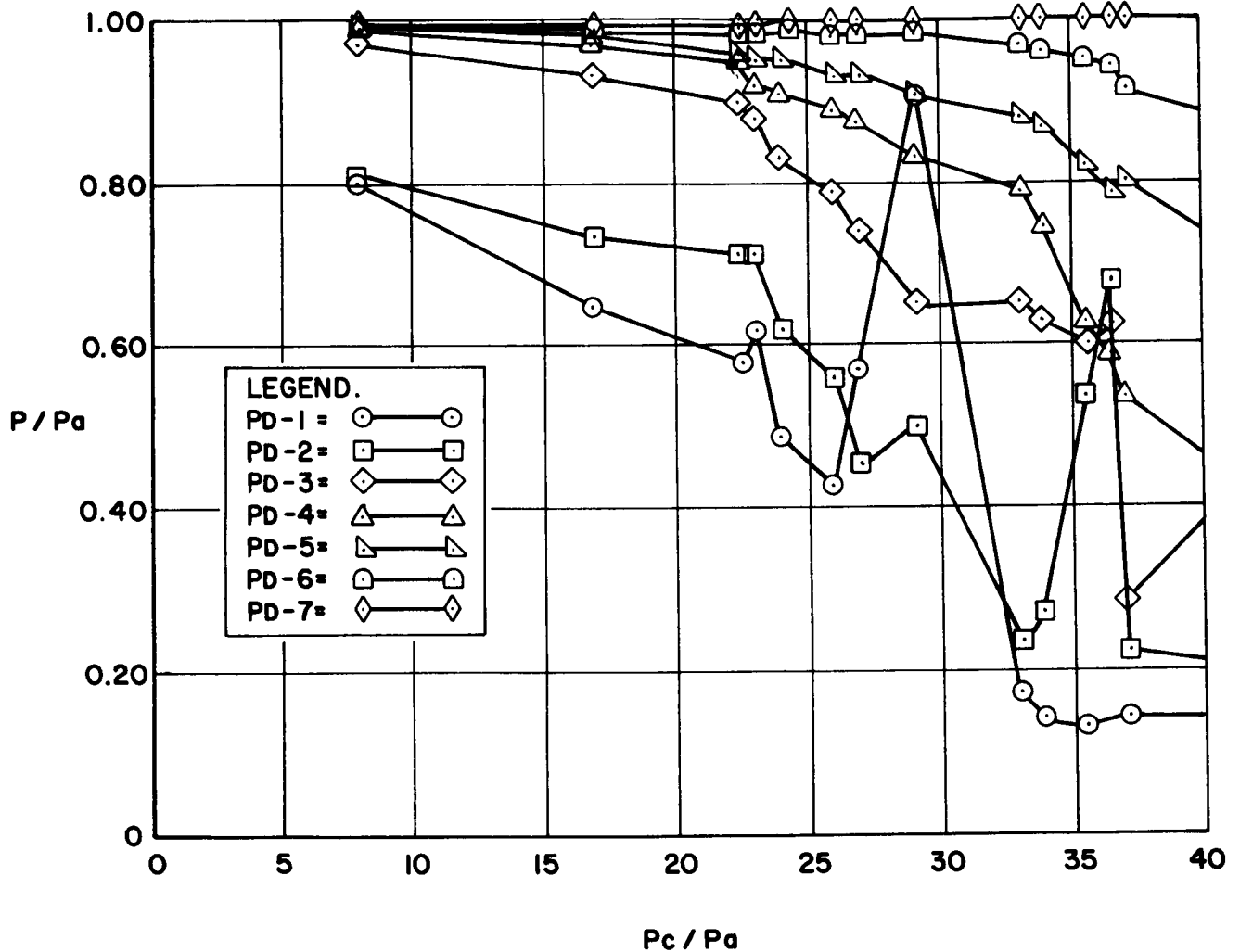


Figure V-21

Static Wall Pressures versus Nozzle Chamber Pressure

NOTES.

1. RUN NO. D-285-LQ-4
2.  $\epsilon = 40/1$  CONTOURED NOZZLE
3. WORKING FLUID - 1390°R  $\text{GN}_2$  ;  $15 < P_c < 616$  at 29 psia/sec
4. CONFIGURATION - 0.87" R x 30° NOSECONE

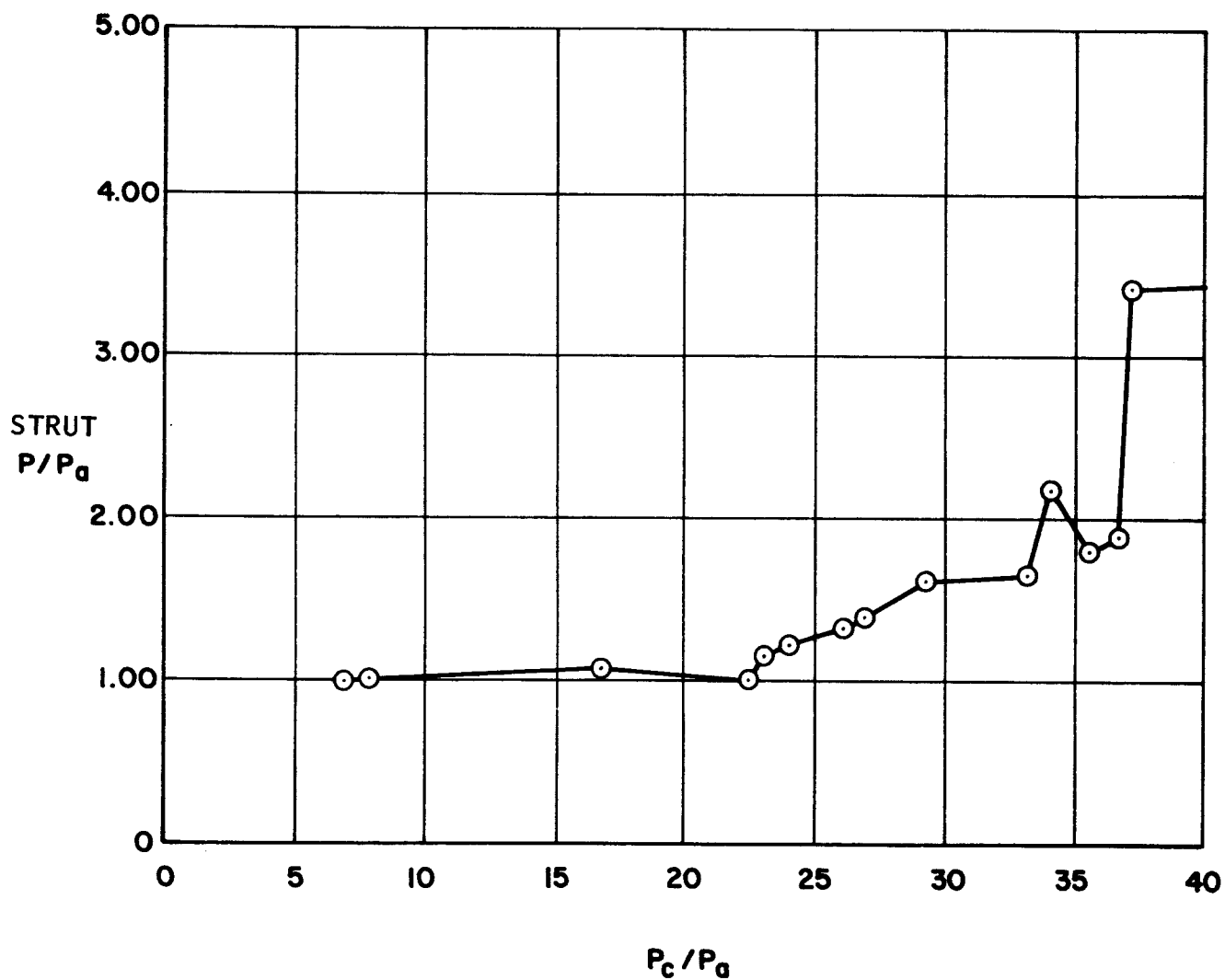


Figure V-22

Stagnation Pressure of Front Strut versus Nozzle Chamber Pressure

TABLE V-2  
COMPARISON OF TEST DATA WITH OTHER TEST DATA AND THEORY

<u>FLOW MODEL</u>	<u><math>(P_c/P_a)_{st}</math></u>	<u>REMARKS</u>
Centerbody Test Data for Present Program	32.5 to 34.0	See Figure IV-1 for Description of Centerbody Geometry
Figure 12 of NASA TN D-1306	29	Data for Centerbody Diffuser System
Figure 16 of NASA TN D-298	30	Cold Flow Air Data for Cylindrical- Exhaust-Diffuser ( $A_{D_t}/A^* = 38.2$ )
Normal Shock Theory Model - Total to Static Pressure	27.5	
Normal Shock Theory Model - Total to Total Pressure	24.5	
Figure 39 of AGC Report 2403	29	Hot Gas Data ( $\gamma = 1.4$ ) for Cylindrical-Exhaust-Diffuser with 90° Supersonic Turn for $A_{D_t}/A^* = 35$ and $A_{D_1}/A^* = 58.2$

### References

1. AGC Memorandum 7436-3:M0016 dtd 21 December 1964, Subject, Ejector - Diffuser References, by P. JOERG, Aerojet-General Corporation, Sacramento, California
2. SIBULKIN, M., "Heat Transfer Near the Forward Stagnation Point of a Body of Revolution." Convair Report ZA-7-016, April 1956, San Diego, California.
3. MARK, R., "Compressible Laminar Heat Transfer Near the Stagnation Point of Blunt Bodies of Revolution." Convair Report ZA-7-016, April 1956, San Diego, California.
4. ROMIG, M.F., "Stagnation Point Heat Transfer for Hypersonic Flow." Jet Propulsion, December 1956, pp. 1098-1099.
5. COHEN, C., and RESHOTKO, E., "Heat Transfer at the Forward Stagnation Point of Blunt Bodies." NACA-TN-3513, July 1955.
6. LEES, L., "Laminar Heat Transfer Over Blunt-Nosed Bodies at Hypersonic Speeds." Jet Propulsion, Volume 26, No. 4, pp. 259-269, 1956.
7. FAY, J. A., RIDDELL, F. R. and KEMP, N. H., "Stagnation Point Heat Transfer in Dissociated Air Flow." Jet Propulsion, June 1957, pp. 672-674.
8. FAY, J. A. and RIDDELL, F. R., "Theory of Stagnation Point Heat Transfer." Journal of Aeronautical Sciences, pp. 73-85, February 1958.
9. VAN DRIEST, E.R., "The Problem of Aerodynamic Heating." Aeronautical Engineering Review, October 1956, pp. 26-41.
10. VAN DRIEST, E. R. "Turbulent Flows and Heat Transfer," Section F of Volume V, pp. 339 to 427: High Speed Aerodynamics and Jet Propulsion, Princeton University Press, Princeton, New Jersey, 1959.
11. VAN DYKE, M.D. and GORDON, H. D. "Supersonic Flow Past a Family of Blunt Axisymmetric Bodies." Ames Research Center, Moffett Field, California, 1959. NASA Technical Report TR-1.
12. STINE, H. A. and WANLASS, K. "Theoretical and Aerodynamic Heating and Isothermal Heat Transfer Parameters on a Hemispherical Nose with Laminar Boundary Layer at Supersonic Mach Numbers." NACA-TN-3344, December 1954.
13. PROBSTEIN, R. "Inviscid Flow and Heat Transfer in the Stagnation Point Region of Very Blunt-Nosed Bodies." Avco-Everett Research Lab., Everett, Mass., January 1957.
14. LEES, L. and KUBOTA, T. "Inviscid Hypersonic Flow Over Blunt-Nosed Slender Bodies," Journal of the Aeronautical Sciences, Volume 24, No. 3, March 1957.

15. DETRA, R. W. and HIDALGO, H. "Generalized Heat Transfer Formulas and Graphs for Nose Cone Re-entry Into the Atmosphere." Avco-Everett Research Laboratory, ARS-Journal, March 1961, pp. 318-321.
16. PATMOR, G. O., MC FARLAND, B. L., NELSON, R. E., and MANDELL, B. "A Heat Transfer Investigation of Ejector Systems with 90° Turns." Space Simulation Conference, Pasadena, California, November 1964. AIAA - Publication CP-11.
17. TRUITT, R. W. "Fundamentals of Aerodynamic Heating" and "Hypersonic Aerodynamics," The Ronald Press Company, New York.

## APPENDIX A

### METHOD FOR CORRECTING INDICATED HEAT TRANSFER CONVECTION COEFFICIENTS FOR LONGITUDINAL CONDUCTION EFFECTS IN THIN-WALLED SECTIONS

#### I. INTRODUCTION

Presented herein is a method for correcting indicated heat transfer coefficients obtained by measurement (1) near the flow stagnation point on a thin-walled spherical segmented nosed centerbody and (2) along the edge of a thin-walled conical section. The thin-walled body sections are aerodynamically heated by an axially symmetric flow. The method presented here is for correction of longitudinal conduction effects. Because of a variation in the local convection coefficient along the thin-wall bodies, heat will be transferred in the longitudinal direction. This longitudinal transfer of heat will cause hotter spots to appear cooler and cooler spots to appear hotter.

The method used to correct the measured values of the local convection coefficient is the same as that presented in Reference (a), except that the effects of longitudinal area change are included.

## II. DISCUSSION

### A. GENERAL

In this analysis for correcting for longitudinal conduction effects, the thin-walled shells of both the spherical nose segment and the conical section were assumed to be made up of ring-like sections.\* (Cross-sections of these sections are shown in Figures A-1 and A-2). The rings are formed by revolving any cross-sectional increment ( $\delta x_n$ ) with temperature  $T_n$  around the centerline of the centerbody. The thermal properties of any ringed sections can be analyzed by considering the cross-sectional increments since the flow about the centerbody is axially symmetric. Therefore, a thermocouple placed on the inside of any thin-walled ring will measure essentially the average temperature of that particular ringed section. Using any three adjacent ringed sections (geometry shown in Figure A-3), the following heat balance can be derived.

$$h_n(T_R - T_n)A_{g_n} \Delta\beta + \frac{k(T_{n-1} - T_n)A_{c_{n(n-1)}}\Delta\beta}{\Delta x_{n(n-1)}} + \frac{k(T_{n+1} - T_n)A_{c_{n(n+1)}}\Delta\beta}{\Delta x_{n(n+1)}} = M_n C \Delta T_n$$

where  $A_{c_{n(n-1)}}$  = conduction area between increments  $\Delta x_{n-1}$  and  $\Delta x_n$   
 $A_{c_{n(n+1)}}$  = conduction area between increments  $\Delta x_n$  and  $\Delta x_{n+1}$   
 $A_{g_n}$  = area of the increment  $\Delta x_n$  which is heated by convection  
 $M_n$  = mass of increment  $\Delta x_n$

$T_{n-1}, T_n, T_{n+1}$  = respective temperatures of increments  $\Delta x_{n-1}, \Delta x_n$ , and  $\Delta x_{n+1}$  at beginning of time interval ( $\Delta\beta$ )

$\Delta T_n$  = temperature rise of increment end of time interval ( $\Delta\beta$ )

---

\* All sections are ring-like shells except the section at the stagnation point of the spherical nose segment which is essentially saucer shaped.

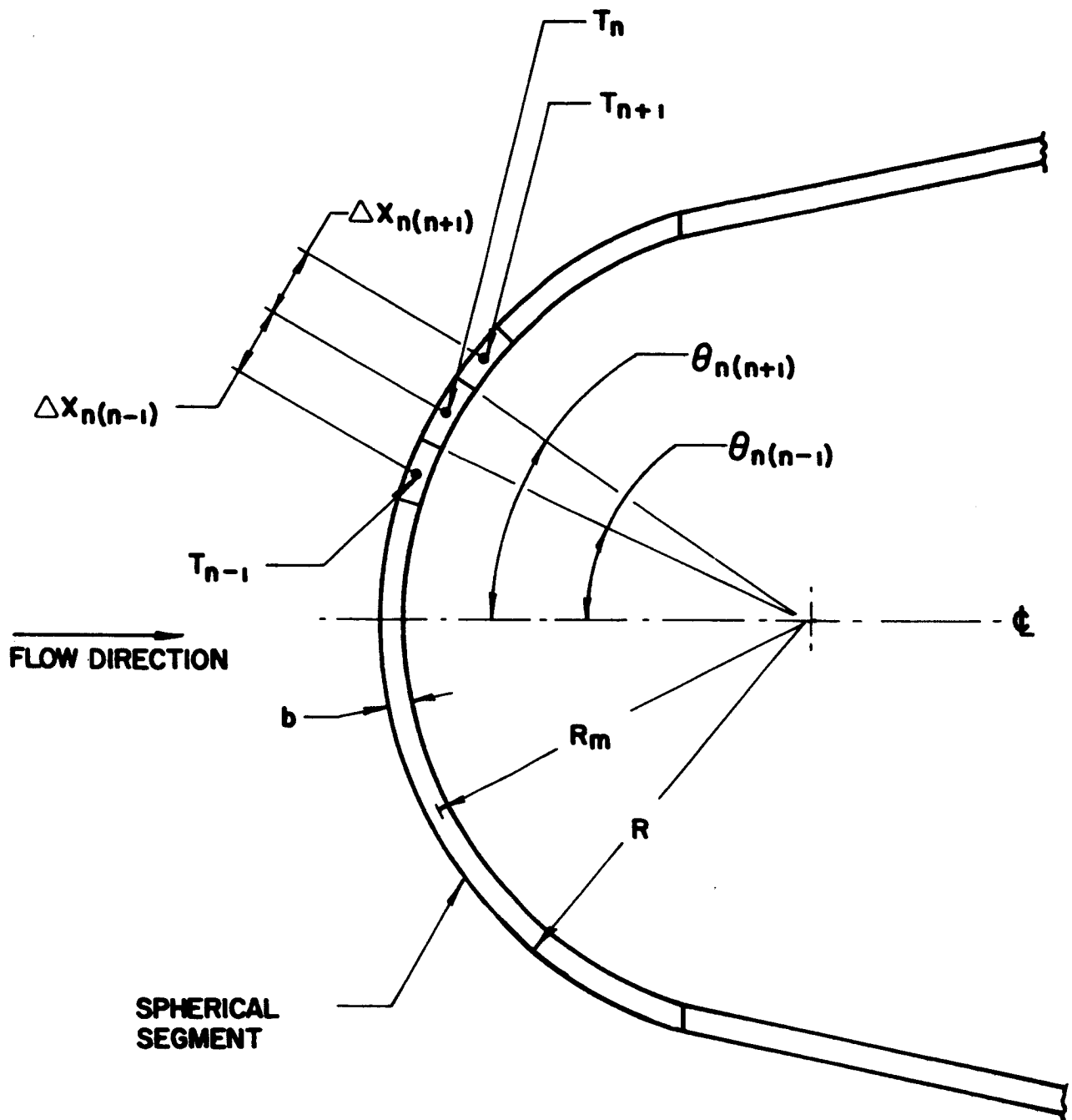


Figure A-1  
 Geometry used for Spherical Nose Segment  
 A-3

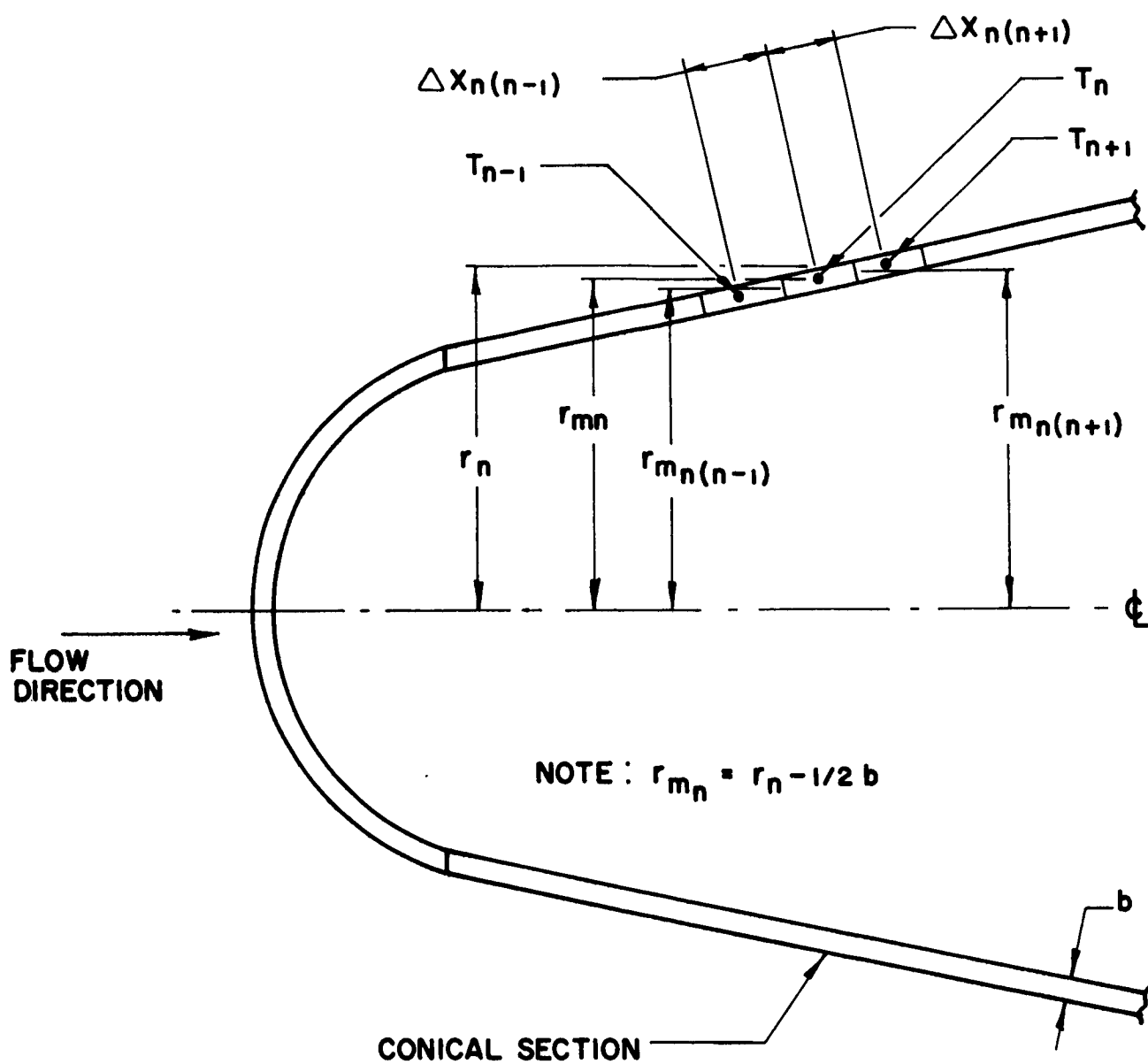


Figure A-2  
 Geometry used for Conical Section  
 A-4

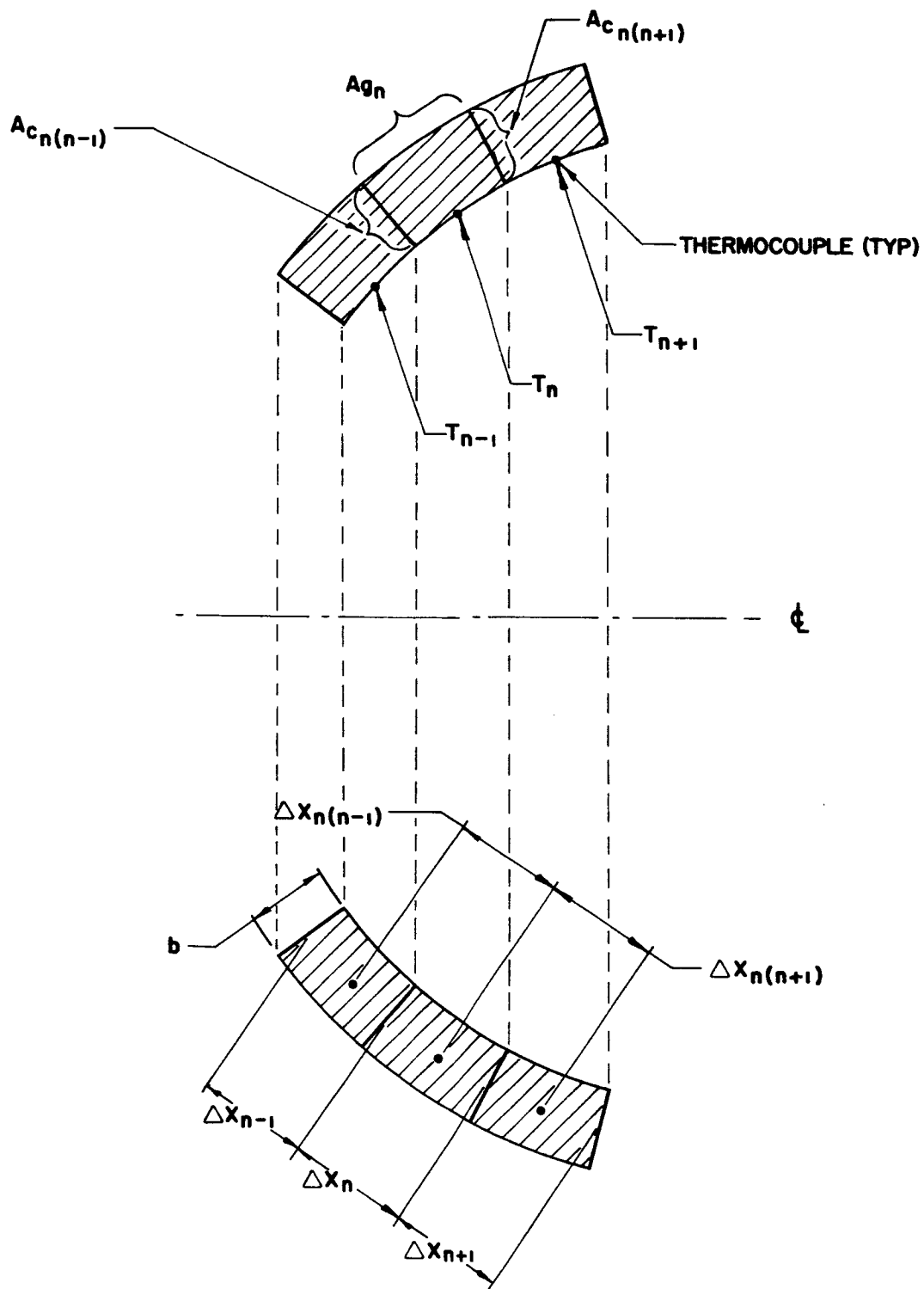


Figure A-3

Typical Geometry used in Analysis

The above method was applied to the spherical nose segment and the conical section and the resulting equations are presented in the next section under Method.

## B. METHOD

### 1. Spherical Nose Segment

The equation which gives the corrected value ( $h_n$ ) of the local convection coefficient for the spherical segmented nose (see geometry in Figure 1) is:

$$h_n = h'_n \left( \frac{R_M}{R} \right)^2 - \frac{kbR_M}{R^2 [\cos \theta_{n(n-1)} - \cos \theta_{n(n+1)}]} \left\{ \frac{\sin \theta_{n(n-1)}}{\Delta x_{n(n-1)}} \frac{T_{n-1} - T_n}{T_R - T_n} + \frac{\sin \theta_{n(n+1)}}{\Delta x_{n(n+1)}} \left( \frac{T_{n+1} - T_n}{T_R - T_n} \right) \right\} \quad \text{Eq. (1)}$$

See Figure 1 and Nomenclature for an understanding of the terms in Equation (1).

Equation (1) can also be used in the form:

$$h_n = h'_n \left( \frac{R_M}{R} \right)^2 - \frac{kbR_M}{R^2 [\cos \theta_{n(n-1)} - \cos \theta_{n(n+1)}]} \left\{ \frac{\sin \theta_{n(n-1)}}{\Delta x_{n(n-1)}} \left[ 1 - e^{-\beta(a_n - a_{n-1})} \right] + \frac{\sin \theta_{n(n+1)}}{\Delta x_{n(n+1)}} \left[ 1 - e^{-\beta(a_n - a_{n+1})} \right] \right\} \quad \text{Eq. (2)}$$

where  $-a_n = \ln \left( \frac{T_R - R_n}{T_R - T_i} \right);$

$-a_{n-1} = \ln \left( \frac{T_R - T_{n-1}}{T_R - T_i} \right)$  and  $-a_{n+1} = \ln \left( \frac{T_R - T_{n+1}}{T_R - T_i} \right)$

## 2. Conical Section

The equation which gives the corrected value ( $h_n$ ) of the local convection coefficient along the edge of a conical section (see geometry in Figure 2) is:

$$h_n = h'_n \left( \frac{r_{M_n}}{r_n} \right) - \frac{kb}{\Delta X_n r_n} \left\{ \frac{r_{M_{n(n-1)}}}{\Delta X_{n(n-1)}} \left( \frac{T_{n-1} - T_n}{T_R - T_n} \right) + \frac{r_{M_{n(n+1)}}}{\Delta X_{n(n+1)}} \left( \frac{T_{n+1} - T_n}{T_R - T_n} \right) \right\} \quad \text{Eq. (3)}$$

See Figure 2 and Nomenclature for an understanding of the terms in Equation (3). Equation (3) can also be used in the form:

$$h_n = h'_n \left( \frac{r_{M_n}}{r_n} \right) - \frac{kb}{\Delta X_n r_n} \left\{ \frac{r_{M_{n(n-1)}}}{\Delta X_{n(n-1)}} (1 - e^{\beta(a_n - a_{n-1})}) + \frac{r_{M_{n(n+1)}}}{\Delta X_{n(n+1)}} (1 - e^{\beta(a_n - a_{n+1})}) \right\} \quad \text{Eq. (4)}$$

### C. DISCUSSION OF METHOD

This method presented herein in the application of finite difference techniques to approximate conditions which would otherwise have to be solved by complicated differential equations. The cardinal assumption (see Reference 1, page 66) used in this method is that the temperature ( $T_n$ ) at any location can be represented as an exponential function of time, i.e.:

$$T_n = T_R - (T_R - T_i) e^{-a_n \beta}$$

where  $a_n$  is a constant for that particular location and  $T_i$  is the initial wall temperature at time  $\beta = 0$ . This assumption greatly reduces the labor of computation with a very small error introduction.

It should be noted that Equations 1, 2, 3 and 4 are set up to account for the case of unequal distances between thermocouple locations. It would be desirable to have equal distances between thermocouple locations, but this condition is not mandatory. In case the distances between thermocouple locations are not equal, then some discretion should be used assigning incremental lengths to each thermocouple location.

### III. CONCLUSIONS AND RECOMMENDATIONS

#### A. CONCLUSIONS

The method presented herein can be satisfactorily used to correct the effects of longitudinal conduction in the indicated or measured heat transfer coefficient obtained by the thin-wall technique.

#### B. RECOMMENDATIONS

In order to insure accuracy in correcting the effects of longitudinal conduction:

1. A sufficient number of thermocouples should be used in order to obtain an accurate description of the longitudinal variation in temperature along the centerbody.
2. The thermocouples should be equally spaced (if possible).
3. Extreme care and accuracy be exercised in measuring the position of and distance between thermocouples.

NOMENCLATURE  
for Appendix A

b	wall thickness
c	specific heat of wall material
$h_n$	local convection heat transfer coefficient
$h'_n$	local indicated convection heat transfer coefficient (uncorrected for longitudinal conduction and curvature* characteristics of thin-wall
$h' = \frac{\rho c b}{(T_R - T_n)} \quad \frac{dT_n}{d\beta}$	
k	thermal conductivity of wall material
R	outside radius of spherical nose segment
$R_M$	mean radius of spherical nose segment (see Figure 1)
$R_M = (R - \frac{b}{2})$	
$r_n$	local outside radius of an increment along the conical section (see Figure 2)
$r_{M_n}$	local mean radius of an increment along the conical section (see Figure 2)
$r_{M_{n(n-1)}}$	local mean radius between increments with temperatures $T_n$ and $T_{n-1}$ (see Figure 2)
$T_i$	initial temperature
T	average wall temperature of an increment of the thin wall (either on spherical nose segment or along conical section.)
$T_R$	gas recovery temperature
$\Delta\chi_n$	length of an increment containing the temperature $T_n$

---

\* In equations (1) and (3),  $h'_n$  is multiplied by the factors  $(R_M/R)^2$  and  $(r_M/r_n)$ , respectively, to correct for the curvature characteristics of the thin-walled sections.

## APPENDIX B

### STAGNATION POINT HEAT TRANSFER FOR A SPHERICAL BODY

#### Heat Flux Relation

Starting from the simple expression

$$q = h (T_R - t_w) \quad (1)$$

and introducing Stanton Number

$$q = St (\rho \cdot u) \bar{c}_p (T_R - t_w) \quad (2)$$

or using enthalpy values

$$q = St (\rho \cdot u) (H_R - h_w) \quad (3)$$

Introducing Reynolds Number, relation (3) changes to

$$q = \frac{St \sqrt{Re}}{Re} (\rho U) (H_R - h_w) = (St \sqrt{Re}) \frac{\rho u}{\sqrt{\frac{\rho u x}{\mu}}} (H_R - h_w) \quad (4)$$

$$\text{Combining the ratio } \frac{\rho u}{\sqrt{\frac{\rho u x}{\mu}}} = (\rho \mu)^{0.5} = \left(\frac{u}{x}\right)^{0.5} = (\rho \mu)^{0.5} \beta^{0.5} \quad (5)$$

where  $\beta$  designates the velocity gradient at the outer edge of the boundary layer. Thus (4) becomes

$$q = f \cdot (\rho \mu)^{0.5} \cdot \beta^{0.5} \cdot \Delta H \quad (6)$$

By definition  $f$  is a dimensionless heat transfer parameter equal to

$$St \cdot \sqrt{Re}$$

From the interrelation of various dimensionless parameters

$$N = \frac{R_e P_r S_t}{t} \quad (7)$$

Thus  $f$  can also be expressed in the form of a Nusselt-Reynolds-Prandtl function

$$f = \frac{N_U}{P_r \sqrt{R_e}} \quad (8)$$

As for a given case the Prandtl Number stays practically constant, Stine and Wanlass in their Paper (NACA TN-3344) (Reference 12) developed a method to compute the ratio  $\frac{N_U}{\sqrt{R_e}}$  and thus  $f$  for any point at the surface of a body of revolution.

(See Figure 4b of the above Paper.)

At the stagnation point and the close neighborhood of it,  $f$  can be calculated from the relation

$$f = 0.763 P_r^{-0.6}$$

valid for spherical body shape and laminar flow conditions.

# APPENDIX C

## LAMINAR HEAT TRANSFER RATES TO CENTER BODY NOSE AS A FUNCTION OF DISTRIBUTION ANGLE $\theta$

The heat flux is computed from VAN DRIEST's equation:

$$q_w = f_L (\rho \mu)^{0.5} \left( \frac{\partial u}{\partial x} \right)^{0.5} \Delta H$$

The major assumptions and operating conditions (gaseous nitrogen supply) are summarized as follows:

TABLE C-1

REGIONS		AHEAD OF BOW SHOCK		AFTER BOW SHOCK	
		STAGNATION	FREE STREAM	STAGNATION	FREE STREAM
		(1) <sub>o</sub>	(1) <sub>∞</sub>	(2) <sub>o</sub>	(2) <sub>∞</sub>
PARAMETERS					
T	°R	1400	----	1400	----
t	°R	----	233	----	1353
P	psia	550	----	33.95	----
p	psia	----	1.04	----	30.16
M		----	5	----	0.415
$\rho$	lb/ft <sup>3</sup>	----	0.01165	0.0634	0.0584
$\mu \times 10^6$	lb/ft/sec	23.1	8.0	23.0	22.5
U	ft/sec	----	3810	----	763
$\rho \mu \times 10^6$		----	0.0932	1.456	1.313

Wall temperature:  $t_w = 800^\circ\text{R}$

Total enthalpy:  $H = 154.8 \text{ BTU/lb}$

## Pressure Distribution

Once the pressures at various points of the nose surface are known, isentropic expansion from the forward stagnation point is assumed. Thus from the pressures, corresponding temperatures are obtained from the isentropic tables permitting to calculate densities and viscosities.

Table C-2 below, which helps to establish the pressures, is compiled from the results of numerical solutions from a Paper by M. D. VAN DYKE (Reference 11). Values for  $M = 4$  and  $M = 6$  are taken from Table IV of Reference 11. These curves are shown in Figure C-1. Pressures for  $M = 5$  are obtained by interpolation and are listed in Table C-3.

TABLE C-2

CASE 178 ( $\gamma = 1.4$ $M = 6$ )						CASE 177 ( $\gamma = 1.4$ $M = 4$ )					
n	$X_1 - \Delta S$	$\frac{R_s}{R_b}(X_1 - \Delta S)$	$\cos \theta$	$\theta$	$\frac{(P_2)_x}{(P_\infty U_\infty^2)_1}$	$X_1 - S$	$\frac{R_s}{R_b}(X_1 - \Delta S)$	$\cos \theta$	$\theta$	$\frac{(P_2)_x}{(P_\infty U_\infty^2)_1}$	
0	0	0	1	0	0.928	0	0	1	0	0.940	
2	0.0012	0.00164	0.99836	3.283	0.925	0.0015	0.00217	0.99783	3.775	0.935	
4	0.0060	0.00820	0.99180	7.342	0.911	0.0084	0.01215	0.98785	8.94	0.915	
6	0.0148	0.02025	0.97975	11.550	0.886	0.0208	0.0302	0.9698	14.117	0.878	
8	0.0277	0.03785	0.96215	15.815	0.850	0.0389	0.0564	0.9436	19.332	0.828	
10	0.0446	0.06100	0.93900	20.115	0.804	0.0628	0.0911	0.9089	24.647	0.776	
12	0.0658	0.09000	0.91000	24.484	0.750	0.0927	0.1346	0.8654	30.072	0.689	
14	0.0914	0.12500	0.87500	28.955	0.687	0.1293	0.1872	0.8128	35.63	0.601	
16	0.1217	0.16650	0.83350	33.540	0.616	0.1730	0.2508	0.7492	41.479	0.494	
18	0.1570	0.21450	0.78550	38.233	0.530	0.1981	0.2873	0.7127	44.545	0.429	
19	0.1766	0.24150	0.75850	40.666	0.466						

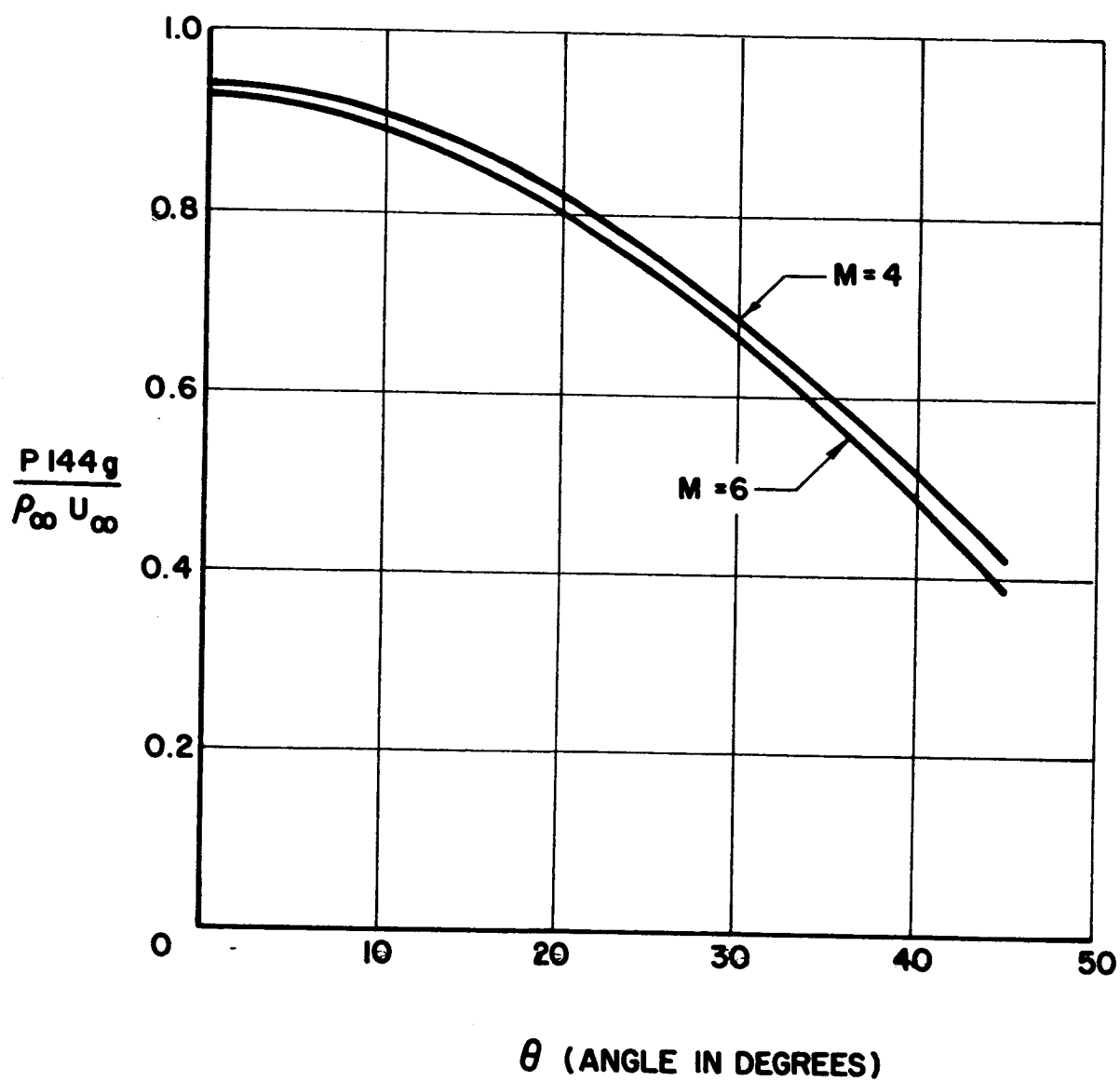


Figure C-1

Pressure Distribution over a Spherical Body in a Supersonic Gas Stream

In Table C-2 with  $R_S = 1$ , the values of  $\Delta S$  and  $R_b$  are taken from Table III of the Reference Paper.

$$\text{for Case 177 } \Delta S = 0.1201 \quad \frac{1}{R_b} = 1.368$$

$$\text{for Case 178 } \Delta S = 0.1084 \quad \frac{1}{R_b} = 1.45$$

and  $\cos \theta = 1 - \frac{R_S}{R_b} (\chi_i - \Delta S)$  where  $\chi_i$  is taken from Table IV of the Reference Paper.

Curves are drawn  $\left( \theta \text{ versus } \frac{(p_2)_x}{(\rho_\infty u_\infty^2)_1} \right)$  and the interpolated values of  $\frac{(p_2)_x}{(\rho_\infty u_\infty^2)_1}$ , as

listed in Table C-3 below for  $M = 5$ , are taken as mean values from Figure C-1.

Table C-3 lists free stream temperatures, densities and viscosities at the edge of the boundary layer and ten locations.

TABLE C-3

0	$\frac{(P_2)_x}{(\rho_\infty u_\infty^2)_1}$	$(p_2)_x$	$\frac{(P_2)_x}{(P_2)_0}$	$\frac{(\rho_2)_x}{(\rho_2)_0}$	$(\rho_2)_x$	$\frac{(t_2)_x}{(T_2)_0}$	$(t_2)_x$	$(\mu_2)_x \cdot 10^6$	$(\rho_2 \mu_2)_x \cdot 10^6$	$(\rho_2 \mu_2)_x^{0.5} \cdot 10^3$
0	0.934	33.95	1.0	1.0	0.0634	1.0	1400	23.0	1.456	1.207
5	0.926	33.67	0.992	0.9943	0.0630	0.9977	1397	22.98	1.445	1.202
10	0.902	32.78	0.966	0.9756	0.0617	0.9902	1386	22.90	1.413	1.185
15	0.864	31.50	0.928	0.948	0.0601	0.9789	1370	22.75	1.368	1.169
20	0.814	29.60	0.872	0.9068	0.0575	0.9616	1346	22.5	1.294	1.138
25	0.752	27.35	0.806	0.8572	0.0542	0.9403	1316	22.2	1.204	1.097
30	0.681	24.75	0.728	0.797	0.0505	0.9132	1278	21.8	1.104	1.051
35	0.601	21.85	0.643	0.730	0.0462	0.8810	1232	21.3	0.985	0.993
40	0.510	18.55	0.547	0.650	0.0412	0.8417	1179	20.7	0.852	0.923
	0.402	14.60	0.430	0.5475	0.0347	0.7860	1100	19.8	0.687	0.830

The pressure is referred to free stream conditions equal to

$$\frac{(\rho_{\infty} U^2)_1}{144 \cdot 32.2} = 36.4$$

Heat Flux:  $(q_w)_x = (f_L)_x \left(\frac{\partial U}{\partial x}\right)_x^{0.5} (\rho_2 \mu_2)_x^{0.5} \bar{c}_p (T_R - t_w)_x$

The laminar heat transfer parameters  $(f_L)_x$  are computed from TE-3344, Figure 4b, as the results of a study by STINE & WANLASS (Reference 12)

$$f_L = \frac{M_u}{P_r \cdot \sqrt{Re}}$$

The velocity gradient is also based on the above pressure distribution and isentropic expansion from the stagnation point. The tangential velocities at the edge of the boundary layer are referred to  $a^*$  and correspond to the pressure ratios. They may be obtained directly from isentropic tables ( $U/a^*$  - values) or, if delicate interpolation is to be avoided, they can be computed from equation:

$$\frac{U}{a^*} = 2.45 \sqrt{1 - \left(\frac{P_2}{P_{2x}}\right)^{0.286}} \quad \text{for } \gamma = 1.4$$

$$T^* = 0.8333 (T_2)_0 = 1166.7^\circ R$$

$$a^* = \sqrt{\gamma R T^* g} = 1700 \text{ ft/sec}$$

TABLE C-4

$\theta$	$\frac{U}{a^*}$	U ft/sec	$R_o \left( \frac{\partial U}{\partial x} \right)_x$	$\left( \frac{\partial U}{\partial x} \right)_x^{0.5}$ for $R_o =$			$(f_L)_x$	$(M_2)_x$	$(T_R)_x$	$\Delta H_x$
				$\frac{0.395}{12}$	$\frac{0.87}{12}$	$\frac{1.58}{12}$				
0	0	0	2465	274.1	184.45	137.05	0.956	0	1400	154.8
5	0.1175	201	2425	271.6	182.90	135.80	0.955	0.127	1400	154.8
10	0.2425	412	2380	268.9	181.25	134.45	0.953	0.264	1400	154.8
15	0.3565	608	2345	266.9	179.80	133.45	0.950	0.329	1395	153.5
20	0.4798	817	2330	266.2	179.15	133.10	0.945	0.447	1391	152.5
25	0.598	1020	2345	266.9	179.80	133.45	0.937	0.572	1387	151.5
30	0.721	1228	2395	269.9	182.00	134.95	0.925	0.689	1379	149.4
35	0.845	1436	2540	278.2	187.45	139.10	0.912	0.82	1369	146.8
40	0.975	1660	2740	288.8	194.70	144.40	0.895	0.97	1363	145.2
45	1.134	1935	3140	309.1	208.30	154.50	0.870	1.168	1349	141.4

Table C-4 gives U as a function of  $\theta$ . The U - values are also plotted versus  $\theta$  (see Figure C-2). The velocity gradient  $\partial U / \partial \theta = R_o$ .  $\partial U / \partial x$  is obtained from the slope to the curve at various angles. The Table also contains the term  $\left( \frac{\partial U}{\partial x} \right)_x^{0.5}$  for the three nose configurations. The recovery temperature is computed from the relation:

$$(T_R)_x = (t_2)_x \left[ 1 + \eta \left( \frac{\gamma-1}{2} \right) M_x^2 \right]$$

Assuming a constant Prandtl Number of 0.69, the recovery factor becomes 0.83 ( $\eta = P_r^{0.5}$  for laminar conditions).

Enthalpy values  $\Delta H_x$  are calculated for a fixed wall temperature of 800°R and a constant specific heat equal to 0.258 BTU/lb °R.

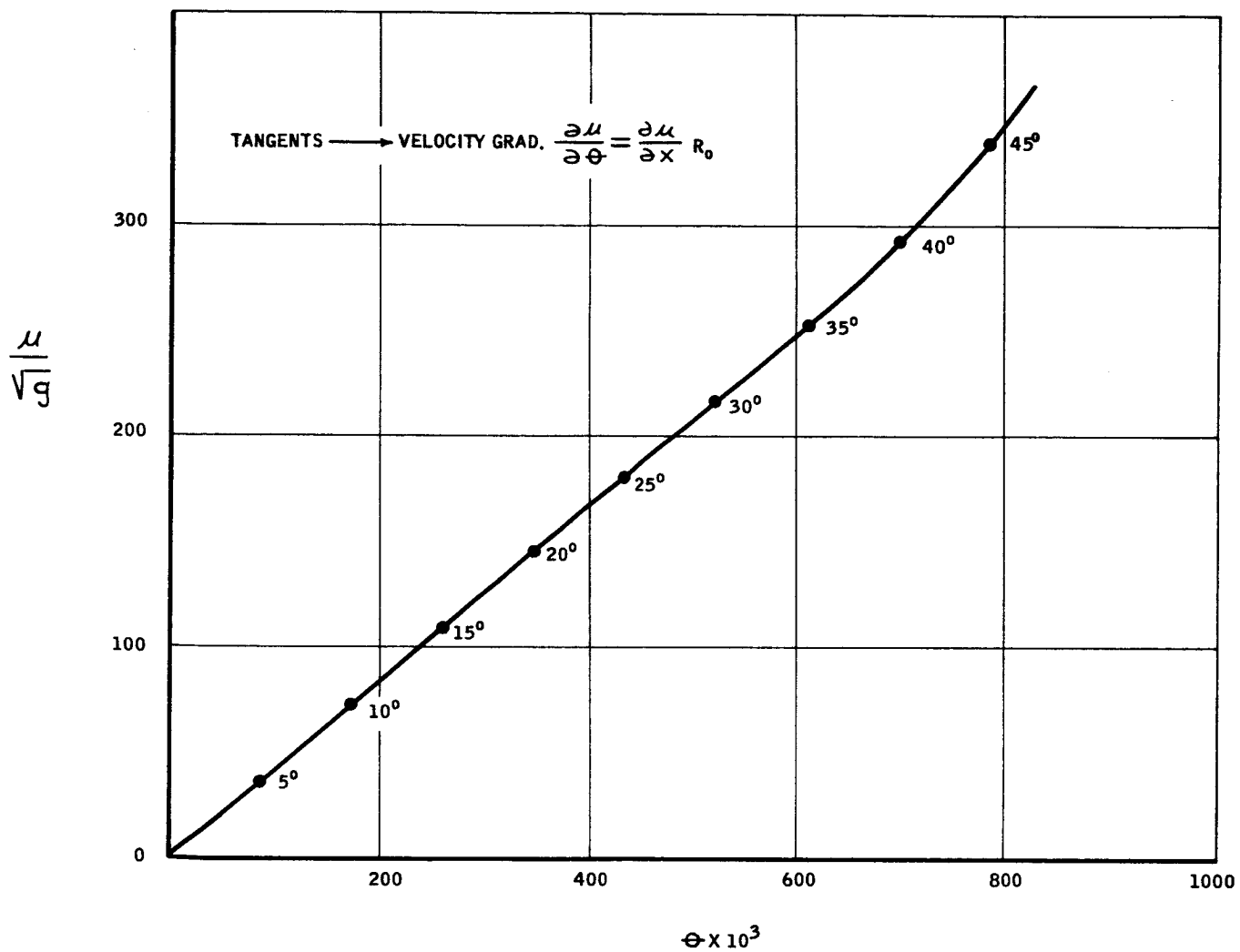


Figure C-2

Velocities versus Angle  $\theta$

Table C-5 below lists  $(q_w)_x$  and  $b_x$  - values.

TABLE C-5

$\theta$	$f_{L_x} (\rho \mu)_x^{0.5}$	$(q_w)_x$ in BTU/in. <sup>2</sup> , sec			$10^4 \cdot h_x$ in BTU/in. <sup>2</sup> , sec, °R		
	$\cdot \Delta H_x$ $R_o$	0.0329	0.0725	0.1315	0.0329	0.0725	0.1315
0	0.1780	0.3386	0.2290	0.1693	5.645	3.802	2.822
5	0.1772	0.3340	0.2247	0.1670	5.559	3.743	2.780
10	0.1745	0.3253	0.2194	0.1626	5.421	3.653	2.710
15	0.1705	0.3154	0.2125	0.1577	5.304	3.568	2.652
20	0.1640	0.3030	0.2040	0.1515	5.128	3.451	2.564
25	0.1560	0.2886	0.1944	0.1443	4.910	3.312	2.455
30	0.1450	0.2710	0.1827	0.1355	4.676	3.153	2.338
35	0.1327	0.2561	0.1725	0.1280	4.501	3.035	2.250
40	0.1197	0.2391	0.1610	0.1195	4.250	2.860	2.120
45	0.1020	0.2189	0.1475	0.1094	3.983	2.684	1.991

APPENDIX D  
TURBULENT HEAT TRANSFER RATES TO CENTERBODY NOSE AS A FUNCTION  
DISTRIBUTION ANGLE  $\theta$

The relation suggested by VAN DRIEST (Reference 9) to compute turbulent heat flux has the form

$$q_w = f_T \left( \frac{\rho U}{\rho_x} \right)^{0.8} \rho_2^{0.8} \mu_2^{0.2} x^{0.6} \bar{c}_p (T_R - t_w)$$

The major assumptions and operating conditions are summarized in Table D-1

<u>TABLE D-1</u>					
REGIONS		AHEAD OF BOW SHOCK		AFTER BOW SHOCK	
		STAGNATION (1) <sub>o</sub>	FREE STREAM (1) <sub>∞</sub>	STAGNATION (2) <sub>o</sub>	FREE STREAM (2) <sub>∞</sub>
PARAMETERS					
T	°R	1400	----	1400	----
t	°R	----	233	----	1353
P	psia	550	----	33.95	----
p	psia	----	1.04	----	30.16
M		----	5	----	0.415
ρ	lb/ft <sup>3</sup>	----	0.01165	0.0634	0.0584
μ . 10 <sup>6</sup>	lb/ft/sec	23.1	8.0	23.0	22.5
U	ft/sec	----	3810	----	763
(ρμ) . 10 <sup>6</sup>		----	0.0932	1.456	1.313

Wall temperature:  $t_w = 800^\circ$

Total enthalpy:  $\Delta H = 154.8 \text{ BTU/lb}$

The method to calculate the pressure distribution is the same as for laminar flow. The details are shown in Appendix C.

The heat transfer parameter is approximated from an empiric relation:

$$(f_T)_x = C(0.03 + 0.012 \cos^2 \theta)$$

$$\text{where } C = P_r^{-0.67}$$

Considering that for a flat plate  $f_T = 0.03C$ , and  $0.042C$  for the forward stagnation point of a sphere, then the above relation reflects approximately a linear decrease of  $f_T$  with pressure.

Table C-2 lists the body contour distances  $x$ , the terms  $x^{0.6}$ ,  $p_2^{0.8}$ ,  $\mu_2^{0.2}$  and  $f_T$  - values. The values of the transport properties  $\rho$  and  $\mu$ , which are the same as for the laminar conditions, are not repeated in this memorandum.

TABLE D-2

$\theta$ in degr.	$\theta$ in rad.	$X$ (in ft) for $R_o =$			$x^{0.6}$ for $R_o =$			$(\rho)_{2x}^{0.8}$	$(\mu)_{2x}^{0.2}$	$f_{T_x}$
		0.0329	0.0725	0.1315	0.0329	0.0725	0.1315			
0	0	0	0	0	0	0	0	0.110	0.1181	0.0538
5	0.08725	0.00287	0.00633	0.01149	0.0296	0.0478	0.0682	0.109	0.1181	0.0537
10	0.1745	0.00574	0.01266	0.02295	0.0452	0.0726	0.1035	0.1075	0.1180	0.0533
15	0.2617	0.00862	0.01897	0.03450	0.0575	0.0925	0.1350	0.1062	0.11786	0.0528
20	0.3490	0.01149	0.02532	0.04596	0.0682	0.1105	0.1575	0.1023	0.1176	0.0520
25	0.4360	0.01435	0.03160	0.05740	0.0780	0.1260	0.1800	0.0972	0.1173	0.0509
30	0.5235	0.01723	0.03796	0.06894	0.0872	0.1400	0.1988	0.0920	0.1169	0.0500
35	0.6110	0.02013	0.04425	0.08050	0.0960	0.1540	0.2200	0.0855	0.1164	0.0488
40	0.6980	0.02298	0.25064	0.09192	0.1040	0.1670	0.2380	0.0780	0.1157	0.0475
45	0.7850	0.02580	0.25696	0.10341	0.1115	0.1790	0.2560	0.0680	0.1146	0.0462

The recovery temperature is computed from the relation:

$$(T_R)_x = (t_2)_x = \left[ 1 + \eta_T \left( \frac{\gamma-1}{2} \right) M_x^2 \right]$$

For an assumed constant Prandtl Number of 0.69, the recovery factor becomes 0.88  
 $(\eta_T = P_r^{0.33}$  for turbulent conditions).

Enthalpy - values are calculated for a fixed wall temperature of 800°R and a constant specific heat of 0.258 BTU/lb °R.

Table D-3 below lists  $(q_w)_x$  and  $h_x$  - values. These values are also shown in graphical form (Tables D-2 and D-3) as a function of angle  $\theta$ . The maximum of the curves is around 41° which should correspond to the sonic point.

TABLE D-3

$\theta$	$(T_R)_x$	$\Delta H_x$	$(f_r)_n \cdot \frac{\Delta H_x}{(p_2)_x^{0.8} (h_2)_x R_o}$	$\frac{\partial U}{\partial x} \cdot 0.8$			$(q_w)_x$ in BTU/in. <sup>2</sup> , sec			$10^4 \cdot h_x$ in BTU/in. <sup>2</sup> , sec. °R		
				0.0329	0.0725	0.1315	0.0329	0.0725	0.1315	0.0329	0.0725	0.1315
0	1400	154.8	0.1082	7910	4205	2610	0	0	0	---	---	---
5	1400	154.8	0.1070	7820	4160	2577	0.172	0.147	0.130	2.865	2.45	2.17
10	1400	154.8	0.1047	7676	4080	2527	0.251	0.214	0.190	4.18	3.57	3.17
15	1396	154.0	0.1016	7600	4035	2502	0.308	0.263	0.2335	5.17	4.41	3.92
20	1394	153.5	0.0960	7545	4015	2490	0.3425	0.292	0.259	5.77	4.92	4.365
25	1392	153.0	0.0887	7600	4035	2502	0.3645	0.3115	0.276	6.16	5.26	4.66
30	1385	151.0	0.0812	7740	4120	2555	0.380	0.3245	0.2875	6.49	5.55	4.91
35	1377	148.8	0.0722	8075	4290	2665	0.389	0.332	0.294	6.74	5.74	5.09
40	1374	148.2	0.0636	8605	4575	2834	0.395	0.337	0.299	6.88	5.88	5.21
45	1365	145.8	0.0524	9590	5100	3163	0.3895	0.3325	0.295	6.88	5.88	5.21

## APPENDIX E

### Laminar Heat Transfer Rates to Cone Frustum

Heat transfer rates are computed from Lester Lees' equation

$$(q_w)_s = (q_w)_o \frac{A_\alpha \cdot s'/R_o}{\left[ B_\alpha + (s'/R_o)^3 \right]^{\frac{1}{2}}}$$

Parameters  $A_\alpha$  and  $B_\alpha$  are a function of  $\alpha$ ,  $\gamma$  and  $M$ .

$$A_\alpha = \frac{\sqrt{3}}{2} \left[ 1 - \frac{1}{\gamma_\infty M_\infty^2} \sin^2 \alpha + \frac{1}{\gamma_\infty M_\infty^2} \right]^{\frac{1}{2}} \sqrt{\frac{\pi}{2} - \alpha}$$

$$B_\alpha = \frac{3/16}{\sin^2 \alpha \left[ 1 - \frac{1}{\gamma_\infty M_\infty^2} \sin^2 \alpha + \frac{1}{\gamma_\infty M_\infty^2} \right]} \cdot \frac{D_\beta}{\beta} - \cot^3 \alpha$$

where

$$D_\beta = \left( 1 - \frac{1}{\gamma_\infty M_\infty^2} \right) \left( \beta^2 - \frac{\beta \sin 4\beta}{2} + \frac{1 - \cos 4\beta}{8} + \frac{4}{\gamma_\infty M_\infty^2} \right. \\ \left. \left( \beta^2 - \beta \sin 2\beta + \frac{1 - \cos \beta}{2} \right) \right)$$

$$\text{where } \beta = \pi/2 - \alpha$$

with  $\gamma = 1.4$  and  $M = 5$  these forms reduce to:

$$A_\alpha = 0.866 \sqrt{\frac{\pi}{2} - \alpha} (0.9714 \sin^2 \alpha + 0.0286)^{0.5}$$

$$B_\alpha = \frac{0.1875}{\sin^2 \alpha (0.9714 \sin^2 \alpha + 0.0286)} \cdot \frac{D_\beta}{\beta} - \cot^3 \alpha$$

$$D_\beta = 0.9714 \left( \frac{\pi}{2} - \alpha \right)^2 - 0.5 \left( \frac{\pi}{2} - \alpha \right) \sin 4 \left( \frac{\pi}{2} - \alpha \right) + 0.125 \left\{ 1 - \cos \left( \frac{\pi}{2} - \alpha \right) \right\} \\ + 0.1144 \left( \frac{\pi}{2} - \alpha \right)^2 - \left( \frac{\pi}{2} - \alpha \right) \sin 2 \left( \frac{\pi}{2} - \alpha \right) + 0.5 \left\{ 1 - \cos 2 \left( \frac{\pi}{2} - \alpha \right) \right\} \\ = 0.9714X + 0.1144Y$$

Tables E-1 and E-2 give the details of the calculations of A, B and D.

TABLE E-1

$\alpha$ Degrees	$\alpha$ Radians	$\left(\frac{\pi}{2} - \alpha\right)$		$2\left(\frac{\pi}{2} - \alpha\right)$		$4\left(\frac{\pi}{2} - \alpha\right)$		$\cos\left(\frac{\pi}{2} - \alpha\right)$	$\cos 2\left(\frac{\pi}{2} - \alpha\right)$	$\sin 2\left(\frac{\pi}{2} - \alpha\right)$	$\sin 4\left(\frac{\pi}{2} - \alpha\right)$
		Deg	Radians	Deg	Radians	Deg	Radians				
16	0.2792	74	1.2915	148	2.5831	296	5.1662	0.2756	-0.848	0.5299	-0.8988
23	0.4014	67	1.1694	134	2.3388	268	4.6776	0.3907	-0.6946	0.7193	-0.9994
30	0.5236	60	1.0472	120	2.0944	240	4.1888	0.5	-0.5	0.866	-0.866

TABLE E-2

$\alpha$ Degrees	$\sqrt{\frac{\pi}{2} - \alpha}$	$\left(\frac{\pi}{2} - \alpha\right)^2$		$\sin^2 \alpha$	$\cot^3 \alpha$	$\frac{X}{Y}$	$\frac{D_a}{A_a}$	$\frac{B_a}{A_a}$
		Deg	Radians					
16	1.137		1.67	0.076	42.09	2.3415	2.488	22.3
23	1.082		1.368	0.1527	13.15	2.0293	2.127	1.92
30	1.023		1.095	0.25	5.196	1.6105	1.67	-0.266

The distance  $s'$  is calculated from:

$$s' = \frac{R_o}{\sin(\alpha + \theta)} \cdot \frac{\sin \theta}{\sin \alpha} = R_o [\cot \alpha + \cot(\alpha + \theta)]$$

In order to represent the  $(q_w)_s$  - values graphically, the distance  $s$  had to be computed:

$$s = X + \Delta s' = X + R_o \cot(\alpha + \theta)$$

Tables E-3 and E-4 give the values of  $s$  and  $s'$  corresponding to angles  $\alpha$  and  $\theta$ .

Table E-4 also contains dimensionless  $(q_w)_s$  - values. Table E-5 lists  $q$  and  $h$  for all three nose configurations.

TABLE E-3

$\alpha$ Degr.	$\theta$ Degr.	$\theta$ Radians	X in inches			$\Delta s'$ in inches			s in inches		
			$R_o=0.395$	$\frac{0.87}{-}$	$\frac{1.58}{-}$	$\frac{0.395}{-}$	$\frac{0.87}{-}$	$\frac{1.58}{-}$	$\frac{0.395}{-}$	$\frac{0.87}{-}$	$\frac{1.58}{-}$
16, 23, 30	5	0.08725	0.03446	0.0759	0.13785	-	-	-	0.03446	0.0759	0.13785
16, 23, 30	45	0.785	0.3100	0.683	1.2402	-	-	-	0.3100	0.683	1.2402
16	74	1.29154	0.51	1.124	2.04	-	-	-	0.5100	1.124	2.04
23	67	1.16937	0.462	1.016	1.848	-	-	-	0.462	1.016	1.848
30	60	1.0472	0.4135	0.912	1.654	-	-	-	0.4135	0.912	1.654
16	90	-	-	-	-	0.113	0.249	0.452	0.623	1.373	2.412
23	90	-	-	-	-	0.1675	0.369	0.670	0.6295	1.385	2.518
30	90	-	-	-	-	0.228	0.5012	0.912	0.6415	1.4132	2.566
16	105	-	-	-	-	0.237	0.522	0.948	0.747	1.646	2.988
23	105	-	-	-	-	0.3035	0.679	1.234	0.7705	1.695	3.082
30	105	-	-	-	-	0.355	0.87	1.58	0.8085	1.782	3.234
16	120	-	-	-	-	0.409	0.902	1.636	0.919	2.026	3.676
23	120	-	-	-	-	0.523	1.153	2.092	0.985	2.169	3.94
30	120	-	-	-	-	0.684	1.507	2.736	1.0875	2.419	4.39
16	135	-	-	-	-	0.712	1.568	2.848	1.222	2.692	4.888
23	135	-	-	-	-	0.977	2.15	3.908	1.439	3.166	5.756
30	135	-	-	-	-	1.475	3.25	5.90	1.8885	4.162	7.554

TABLE E-4

$\alpha$ Degr.	$\epsilon$ Degr.	$(\alpha + \epsilon)$ Degr.	$\sin \alpha$	$\sin \alpha$	$\sin(\alpha + \epsilon)$	$s'/R_o$	$(s'/R_o)^3$ = Z	$A \frac{s'}{\alpha R_o}$	$(B_\alpha + Z)^{\frac{1}{2}}$	$\frac{(q_w)s}{(q_w)_o} 100 \text{ in } \phi$
16	74	90	0.2756	0.9613	1.0	3.4874	42.5	1.10	8.06	13.66
16	90	106	0.2756	1.0	0.9613	3.774	53.7	1.19	8.72	13.63
16	105	121	0.2756	0.9659	0.8572	4.088	68.5	1.29	9.53	13.55
16	120	136	0.2756	0.866	0.6947	4.523	92.3	1.425	10.70	13.30
16	135	151	0.2756	0.7071	0.4848	5.291	148.4	1.666	13.06	12.75
23	67	90	0.3907	0.9205	1.0	2.356	13.05	0.928	3.872	23.95
23	90	113	0.3907	1.0	0.9205	2.78	21.55	1.093	4.845	22.55
23	105	128	0.3907	0.9659	0.788	3.137	30.75	1.232	5.72	21.55
23	120	143	0.3907	0.866	0.6018	3.683	50.0	1.45	7.20	20.15
23	135	158	0.3907	0.7071	0.3746	4.831	113.0	1.90	10.72	17.72
30	60	90	0.5	0.866	1.0	1.732	5.2	0.798	2.225	35.80
30	90	120	0.5	1.0	0.866	2.309	12.3	1.064	3.465	30.70
30	105	135	0.5	0.9659	0.7071	2.732	20.4	1.26	4.49	28.10
30	120	150	0.5	0.866	0.5	3.464	41.5	1.595	6.42	24.85
30	135	165	0.5	0.7071	0.2588	5.464	163.0	2.515	12.74	19.72

TABLE E-5

$s'/R_o$	$\theta$ Degr.	$\alpha$ Degr.	$(q_w)_s$ BTU/in. <sup>2</sup> , Sec			$10^4 \cdot h_s^*$ BTU/in. <sup>2</sup> , sec, °R		
			0.395"	0.87"	1.58"	0.395"	0.87"	1.58" $R_o/R_o$
3.4874	74	16	0.0463	0.03135	0.02315	0.842	0.572	0.421
3.774	90		0.0462	0.0313	0.0231	0.840	0.570	0.420
4.088	105		0.0459	0.0311	0.02295	0.835	0.565	0.418
4.523	120		0.0451	0.0305	0.02255	0.820	0.552	0.410
5.291	135	16	0.0433	0.0293	0.02162	0.787	0.533	0.394
2.356	67	23	0.0812	0.0549	0.0406	1.476	0.999	0.738
2.780	90		0.0766	0.0518	0.0383	1.394	0.942	0.697
3.137	105		0.0730	0.0495	0.0365	1.292	0.900	0.646
3.683	120		0.0684	0.0462	0.0342	1.244	0.840	0.622
4.831	135	23	0.0602	0.0406	0.0301	1.094	0.739	0.547
1.732	60	30	0.1216	0.0824	0.0608	2.212	1.500	1.106
2.309	90		0.1040	0.0705	0.0520	1.892	1.282	0.946
2.732	105		0.0952	0.0644	0.0476	1.732	1.172	0.866
3.464	120		0.0842	0.0571	0.0421	1.532	1.040	0.766
5.464	135	30	0.0668	0.0453	0.0334	1.216	0.824	0.608

\*  $h$  is based on a fired temperature difference:  
 $\Delta T = 1350 - 800 = 550^\circ$  (1350 is  $T_R$  at  $45^\circ$ )

## APPENDIX F

### Heat Transfer to the Struts

The method of LESTER LEES allows heat flux computation to a planar front by replacing the constant of 0.707 by 0.47 in equation (2) of Section V-C-b. The free stream pressure ahead of the bow shock at the struts was determined from flow continuity and the assumed Mach number.

$$\text{also } t_w = 1500^\circ\text{R} \quad \mu_w = 12.1 \times 10^{-6} \text{ lb/ft sec.}$$

Ahead of the bow shock on the struts, assume three possibilities of  $M_{1\infty} = 2, 1.5$  and  $1.0$ .

Thus the heat flux becomes:

$$(q_w)_o = \left( G \times H_{se} \times U_\infty^{\frac{1}{2}} \times (\rho_e \mu_e)^{\frac{1}{2}} \right) \frac{0.47}{P_r^{2/3} R_o^{\frac{1}{2}}} \quad (1)$$

The following Table gives the computed values for pressures, temperatures, enthalpies and transport properties for three different Mach Numbers.

TABLE F-1

$M_{1\infty}$	$t_{1\infty}$	$U_\infty$	$U_\infty^{\frac{1}{2}}$	$G$	$H_{se}$	$P_2$	$P_w$	$10^6 \times \rho_w \mu_w$	$10^3 \times (\rho_w \mu_w)^{\frac{1}{2}}$	$(q_w)_o \times R_o^{\frac{1}{2}}$
2.0	2775	19600	140	0.852	7680	62.0	0.00775	0.0948	0.308	172
1.5	3450	16400	128	0.89	5370	55.7	0.00694	0.084	0.29	108
1.0	4165	12000	109.6	0.835	2880	51.0	0.00638	0.0772	0.0278	44.7

$$U_\infty = M_\infty \sqrt{\gamma_\infty g R t_\infty} \quad (2)$$

$$H_{se} = \frac{U_\infty^2}{2gJ} \quad (3)$$

$$G = \left[ \frac{(\gamma_\infty - 1)}{\gamma_\infty} \right]^{\frac{1}{4}} \left[ \left( 1 + \frac{2}{(\gamma_\infty - 1) M_\infty^2} \right) \left( 1 - \frac{1}{\gamma_\infty M_\infty^2} \right) \right]^{\frac{1}{4}} \quad (4)$$

Flow Areas are:  $A_D = 0.515 \text{ ft}^2$  and  $A_{AN} = 0.322 \text{ ft}^2$

Free stream pressure ahead the bow shock at the struts is computed from

$$\dot{w} = (\rho_\infty U_\infty)_{CB} A_D = A_{AN} \left( \frac{P_{1\infty} M_{1\infty}}{\sqrt{t_{1\infty}}} \right)_{\text{Str.}} \sqrt{\frac{\gamma g}{R}} \quad (5)$$

or

$$P_{1\infty} = \frac{(\rho_\infty U_\infty)_{CB} \times A_D \times \sqrt{t_{1\infty}}}{A_{AN} \sqrt{\frac{\gamma g}{R}} M_{1\infty}} = \frac{0.00034 \times 26850 \times 0.515 \sqrt{t_{1\infty}}}{144 \times 0.322 \sqrt{\frac{1.4 \times 32.2}{767}} M_{1\infty}}$$

$$P_{1\infty} = 0.417 \frac{\sqrt{t_{1\infty}}}{M_{1\infty}} \quad (6)$$

for $M_{1\infty} = 2$	$p_{1\infty} = 11.0 \text{ psia}$
$M_{1\infty} = 1.5$	$p_{1\infty} = 16.3 \text{ psia}$
$M_{1\infty} = 1.0$	$p_{1\infty} = 26.95 \text{ psia}$

The total pressure  $P_2$  (listed in the preceding Table) is taken from the tables from conditions across a normal shock.

The ratio of film coefficients Center Body to Struts is:

$$\frac{h_{\text{str.}}}{h_{\text{CB}}} = \frac{\left( \frac{(q_w)_o}{R_o^{\frac{1}{2}}} \cdot \frac{1}{T_R - t_w} \right)_{\text{str.}}}{\left( \frac{(q_w)_o}{R_o^{\frac{1}{2}}} \cdot \frac{1}{T_R - t_w} \right)_{\text{CB}}} = \frac{4970 - 1500}{425} \cdot \frac{(q_w)_o}{(T_R - 1500)_{\text{str.}}} \cdot \left( \frac{R_{\text{oCB}}}{R_{\text{ostr.}}} \right)^{\frac{1}{2}}$$

$$\frac{h_{\text{str.}}}{h_{\text{CB}}} = \frac{8.17 (q_w)_o}{(T_R - 1500)_{\text{str}}} \cdot \left( \frac{R_{\text{oCB}}}{R_{\text{ostr}}} \right)^{\frac{1}{2}} \quad (7)$$

The recovery temperature for conditions behind the bow shock is computed from

$$T_R = t_{2\infty} \left( 1 + \eta_L \frac{\gamma_\infty - 1}{2} M_{2\infty}^2 \right) \quad (8)$$

The following Table gives film coefficient, heat flux ratios for three different Mach Numbers and three ratios of center body nose to strut bluntness.

TABLE F-2

$M_{1\infty}$	$M_{2\infty}$	$t_{2\infty}$	$T_R$	$\frac{R_{oCB}}{R_{ostr.}}$	$\left(\frac{R_{oCB}}{R_{ostr.}}\right)^{\frac{1}{2}}$	$\frac{h_{str.}}{h_{CB}}$	$\frac{q_{wstr.}}{q_{wCB}}$
2.0	0.577	4680	4935	1	1	0.41	0.405
				2	1.412	0.58	0.572
				4	2	0.82	0.81
1.5	0.701	4560	4930	1	1	0.257	0.256
				2	1.412	0.363	0.36
				4	2	0.514	0.512
1.0	1.0	4165	4850	1	1	0.109	0.105
				2	1.412	0.154	0.149
				4	2	0.218	0.21

The heat flux ratio in the Table is based upon the stagnation point heat transfer at the center body nose for laminar boundary conditions. This value was previously calculated and found to be

$$(q_w)_{oCB} = \frac{423}{\sqrt{R_{oCB}}} \text{ BTU/sec ft}^2$$

for the nose radius in ft.